NTNU
Norwegian University of
Science and Technology

Hydrothermal syntheis and characterization of $BaTiO_3$ nanoparticles

Frida Sveen Hempel

Nanotechnology
Submission date: June 2018
Supervisor: Sverre Magnus Selbach, IMA

Norwegian University of Science and Technology
Department of Materials Science and Engineering

Preface

This thesis was carried out at the Department of Materials Science and Engineering at the Norwegian University of Science and Technology, spring 2018. My main supervisor has been Assoc. Professor Sverre Magnus Selbach and my co-supervisors have been Professor Mari-Ann Einarsrud and Ph.D. candidate Ola Gjønnes Grendal.

Acknowledgements

The project work has been challenging and could not have been done without the help of several people.

First of all I would like to give a special thank my main supervisor Sverre Magnus Selbach for endless support and guidance, and for always having time to discuss different challenges that occurred. Also, thank you for keeping my spirits up when the dipole ordering turned out to be more challenging than anticipated and the instruments kept breaking down. I am very grateful for everything I have learned from you.

My co-supervisor Ola Gjønnes Grendal for invaluable help with the hydrothermal synthesis and XRD. Kristine Bakken deserves a huge thanks for support with Raman spectroscopy and general advice and guidance.

The ceramics group at IMA deserves thanks, for helpful discussions and for making me feel so included. Especially Dr. Anders Bank Blichfeld, Dr. Dong Hou, Solveig Aamlid and Ola Gjønnes Grendal for doing the total scattering X-ray diffraction measurements on my samples. An additional thanks to Dr. Dong Hou for doing the conversion to PDF data.

I would also like to thank the technical staff at the department. Especially Kristin Wells and Julian Richard Tolchard for guidance and support with XRD and sample preparation, and Mikko Saraste for help and technical support, and for always answering my questions.

I would lastly like to thank Kristine Bakken and Tora Olsen for proof reading the whole thesis and an extended thanks to all my friends and family for love and support.

Abstract

This thesis investigates the size dependent dipole disorder in ferroelectric materials, which leads to a loss of macroscopic ferroelectricity, and the role of the depolarization field on this disorder. Structural characterization was done on particles dispersed in mediums with different dielectric constant, providing different electrostatic boundary conditions on the particles.

$BaTiO_3$ particles was prepared using hydrothermal synthesis, with varying process parameters to achieve particles with crystallites between 11 and 31 nm. An additional annealing step gave particles with crystallites between 40 and 94 nm.

For particle characterization, the different dispersion mediums was either oil or water, with dry particles as a reference. The average structure was characterized using Raman spectroscopy, X-ray diffraction and subsequent Pawley refinement. The local structure was measured using synchotron total scattering X-ray diffraction and pair distribution function analysis.

The three structural characterization methods reveal a complicated dipole ordering, as the influence from the dispersion medium is different over the different measurement length scales. The particle structures can not be explained on both local and average scale by symmetry models of either tetragonal $P4mm$ or $Pm\bar{3}m$ space group symmetry, suggesting a more complicated dipole ordering like domain structures or vortex states. The Raman spectroscopy data suggest an abrupt change in the dipole ordering between the particles with 20 and 24 nm crystallites, which could be interpreted as a transition in the dipole ordering from a coexisting polarization and vortex state to a polar domain structure. Further investigation is necessary before any final conclusions can be reached.

Sammendrag

Denne oppgaven undersøker størrelsesavhenging dipolordning i ferroelektiske materialer, som gir gradvis tap av makroskopisk ferroelektisitet, og rollen til depolarisasjonsfeltet på denne dipoluordenen. Strukturell karakterisering ble gjort på partikler dispergert i medier med ulik dielektrisk konstant, som gir ulike elektrostatiske grensebetingelser for partiklene.

$BaTiO_3$ partikler ble laget ved hydrotermal syntese, med ulike parametere for å gi partikler med krystallittstørrelser mellom 11 og 31 nm. Et ekstra glødesteg ble lagt til for å få partikler med krystallittstørrelser mellom 40 og 94 nm.

Partikkelkarakterisering ble gjort i enten olje eller vann, med tørre partikler som referanse. Gjennomsnittlig struktur ble karakterisert ved Raman spektroskopi, røntgendiffraksjon og følgende Pawley raffinering. Lokal struktur ble målt ved totalspredning-røntgendiffraksjon med synkotronstråling og pardistribusjonsfunksjon (PDF).

De tre strukturelle karakteriseringsmetodene avslører en komplisert dipolordning, der dispersjonsmediene er ulike over ulike lengdeskalaer. Partikkelstrukturen kan ikke forklares både lokalt og på gjennomsnittlig skala ved strukturmodellene med enten tetragonal $P4mm$ eller kubisk $Pm\bar{3}m$ romgruppesymmetri, noe som tyder på en mer komplisert dipolordning som for eksempel vortex states eller polare domener. Resultatet fra Raman spektroskopi tyder på en brå forandring i dipolordning mellom partiklene med 20 og 24 nm krystallitter, som tolkes som en overgang i dipolordningen mellom en polarisasjon og vortex state og en med polare domener. Videre undersøkelser er nødvendig før endelige konklusjoner kan treffes.

Contents

1 Introduction **9**
1.1 Background . . . 9
1.2 Research objective . . . 10

2 Literature survey **11**
2.1 Ferroelectricity . . . 11
2.1.1 Macroscopic ferroelectricity . . . 11
2.1.2 The crystallographic requirements of ferroelectricity . . . 11
2.1.3 The perovskite structure . . . 12
2.2 Barium titanate . . . 14
2.3 Size effects in ferroelectrics . . . 15
2.3.1 Ferroelectrictric structure at the nanoscale . . . 15
2.3.2 The driving force of ferroelectric disorder . . . 18
2.3.3 Depolarization field . . . 19
2.3.4 Dipole ordering in ferroelectric components . . . 20
2.4 Characterization techniques . . . 22
2.4.1 Total scattering and pair distribution function analysis . . . 22
2.4.2 Raman spectroscopy . . . 26

3 Experimental **31**
3.1 Hydrothermal synthesis . . . 31
3.2 Dispersion mediums . . . 34
3.3 Characterization . . . 34
3.3.1 X-ray Diffraction . . . 34
3.3.2 Background fitting . . . 36
3.3.3 Synchrotron X-ray Diffraction . . . 36
3.3.4 Raman spectroscopy . . . 37
3.3.5 Scanning electron microscope particle characterization . . . 38

4 Results **39**
4.1 Particle characterization . . . 39
4.2 Pawley fit on dispersed particles . . . 40
4.2.1 Background fits . . . 40
4.2.2 Pawley fit of particles dispersed in oil and water . . . 40

4.2.3 Pawley refinement of particles dispersed in eutectic gallium indium 41
4.3 Structure characterization from Raman spectroscopy 47
4.3.1 Size dependence 47
4.3.2 Influence of liquid layer thickness on Raman spectroscopy 47
4.3.3 The influence of dispersion medium 47
4.4 Local structure 51
4.4.1 Size dependence of the local structure 51
4.4.2 Influence from dispersion medium on the local structure 51
4.4.3 PDFs fitted to crystallographic models 54
4.4.4 Local structure analysis 58

5 Discussion **61**
5.1 Agreement between observed structure and crystal symmetry model . . . 61
5.1.1 Dipole order coherence length 61
5.1.2 Influence from the dispersion medium on ionic lattice expansion . 62
5.1.3 Limitations of the crystal structure model 66
5.1.4 Surface structure and the penetration depth of Raman spectroscopy 66
5.1.5 Surface adsorbed species 67
5.1.6 Difference in crystallite and particle size 67
5.2 Size dependent changes in the dipole ordering 67
5.3 Vortex states 70
5.4 Polar domains 71
5.5 Further work 77

6 Conclusion **79**

Appendices **87**

A Pawley fits for particles in all dispersion mediums **89**

B Rietveld refinement for size determination **107**

C Agreement factor R_{wp} for ADP **111**

D Scanning electron microscopy **113**

Chapter 1

Introduction

Ferroelectricity is observed to disappear at the nanoscale. A ferroelectric material is an ionic material, where the cations and anions create a spontaneous charge distribution, giving rise to dipoles. If the direction and axis is ordered, this gives the material a spontaneous macroscopic polarization. This master thesis investigates the disorder that follows a size reduction and the possible influence of the electrostatic boundary conditions as a means of stabilizing dipole order at the nanoscale. This will hopefully contribute to a better understanding of the size dependent dipole disorder, which is the limiting factor for possible use in technological applications.

1.1 Background

Ferroelectric materials are an integral part of modern electronics, which is currently defined by an ongoing miniaturization of electronic components. In 1965, Gordon Moore described the famous "Moore's law", which states that the performance of computers will double every year.[1] The performance is linked to data storage, where data is stored in bits, a physical representation of either 0 or 1 in the binary system. At the moment, this is done by charge storage, where a current is used to represent 1, and the absence of a current is 0. There is a size limit for this type of component, as tunneling is an increasing problem for nanoscale components, which is why ferroelectric materials are a promising candidate. By representing the bit by a polarization instead of a current, using a ferroelectric domain could possibly give a smaller unit than an electronic component, resulting in a much higher storing capacity. Another advantage is that the ferroelectric random access memory (FeRAM) will be non-volatile, meaning that a power failure will not lead to loss of stored data. Understanding the loss of ferroelectricity at reduced size is therefore fundamental for possible technological applications.[2,3,4]

The study of size effects in ferroelectrics was started by Batra and Wurfel in 1973, with the publications of two papers: The first investigating a ferroelectric thin film between a metal and a semiconductor and the other a ferroelectric thin film between two semiconductors.[5,6] They demonstrated that an incomplete compensation of the polarization at the interfaces will give a depolarization field that reduce the overall polarization in the

ferroelectric material.

From then on, there has been an ongoing search to find the size limit for the disappearance of ferroelectricity. Thin films are the most studied systems, because they are more used in technical applications. The size limitation in only one dimension also simplifies production of a component with well defined geometry, and the control and description of electrostatic boundary conditions. Several articles claim to find an absolute limit for ferroelectricity, with mentions of limits down to a few unit cells.[7,8,9] Fong *et.al.* has for example shown that when the depolarization field is neutralized, ferroelectric order in a $PbTiO_3$ thin film is present in a 3 unit cell thin film.[10] This paper motivates a more thorough investigation of the influence of the depolarization field and therefore the electrostatic boundary conditions on ferroelectricity.

The disappearance of ferroelectricity in nanoparticles have not been shown the same amount of interest as thin films, as technical applications are less apparent and there are large problems when defining their geometry. As for the thin film studies, many papers have been interested in determining the final size limit, and the reported values have varied over orders of magnitude of difference.[9,11,12] Lately, there has been a breakthrough with the work of Smith *et. al.* and Page *et. al.*, who characterized the local structure of ferroelectric $BaTiO_3$ particles with total scattering X-ray diffraction. They revealed that, contrary to earlier beliefs, the local dipole magnitude was increased, and the loss of ferroelectricity could not be due to a displacive phase transition, and instead suggest an order-disorder transition. Senn *et. al.* did an investigation of the temperature dependent phase transitions for $BaTiO_3$, showing that it is well described as an order-disorder phase transition.[13] Understanding the temperature dependent phase transitions, gives a better foundation for investigating and understanding of the size dependent phase transitions.

1.2 Research objective

The primary objective of this project is to investigate the role of the depolarization field on the dipole disorder and how the ferroelectricity in $BaTiO_3$ nanoparticles can be influenced by the electrostatic boundary conditions. The dipole disorder will be assessed by crystal structure characterization, both for average and local structure. The hypothesis is that the long range dipole order can be stabilized by providing shielding for surface dipoles, which will reduce dipole disorder and give a larger macroscopic polarization in the nanoparticle. If the electrostatic shielding increase microscopic polarization, this is a possible method for conserving ferroelectricity at smaller particle sizes.

The $BaTiO_3$ nanoparticles will be prepared by hydrothermal synthesis, which was investigated in the project work written and submitted during the fall 2017 at NTNU. The result of this project work was that the recipe used in this synthesis steadily produced particles between 11 and 31 nm, and larger sizes needed an additional annealing step.

Chapter 2

Literature survey

2.1 Ferroelectricity

2.1.1 Macroscopic ferroelectricity

A ferroelectric material is an insulating material with a switchable polarization, that will be remnant in the material in the absence of an electric field.[14,15] Under both very low and high electric fields, the ferroelectric material behaves like a dielectric, usually with a very high dielectric constant. However, the direction of the polarization can be reversed with a specific magnitude of the electric field, called the coercive field. This is the reason for the the non-linear relationship between the electric field and the polarization, which is an important feature of the ferroelectric material. The relationship follows a hysteresis curve, shown in figure 2.1. The hysteresis curve shows the coercive field, where there is no polarization, the remnant polarization, under no electric field, and the saturated polarization, which is the limiting value of polarization. This is only true for a single crystal ferroelectric. The presence of grains reduce net polarizability, as the spontaneous polarization for different grains align in a randomized direction to reduce the overall energy of the configuration. However, after application of an electric field, the polarization in each grain align and the hysteresis curve is present, although usually with a lower average value of polarization than for a single crystal, as the grains are unable to fully align due to a randomized orientation of crystallographic axes. This process is called poling, and the discovery of this process is what started the ferroelectric material research.

There is a temperature limit for ferroelectric materials, called the Curie temperature, T_C. Above the Curie temperature, the material becomes paraelectric. These materials can only be polarized by an electric field, and will lose polarization when the electric field is absent. This change from ferro- to paraelectric happens because ferroelectricity is a phenomenon of ordering within the material, and order is lost at the Curie temperature.

2.1.2 The crystallographic requirements of ferroelectricity

The crystallographic explanation of the ferroelectric crystal structure is more easily understood by first inspecting the crystal group that ferroelectrics belongs to, the piezoelectric

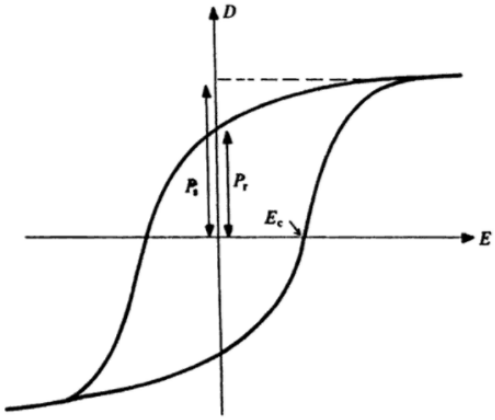

Figure 2.1: Hysteresis curve of a ferroelectric, with marked coercive field E_c, saturation polarization P_s and remnant polarization P_r. The figure is adopted from Glass and Lines.[14]

materials. Piezoelectric materials polarize from a uniform deformation of the crystal. The symmetry requirement for these materials is a polar point group, which is the absence of centrosymmetry. This is true in 21 out of the 32 crystal classes, where all except one exhibit polarity under stress. The reasoning for this requirement is simple to imagine: A crystal with a centre of symmetry will have all the charges moving symmetrically, so all the polar displacements is distributed evenly, giving no polarization within the unit cell. A piezoelectric material have no centre of symmetry, and a small deformation will result in a change in the charge distribution within the unit cell, which creates a dipole, which when aligned give the average polarization.

If there is one unique polar axis, this allows the formation of a spontaneous polarization with changes in the unit cell volume. This is the case for 10 of the original 20 crystal classes, called pyroelectric materials, as they will change polarization with temperature due to thermal expansion. For a pyroelectric material to be ferroelectric, the direction of polarization must be switchable. This is achieved by having a low transition energy between the two off-centered states.

2.1.3 The perovskite structure

The perovskite material has the chemical composition ABX_3, where A and B are the cations and X the anion, usually oxygen. In the oxides, the combined valency of the cations must be VI, which gives three different possibilities for cathode valency, describing the types: I-V, II-IV and III-III. The typical perovskite structure is centrosymmetric, and the material is paraelectric in this configuration. Below the T_C the centrosymmetry is broken by a small distortion. One of the cation sublattices is off-centered in relation to the anion sublattice, and the material becomes ferroelectric. This difference between the cubic, centrosymmetric and the tetragonal, non-centrosymmetric configuration is shown in figure 2.2.

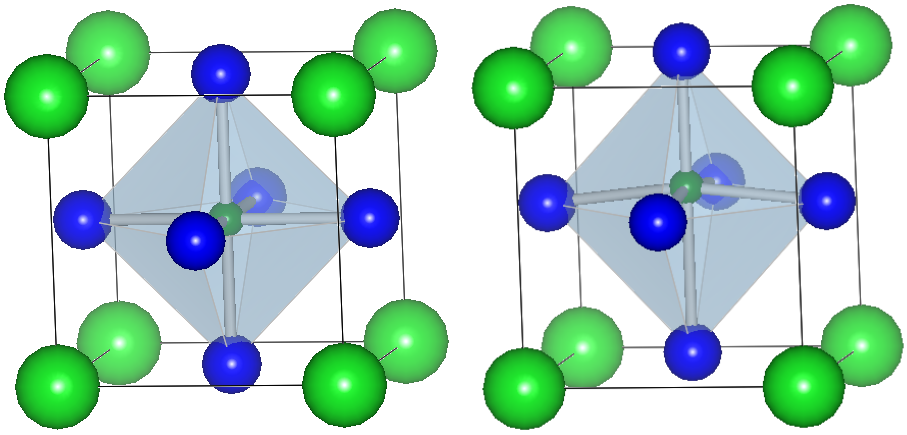

(a) (b)

Figure 2.2: $BaTiO_3$ unit cell. (a) Cubic, paraelectric unit cell (symmetry group $Pm\bar{3}m$), (b) tetragonal, ferroelectric unit cell, (symmetry group $P4mm$). The displacement of the Ti^{4+} ion along the z-axis is exaggerated. The figures are made in Vesta,[16] with parameters adopted from Lu *et. al.*[17] for the cubic and Rother *et. al.* for the tetragonal unit cell.[18]

The distortion is an off-centering of one of the cations, which is the result of a difference in cathodic radii, called the Goldsmith tolerance factor

$$t = \frac{r_A + r_O}{\sqrt{2}r_B + r_O}. \tag{2.1}$$

If the tolerance factor is slightly above one, the A cation is too large compared to the B cation, which is the smallest of the two. The B cation is not stable in the centre, and displace towards one of the anions to reduce the B-O bond. This displacement distorts the structure slightly, so the unit cell is elongated in the c-direction and becomes tetragonal instead of cubic.

The off centering in a perovskite is stabilized by the bond type, which has been shown to be a combination of ionic and covalent. A partly covalent bond between the 2p O orbital and the d orbital of the d^0 configuration of the B cation, essential for the displacement and for creating the dipole in the unit cell. Some ferroelectric materials, such as $PbTiO_3$, also have a covalent bond between the s-orbitals of the A cation and the O 2p orbital, while others, such as $BaTiO_3$ have a completely ionic bond between the A and the O. The covalent bond is only present in the tetragonal configuration, while in the cubic configuration, all bonds are ionic.[19,20,21] This covalent bond changes the electronic charge density, as shown in figure 2.3, stabilizing the off-centering of the B cation.

For the material to become ferroelectric, the displacement of the B cations must be along the same crystallographic axis and in the same direction, so that the polar displacements is aligned. Unaligned displacement axis or alternating displacement directions gives a dipole disorder, in which the local dipoles average to zero net polarization. There is now two possible phase transitions: A displacive, where the displacement of the B-

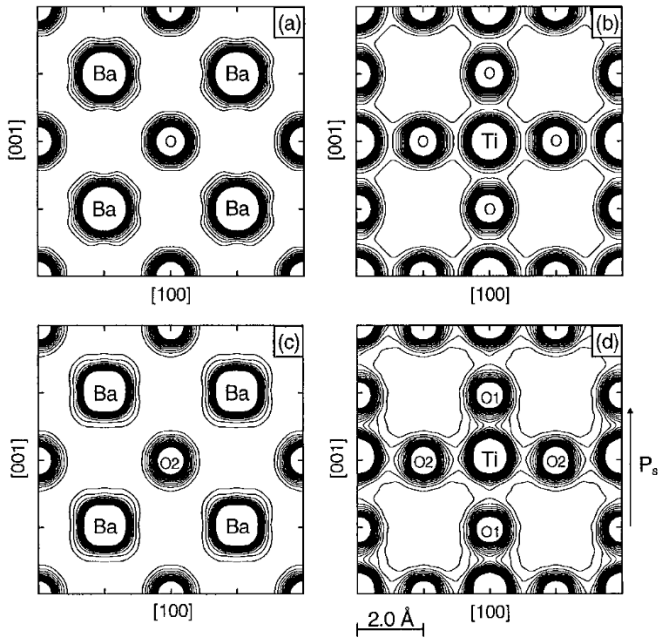

Figure 2.3: Electronic charge density of for $BaTiO_3$. The intersection shows the highest valence band, and a cross section of both the Ba-O plane and the Ti-O plane. The figure is adopted from Kuroiwa *et. al.*[20] (a, b) Cubic $BaTiO_3$ at 300°C, (c, d) tetragonal $BaTiO_3$ at 27°C.

cation is decreased, and an order-disorder, where the alignment of the unit cell dipoles are broken.[13,22]

2.2 Barium titanate

The first ferroelectric material was Rochelle salt, but it was with the discovery of $BaTiO_3$, 30 years later, that ferroelectrics emerged as an interesting field of study and possible applications became apparent.[14] It is still considered the model ferroelectric perovskite, and it is one of the most thoroughly studied materials even though the low Curie temperature limits use in technology.[23]

$BaTiO_3$ has a Goldsmith tolerance factor of about 1.06 and a c/a ratio of 1.01.[20] An early theory explaining the off centering of the small Ti^{4+} ion, is "rattling" in the oxygen octahedra.[24] Calculations by Cohen suggest otherwise, where a partly covalent bond between the O 2p orbital and the Ti 3d orbital, and the resulting competition between covalent and ionic forces gives the structural instability responsible for the off-centering of Ti^{4+} ion.[19] The crystal structure shown in figure 2.2 is of $BaTiO_3$.

$BaTiO_3$ has more than one phase transition, as shown in figure 2.4. From 0 °C to 120 °C, the material is in the tetrahedral phase, the symmetry group $P4mm$. The next phase

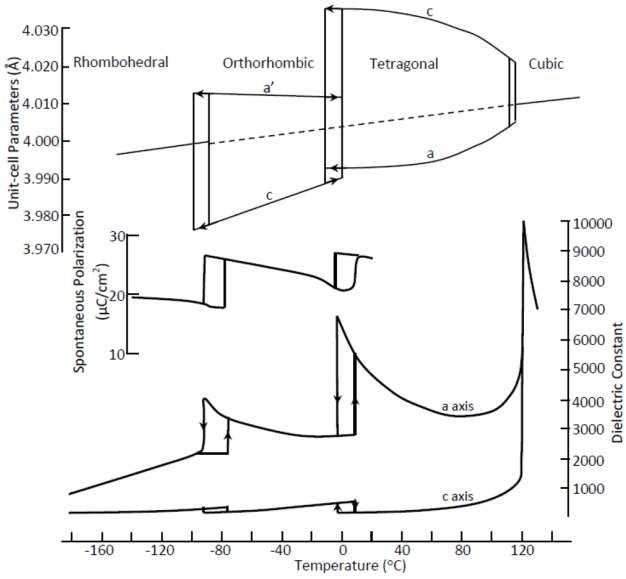

Figure 2.4: The phase transitions of $BaTiO_3$, showing both the structure (top), the spontaneous polarization and dielectric constant (bottom). Figure adopted from Aksel *et. al.*

transition happens at 0 °C, to the orthorombic crystal structure and the last at about -80 °C to a rhombohedral crystal structure. Around the temperature of the phase transitions, there is a considerable strain in the crystal, resulting in a larger dielectric constant. The low Curie temperature is the main reason for the limited industrial applications, but $BaTiO_3$ is considered the benchmark material for ferroelectric research.

The phase transitions of $BaTiO_3$ have long been assumed to be displacive, moving the Ti^{4+} ion back to the centrosymmetric position for the cubic phase. However, a local symmetry characterization by Senn *et. al.* show the Ti^{4+} displacement to be rhombohedral on the local scale. Such a rhombohedral displacement of the Ti^{4+} ion would be the result of a simultaneous shortening of three covalent bonds between the Ti 3d orbitals and the O 2p orbitals. The calculations use the displacive phase transition, where a disorder in the dipole ordering is the reason for the change in average structure at the phase transition, as shown in figure 2.5. The order-disorder is shown to be a good description of the phase transitions of $BaTiO_3$.[13]

2.3 Size effects in ferroelectrics

2.3.1 Ferroelectrictric structure at the nanoscale

A nanoscale component is usually defined as an object with at least one dimension limited to between 1 and 100 nm. A nanoparticle could be called a 0D object, as it is limited in three dimensions. An important feature of the nanoparticles is the increased ratio

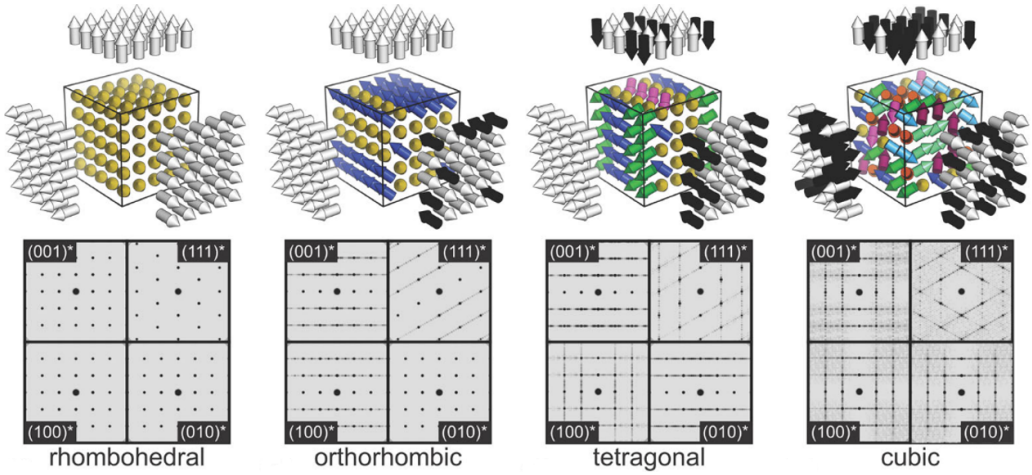

Figure 2.5: Monte carlo simulations of the phase transitions of $BaTiO_3$, where the polar vector projections along the 100 direction and the calculated diffuse scattering below, which gives diffuse planes in the reciprocal space. The black and white arrows show the polar projections along the different axis. The phase transitions are (a) rhomohedral, (b) orthorombic, (c) tetragonal and (d) cubic. Adopted from Senn *et. al.*[13]

between surface atoms and bulk atoms. A nanoparticle of 5 nm diameter has around 20% of the atoms on the surface. This is important as surface atoms behave differently than bulk atoms due to a lower coordination number, and will, in nanoparticles, substantially change the average properties of the material. One obvious effect is the the increased surface tension, or surface stress in a solid, which describes the tendency of a material to minimize the surface area. For a 10 nm gold nanoparticle, the surface tension is several GPa, which will give a noticeable contraction in the lattice parameter.[25]

The surface stress is not the dominating force in ionic nanomaterials, where a reduction in size gives a lattice expansion. There is a competition between the long-range, attractive Coloumb forces and the short-range ionic repulsion, which creates a negative pressure that increase with decreasing size.[26] This truncation of the Madelung potential is the origin of the increased lattice constant at the decreased size.[27]

Ferroelectricity has generally been assumed to have a size limit before disappearance. As the phase transitions in $BaTiO_3$ was expected to be displacive, where tetragonality is reduced by moving the displaced Ti^{4+} ion towards the unit cell centre, this was expected to be the case for the the size reduction as well. Early research mainly focused on finding an absolute size limit for ferroelectricity, and many papers report the fundamental size limit at widely different values.[28,29] The findings used to support this hypothesis is the observed anisotropic lattice expansion, where the crystal structure changes to a more symmetric configuration with decreasing sizes.[30] Studies of the ferroelectric perovskite $BaTiO_3$ show this as a reduction in the c/a ratio with decreasing crystallite sizes.[30,9] As shown in figure 2.6, some observations showed a full disappearance of tetragonality for nanoparticles. More sensitive measurements demonstrate tetragonality at lower sizes and

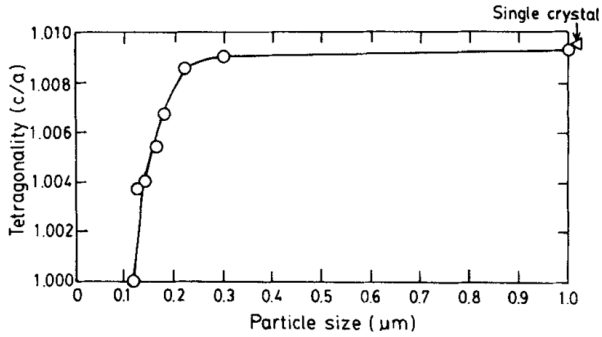

Figure 2.6: Reduction of the tetragonality c/a with a size reduction, where c/a reaches unity for a 100 nm particle. Figure adopted from Uchino *et. al.*.[9]

that this interpretation of the displacive phase transition for a size reduction is flawed. Smith *et. al.* and Page *et. al.* show that the displacement of the Ti^{+4} ion increases with a reduction in size. At the same time, the particles displayed a reduction in tetragonality, demonstrating that the return to centrosymmetry could not explain the reduction in tetragonality.

Smith *et. al.* found the the symmetry to be tetragonal at the local scale.[31] The partial covalency of the Ti−O bond is the stabilizing factor for the displacement, and it is not influenced by a size reduction. The unit cell will keep the deformation, which Smith *et. al.* suggest is tetragonal. The ionic expansion explains the increase of the dipole magnitude, as the partly covalent Ti-O bond that stabilizes the off-centering is not influenced by size reduction. The shortest Ti-O distance will therefore be constant with a reduction in size, while the ionic repulsion increase the other interatomic distances, increasing the local dipole magnitude.[27]

Page *et. al.* observe the Ti-O bonds in both bulk and 5 nm $BaTiO_3$ directly, characterizing the bond lengths that is responsible for the displacement, instead of looking at the effect on the metal-metal bonds that Smith *et. al.* observes. The nearest neighbour interactions of bulk $BaTiO_3$ is described better with a rhombohedral structure than a tetragonal.[22] At interatomic distances above 4 Å, the tetragonal crystal structure fits is shown to fit well, which is explained by to be an average of [111]-displacements in the +z direction. The 5 nm particles studied by Page *et. al.* have the PDF of the capping molecule overlapping with the low r-region of the spectra, and the article are not able to conclude that the displacement of Ti^{4+} ion is rhombohedral for the nanoparticle.

As the Ti^{4+} ion displacement is still present at the local scale, it is clear that something induces a disorder in the alignment of the dipoles, and that this is the explanation of the observed disappearance of ferroelectricity. The structural changes occurring from a reduction in size is therefore an order-disorder transition, and not a displacive transition, similar to the temperature dependent phase transitions described by Senn *et. al.*[13]

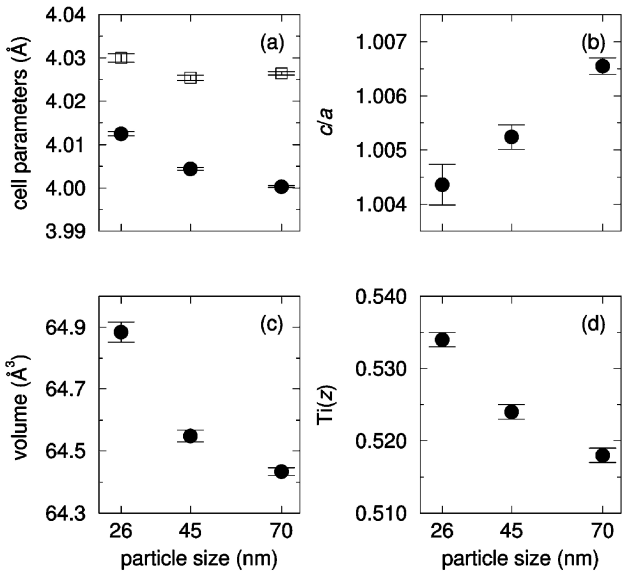

Figure 2.7: Changes in lattice parameters, tetragonality, unit cell volume and polar displacement of Ti^{4+} with reduction in particle size. Figure adopted from Smith *et. al.*.[31]

2.3.2 The driving force of ferroelectric disorder

The driving force behind the dipole disorder is not determined. Even though many articles look for the fundamental size limit for ferroelectrictiy, it could be useful to inspect earlier papers to find the proposed origin of the disappearance of ferroelectricity and examine if this could explain the change in the dipole order.

Akdogan *et. al.* mentions the nanoparticle core as the origin of the decreased polarization.[28] However, this paper suggests that the only other possible origin is surface tension, but if surface stress is responsible for the decreased tetragonality, it must be several GPa high. This is regarded as an unrealistic situation, and is therefore discarded by Akdogan *et. al.*. Calculations by Henry *et. al.* find the surface tension of a 10 nm nanoparticle to be 6.7 GPa, so the situation is clearly not as unrealistic as expected.[25]

Despite the high theoretical surface stress, the core could still be an influencing factor on the disorder. Discussion of these thwo possible origins are limited by a vagueness in most papers, where the actual physical effects are not mentioned. The influence of the core is briefly discussed by Ihlefeld *et. al.*[32] As ferroelectric ordering is a phonon mediated phenomenon, they argue that there must be a fundamental limit to the number of unit cells needed for a ferroelectric material, as a single unit cell does not have the dispersion spectrum needed. This is mainly investigated in thin films. Fong *et. al.* studied ferroelectric stability in $PbTiO_3$ films of one to four unit cell thickness.[10] They find a lower limit to ferroelectiricity at three unit cell thickness, which they explain as an effect of the surface reconstruction, shown in figure 2.8. At three unit cells, the middle layer still has a local structure of $PbTiO_3$, while a film of two unit cells will have surface reconstruction at both outer layers, giving no ordered ferroelectric structure. Fong

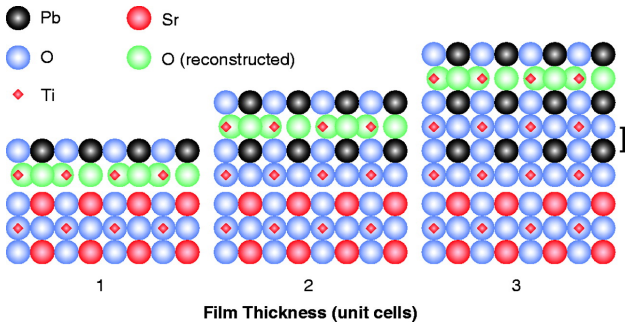

Figure 2.8: Surface reconstruction of the in a thin film with 1, 2 and 3 unit cells thickness. Figure adopted from Fong *et. al.*[10]

therefore concludes that if the structure is present, ferroelectric ordering is possible in a thin film. It should be noted that Fong *et. al.* finds a lower limit for $BaTiO_3$ at seven unit cells, and the difference is not explained. Fong *et. al.* cites the depolarization field as the stabilizing factor, which is discussed in length in section 2.3.3.

2.3.3 Depolarization field

The depolarization field in a ferroelectric material arises from unshielded surface dipoles, as shown in figure 2.9, and is the main candidate for the origin of size effects in the earliest experiments. This is discussed in length in two papers by Wurfel and Batra, investigating a ferroelectric-semiconducting interface. They demonstrate that the incomplete screening at the interface create a depolarization field which reduces the measurable polarization.[5,6]

Junaquera and Ghosez did calculations on an electrode-metal interface, to look into the critical role of the depolarization field in an electrode. The calculations was done on a $SrRuO_3{-}BaTiO_3$ supercell, periodically repeated in space, with the formula $[Sr{-}(RuO_2{-}SrO)_n/TiO_2{-}(BaO{-}TiO_2)_m]$. The n value was set at a level to avoid interaction between the two interfaces, and m was varied to simulate different thicknesses. The critical thickness of ferroelectric stabilization was found to be six layers. If the screening from the metal layer was infinite, the film would have bulk values for all the crystal structure parameters. However, the realistic interface would have incomplete screening from the metal, creating a sizable depolarization field and thus the observed dipole disorder.

The study by Fong *et. al.* has the notable experimental result of a measurable ferroelectricity in a 3 unit cell thin film. Instead of using electrodes to stabilize ferroelectricity, Fong *et. al.* uses a domain configuration, where the domains are lines with the polarization direction alternating in 180°in relation to each other. This is explained to neutralize of the depolarization field, which is suggested as the reason for the ferroelectric stability at the very low thickness.[10]

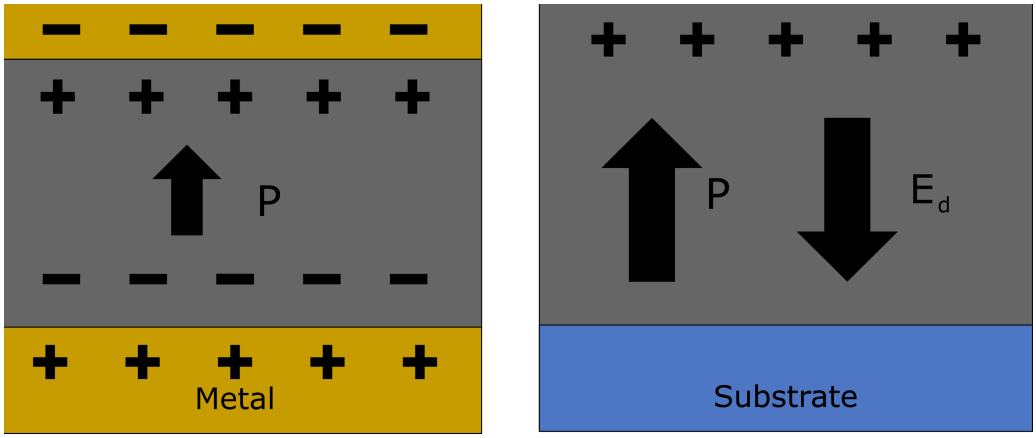

Figure 2.9: A simplified model of the depolarization field. (a) A perfectly screened ferroelectric thin film, with no depolarization field, (b) an imperfectly screened electrode with a polarization field reducing polarization in the material. Figure by author.

2.3.4 Dipole ordering in ferroelectric components

The dipoles in a ferroelectric material at the nanoscale can be ordered to stabilize local ferroelectric ordering over longer length scales. The simplest type of ordering is the stripe domain pattern demonstrated by Fong *et. al.* for thin films of $PbTiO_3$ on an insulating substrate. The stripes are domains of polarization perpendicular to the surface, which Fong suggest forms to reduce the depolarization field, with a line width that decrease with thickness of the film, as the depolarization field increases.

Schilling *et. al.* has done a study of more complicated polarization patterns. The calculations are done for the three different configurations of a striped pattern of alternating polarization directions, shown in figure 2.10b. This article investigates, among other, the hypothesis that the pattern develops to minimize the electrostatic surface energy. The analysis reveal that the quadrant configuration, as shown in figure 2.10b, minimizes the electrostatic surface energy. $BaTiO_3$ particles between 100 and 500 nm are observed to display this kind of domain configuration, as shown in 2.10a. The domain feature itself is shown to be insensitive to changes in the size, but the periodicity is related to the sidewall length.[33]

Other possible dipole ordering states is the vortex states, which have received a lot of interest in recent years with intensifying research. A ferroic material can rotate the magnetization or polarization around a point to reduce the magnetic or electric field, which creates a vortex state.[34]

Naumov and Fu has done a study of vortex-to-polarization simulations of PZT nanoparticles with an external electronic field perpendicular to the vortex plane.[35] The particles studied are small, between 3.6 to 10 nm in diameter and 5.6 nm in height. The initial state without an external field is a mixing of the polarization and the vortex state, as shown in figure 2.11. The polarization nucleates in the middle of the particle, creating a large polarization alongside the strong toroid moment. The formation of the polarization

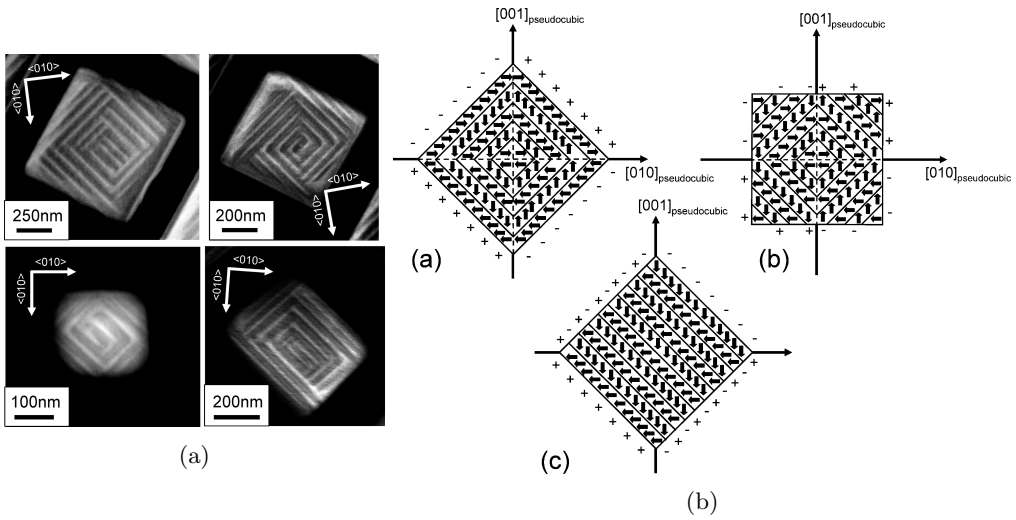

Figure 2.10: (a) Observed domain structure using STEM imaging of free standing $BaTiO_3$ nanoparticles, (b) Calculated energy of of domain patterns consistent with the domains in figure (a), displaying the surface charges.

in the centre is suggested to be initiated by the rotation of the dipoles near the cylindrical axis, as there is a large strain in the centre of the particle and the rotation reduces strain energy.

The vortex state for zero field in figure 2.11 has a c/a ratio below 1, and the dipoles are directed along the xy plane. When the field increases, there is a nucleation and growth of the polarized state in the middle of the particle, the c/a ratio will increase. The field giving a c/a ratio of about 1 is the same as transitioning the structure from phase 1, the strong toroid moment coupled with the strong polarization, to phase 2, which is a symmetry-broken version that has a y component in the toroid moment. This second phase have a different toroid phase, but Naumov and Fu comments that the polarization seems not to be affected greatly and is fairly stable.[35]

A similar calculation was done previously by Naumov *et. al.*, which studies the vortex states development in relation to variations in the height and diameter in the nanoparticles.[36] Two different phases arises, one fully circular for the nanodisc, where the diameter is larger than the height, and one periodically helical for the nanorods. This calculations only includes the toroid moment, and rarely goes in depth about the crystallographic signs of these states. Naumov *et. al.* does comment that the patterns is robust to surface termination, but at the same time both faces are ordered to minimize the depolarization field.

The simple stripe domain pattern and vortex states described here are not the only dipole ordering possible. The domains can be oriented differently in relation to the surface, helix-type vortex states or vortex rings have all been observed, as described in a review article by Gregg.[37]

There have been observations of nanoparticles with a single domain with dipole or-

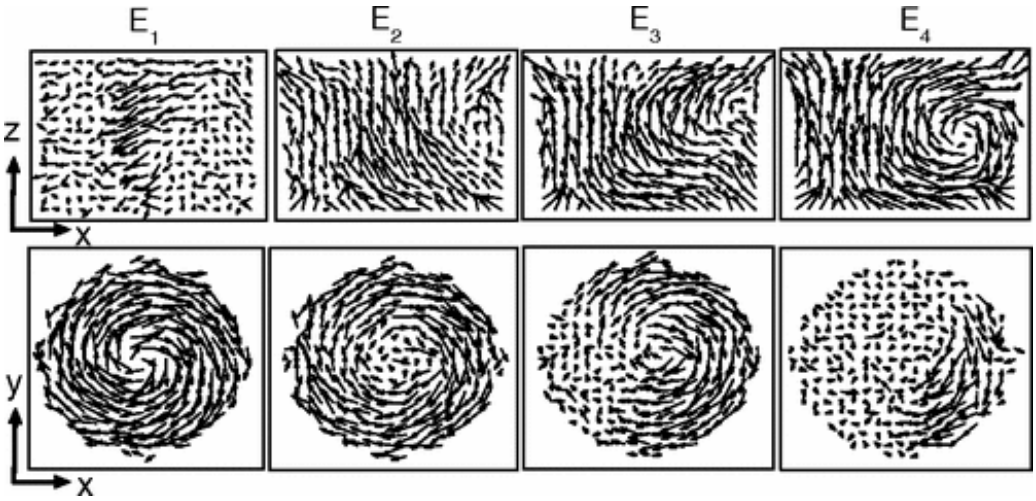

Figure 2.11: Calculated vortex states in a nanodisc for varying electric fields. The top row is along the z-axis and the bottom shows the xy-plane. Figure adopted from Naumov and Fu.[35]

dering along one axis. Polking *et. al.* has mapped the Ti^{4+} displacements on an approximately 10 nm $BaTiO_3$ nanocube and calculating the dipole magnitudes from the displacements, as shown in figure 2.12. The particle has a unified ordering along one axis, and a general disorder along the plane perpendicular to the polarization.

2.4 Characterization techniques

2.4.1 Total scattering and pair distribution function analysis

The pair distribution function (PDF) gives the atomic density as a function of radial distance. As nanoparticles usually display great deviations from the crystal models using space group symmetry to describe bulk crystals, PDF is an important tool for describing the structure of these highly disordered systems. The wavevector Q is related to the diffraction angle by $Q = 4\pi sin(\theta/\lambda)$. The reduced PDF, *G(r)*, is the fourier transform of the reciprocal space total scattering function *S(Q)*, related by

$$\begin{aligned} G(r) &= \frac{2}{\pi}\int_{Q_{min}}^{Q_{max}} Q(S(Q)-1)sin(Qr)dQ \\ &= 4\pi r[\rho(r)-\rho_0] \end{aligned} \tag{2.2}$$

where ρ_0 is the average atomic number density, *ρ(r)* is the atomic pair density and r is the interatomic distance. PDF is advantageous as it allows analysis in real space and gives structural information about both ordered and disordered materials.[38,39,40,41]

$BaTiO_3$ is the a well studied material, and PDF analysis has been shown to characterize the structure of nanoparticles with great result. Petkov *et. al.* used PDF to look

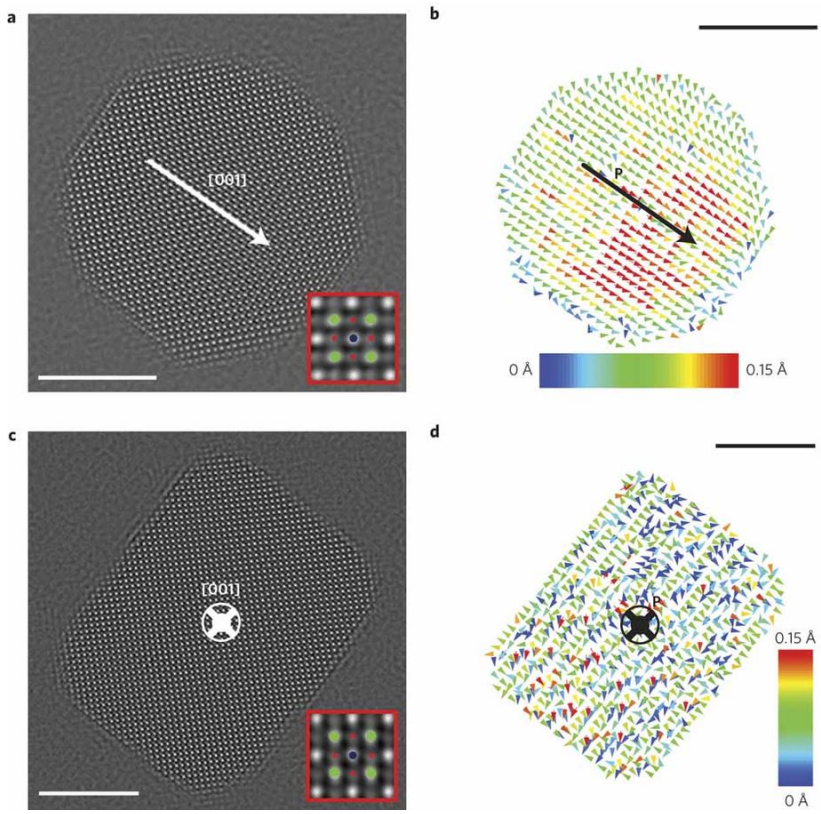

Figure 2.12: (a,c) Atomic resolution TEM of a single particle $BaTiO_3$. The scale bar is 5 nm in both figures. (b,d) Dipole moment calculated from mapped displacement of Ti^{4+} from the atomic resolution image in (a,d). Figure adapted from Polking *et. al.*[12]

into the structural coherence of $BaTiO_3$ between 5 and 1200 nm,[42] which is shown in figure 2.13b. The 5 nm particles has broader and less intense peaks, which is interpreted by Petkov *et. al.* to be due to an increasing structural disorder.

The coherence length is an important parameter, as it describes the length scales over which the dipoles order coherently. Calculating the coherence length is not trivial, which could be why the reported values are not consistent. Petkov *et. al.* reports a coherence length of about 20 Å for 5 nm $BaTiO_3$ particles, while Polking *et. al.* find that a spherical 10 nm $BaTiO_3$ particle have a coherence length of about 10 Å.[12] The latter show that coherence length depend on the surface energy of the particles, as it includes the nanocubes with a coherence length of 20 Å for 8 nm nanocube and 40 Å for a 15 nm nanocube. The surface of a cubic particle is flat and has a low energy crystal plane exposed, which could be why they have a much longer coherence length than spherical particles of the same size, which have a much more irregular surface. Polking *et. al.* proposes the use of different particle morphology as a possible way to study the surface without the depolarization field, but the method assumes that the surface energy does not

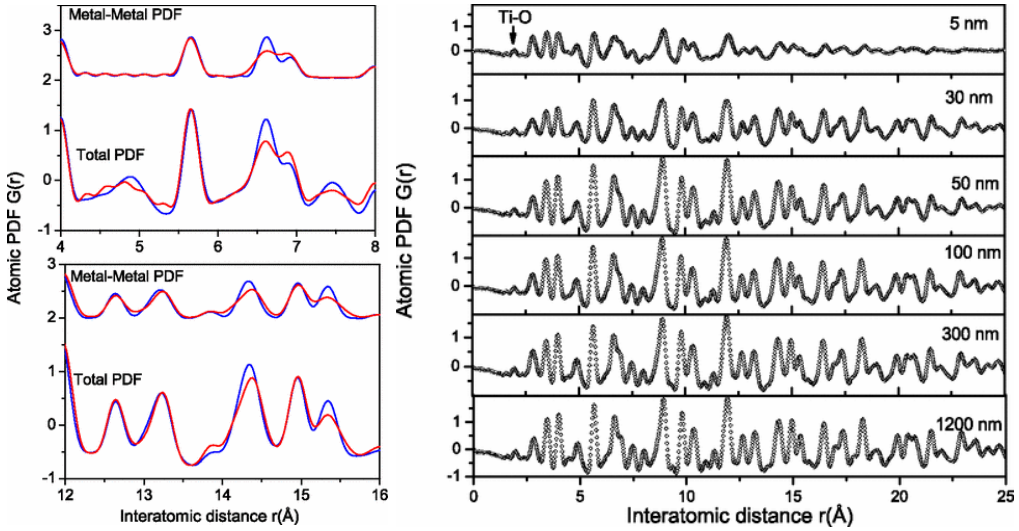

(a) (b)

Figure 2.13: (a) Model of the structure for two low regions Å for both tetragonal (red) and cubic (blue). (b) Experimental atomic PDF for nanoparticles between 5 and 1200 nm. Both figures adapted from Petkov *et. al.*[42]

have any influence on the depolarization field. It should also be noted that cubic particles actually have a higher surface to volume ratio than spherical particles of corresponding size. The high energy surface is mentioned as the reason for the high internal stress in the spherical particles, and states this as the reason for the disorder. It is not clarified if the surface interactions refers to the electrostatic boundary conditions or surface stress.

The PDF of $BaTiO_3$ described by the tetragonal $P4mm$ and the cubic $Pm\bar{3}m$ symmetry can easily be calculated, which gives a greater insight into the origins of the changes in the PDF, as Petkov *et. al.* demonstrates in figure 2.13a. The Ba-Ba bonds does not behave differently, and the differences in atomic density is expected to originate in the bonds corresponding to the Ti ion. The first pronounced difference is the higher r-shoulder of the peak at 6.5 Å, which is more pronounced in the tetragonal structure. The intensity difference of the peaks at 14.3 and 14.9 Å is also related to the model used. In the cubic model both these peaks have the same intensity, but the tetragonal model gives two peaks with the same intensity.

Smith *et. al.* uses PDF analysis to show the increased displacement of the Ti^{4+} ion with decreasing size. The analysis is done only for the metal-metal bonds, as the oxygen have a very weak scattering power.[31] The displacement of Ti^{4+} and the c/a ratio is likely to be correlated, so atom-atom distances should be used as a basis for the analysis, defining a distortion parameter by

$$\frac{(\mathrm{Ba{-}Ti})_{\mathrm{long}} - (\mathrm{Ba{-}Ti})_{\mathrm{short}}}{(\mathrm{Ba{-}Ti})_{\mathrm{long}} + (\mathrm{Ba{-}Ti})_{\mathrm{short}}} \tag{2.3}$$

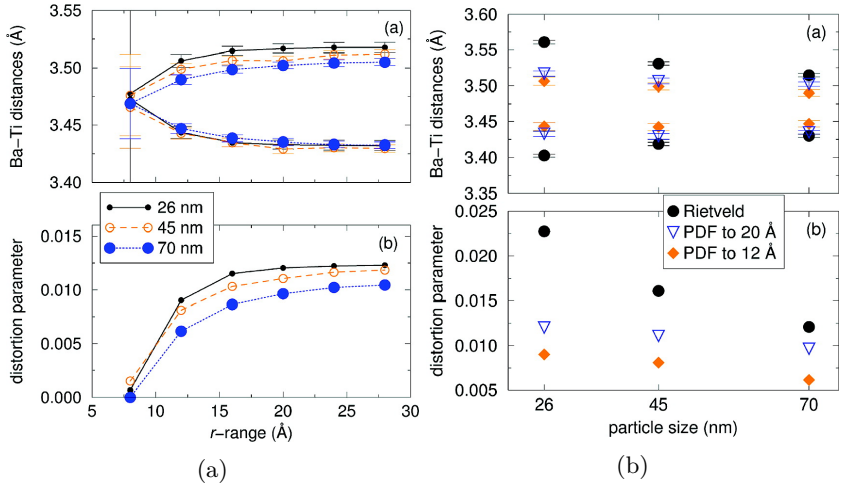

(a) (b)

Figure 2.14: (a) Evolution of PDF refinements for Ba-Ti distances and a distortion parameter for varying r-ranges. (b) Long and short distances of Ba-Ti and a defined distortion parameter. Results from both Rietveld refinement and fitted PDF for different r-ranges are displayed. Figure adapted from Smith *et. al.*[31]

The bond lengths is correlated with the length scale used for the refinements and vary little with the particle size, which is shown in figure 2.14. The atomic distortions is higher for the higher ranges, which is the opposite of the expected result, as low r-regions should have a higher accuracy on atomic distortions. The evolution of the displacement is similar for the different particle sizes, which suggest a dependence on the modelling, and not a size effect. Smith *et. al.* concludes that larger fit ranges is needed for accurate structural fits, and shows that the distortion parameter is constant from about 16 Å.

$BaTiO_3$ display a broadening with a reduction in size, which is related to the strain, but the structure retains order on the local scale. It is useful to compare this with the local structure of a system where the local order is lost at the nanoscale. One type of structure displaying this loss of structural coherence is $BiFeO_3$, where the Bi-ions goes through a "melting" where all Bi-ions displace in a completely disordered fashion, giving the smeared out PDF pattern shown in figure 2.15.[43] This is how a PDF pattern looks, if the structural coherence of one sublattice is completely lost.

A nanoparticle is expected to be a highly strained system, and the strain should therefor also be characterized. The atomic displacement parameter (ADP) includes the strain, through both thermal vibrations and structural disorder at the lattice site.[44] A very large ADP value will signify that the model is unable to model the atomic displacement, which will in turn indicate a higher degree of strain.

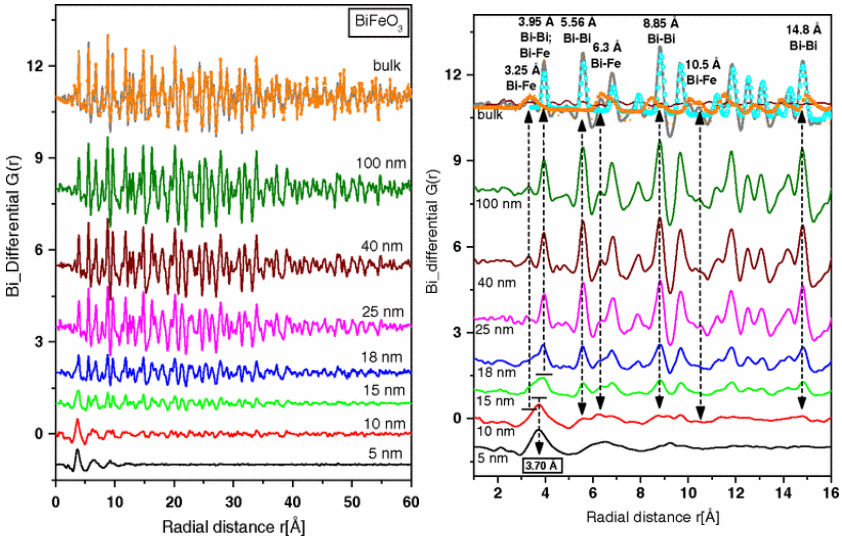

(a) (b)

Figure 2.15: (a) Full experimental PDF for different sized $BiFeO_3$ (b) Analysis of size dependent changes in the low r-range of $BaTiO_3$, with different bonds marked in the top spectra: Bi-O (broken line), Bi-Fe (brown) and Bi-Bi (cyan). Both figures adopted from Petkov *et. al.*[43]

2.4.2 Raman spectroscopy

Raman spectroscopy is a measurement technique used to characterize the structural fingerprint for materials. The technique exploits the inelastic scattering of light from a material, also called Raman scattering. Ultra-violet, visible and near IR-light excites the electrons in the material into a virtual electronic state. This state is unstable and the electron relaxes by re-emitting a photon. The situation where the electron is both excited and relaxes into the ground state, and the incident and re-emitted photon is of the same energy, is called Rayleigh scattering, which is elastic. Raman scattering is inelastic scattering, some of the energy of the excited electron excites a vibrational state. The incident and re-emitted photon have an energy difference corresponding to a vibrational state, which gives structural information about the material because the vibrational states possible are dependent on the structure. If an electron is excited from the ground state, and the re-emitted photon is of lower energy than the incident, it is called a Stokes shift, and this is normally used for Raman spectroscopy. The other possibility is an Anti-Stokes shift, where the electron is excited from an excited vibrational state, and re-emitted to the ground state.[45]

For a material to be Raman active one or more vibrational states must be Raman active, meaning the the molecule must change polarizability with the vibration. Vibrations are a result of the bond length, so Raman spectroscopy offers more local information than a method like XRD, which interacts with atomic planes. However, phonos are a collective

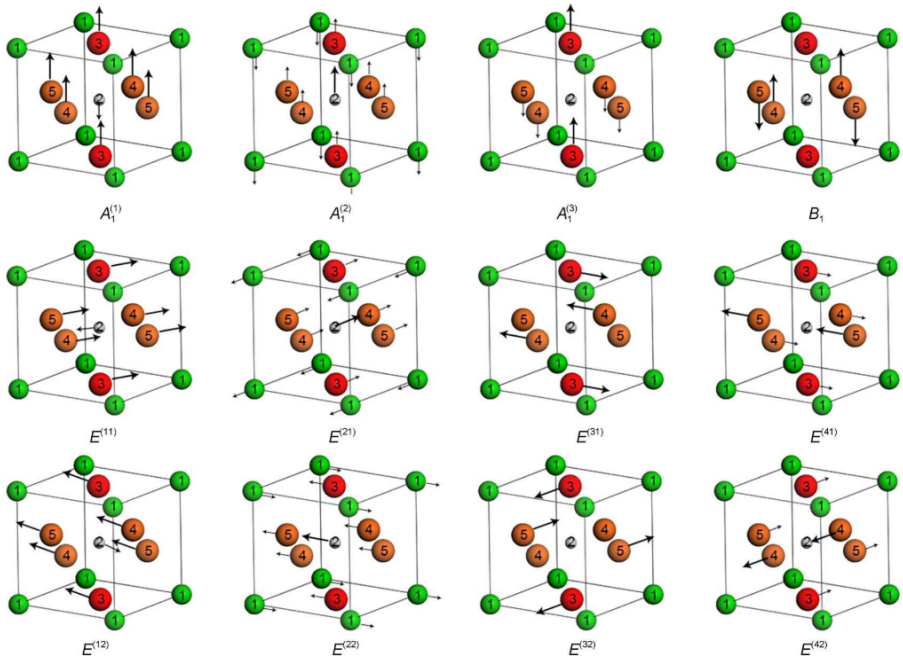

Figure 2.16: Optical vibrational modes of $BaTiO_3$. The A and E modes displace all atoms, while the B_1 mode only displaces O2, which is the oxygens in the xy-plane. This mode is called the wing-flapping mode, referring to the alternating directions of the O atoms. This mode is used by Smith *et. al.* to characterize the degree of disorder in the tetragonal phase.[31] Adopted from An *et. al.*[46]

phenomena, so the method does not give a fully local structure information.

Calculating the peaks in a Raman spectra requires many considerations, and there is some variations in the reported spectra in the literature. In addition, the Raman spectra are heavily influenced by size effects, which will increase the variations even more.

$BaTiO_3$ is Raman active in the tetragonal state. Calculations done by An *et. al.* find eight Raman active modes, which is shown in figure 2.16.[46] Due to overlapping in peak positions, this results in six peaks identified when fitting the theoretical spectra with the experimental data, shown in figure 2.17. The Raman spectra of $BaTiO_3$ has an uneven baseline and broad peaks, due to soft modes and the splitting of transverse and longitudal modes at similar frequency for some modes.

A temperature series of $BaTiO_3$ show how the peaks shape is influenced both by size and disorder.[31] Cubic $BaTiO_3$ should be completely inactive due to symmetry considerations, but broad peaks are visible around 260 and 530 cm^{-1}. These are generally attributed to Ti^{4+} disorder, which is present at all sizes and temperatures.

The peak centered at around 300 cm^{-1} is the best indicator of the tetragonal state,[31] which correspond to the wing flapping mode from An *et. al.*, shown as B_1 in figure 2.16. The peak line width is shown to broaden with decreasing size, which is interpreted to

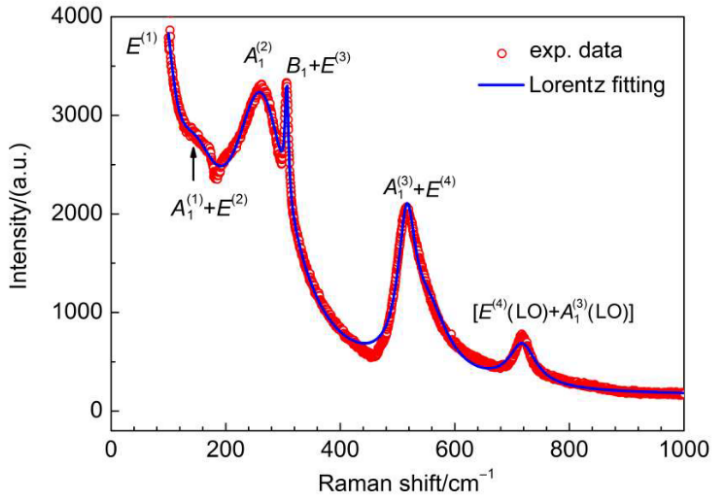

Figure 2.17: Raman spectra from 70 to 1000 cm^{-1}. The measured data is in red and the calculated spectra is in blue.

indicate the presence of a tetragonal phase with a decreased structural coherence.

Below 200 cm^{-1} there will be peaks corresponding to $BaCO_3$. This is important as most synthesis routes for $BaTiO_3$ will have some impurities from $BaCO_3$, as the formation energy of the latter is lower.[31]

There is large changes in the peak at around 300 cm^{-1} for sizes at about 22 nm.[47] The spectra of the particles from 10 nm to 33 nm is shown in figure 2.18b, where especially the size evolution of the peak at 300 cm^{-1} is an important feature. The 33 nm particle has a very sharp peak at 306 $^{-1}$ from the wing flapping mode, and a very broad peak at about 250^{-1}. For the smaller particles, from 22-10 nm, the sharp peak is decreased and the feature of the broad peak is not as visible, which is interpreted to be a combining of the peaks from the tetragonal and the cubic phase. From 22 nm and up, there is evidence of a local tetragonal structure, but as the peak is impossible to distinguish from the broad Ti^{4+} disorder peak it is impossible to comment on the degree of tetragonality.

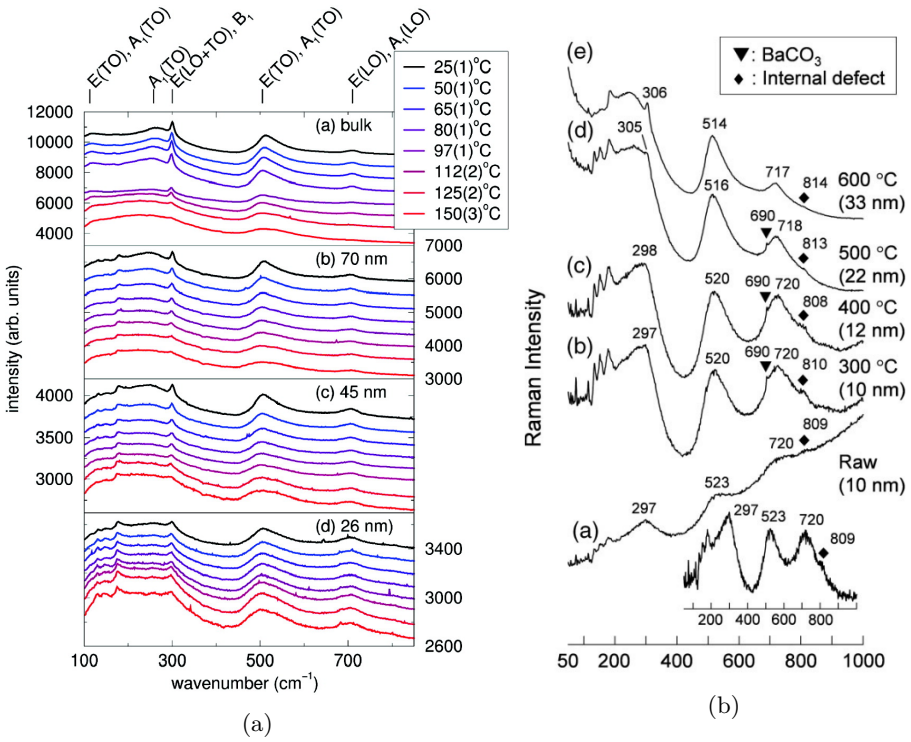

Figure 2.18: (a) Raman spectra at different temperatures for $BaTiO_3$ of different sizes. Figure adopted from Smith *et. al.*[31] (b) Raman spectra of $BaTiO_3$ particles from 10-33 nm. Figure adopted from Shiratori *et. al.*[47]

Chapter 3

Experimental

3.1 Hydrothermal synthesis

The $BaTiO_3$ nanoparticles was made by hydrothermal synthesis, which is a method where the reaction takes place in a closed container with water heated to a temperature between its boiling point and critical point. The increased pressure allows temperatures above the boiling point, and increases the reaction kinetics.

All chemicals used in the synthesis is summarized in table 3.1, and the standard hydrothermal synthesis process is shown in figure 3.1. The experimental protocol used was a modified combination of the recipes described by Dalod *et. al.*[48] and Rørvik *et. al.*.[49] Table 3.2 is a summary of the samples with the sample name, amount of chemicals and reaction conditions. Sample w80 was made by adding titanium isopropoxide (TIP, 8g) to 79.5 ml water and then stirred. Barium nitrate was added to give a Ba to Ti 1:1 ratio. To precipitate $BaTiO_3$, the pH was raised to 14 by adding KOH (21g). The solution was poured into an autoclave that was heated to 125°C for 2 hours before it was washed with water and the sample dried over night at 100°C.

The other barium titanate samples were synthesized after a method more similar to the recipe described by Rørvik *et. al.*, with some modification.[49] TIP (3.05 ml, 0.01 mol) was added to 20 ml 1.5 M aqueous citric acid and stirred at 60°C until the solution turned clear, which was after about 4h. The pH was raised to 5 by addition of ammonia. Barium nitrate (2.61g, 0.01 mol) was added to the solution and then stirred until clear, about 10

Table 3.1: List of chemicals used in hydrothermal synthesis.

Chemical	Molecular formula	Purity [%]	Manufacturer
Titanium(IV) isopropoxide	$Ti[OCH(CH_3)_2]_4$	97	Sigma-Aldrich
Barium nitrate	$Ba(NO_3)_2$	99.999	Sigma-Aldrich
Citric acid	$C_6H_8O_7$	$\geq$ 99.5	Sigma-Aldrich
Potassium hydroxide	KOH	90	Sigma-Aldrich
Ammonium hydroxide	NH_4OH		VWR Chemicals

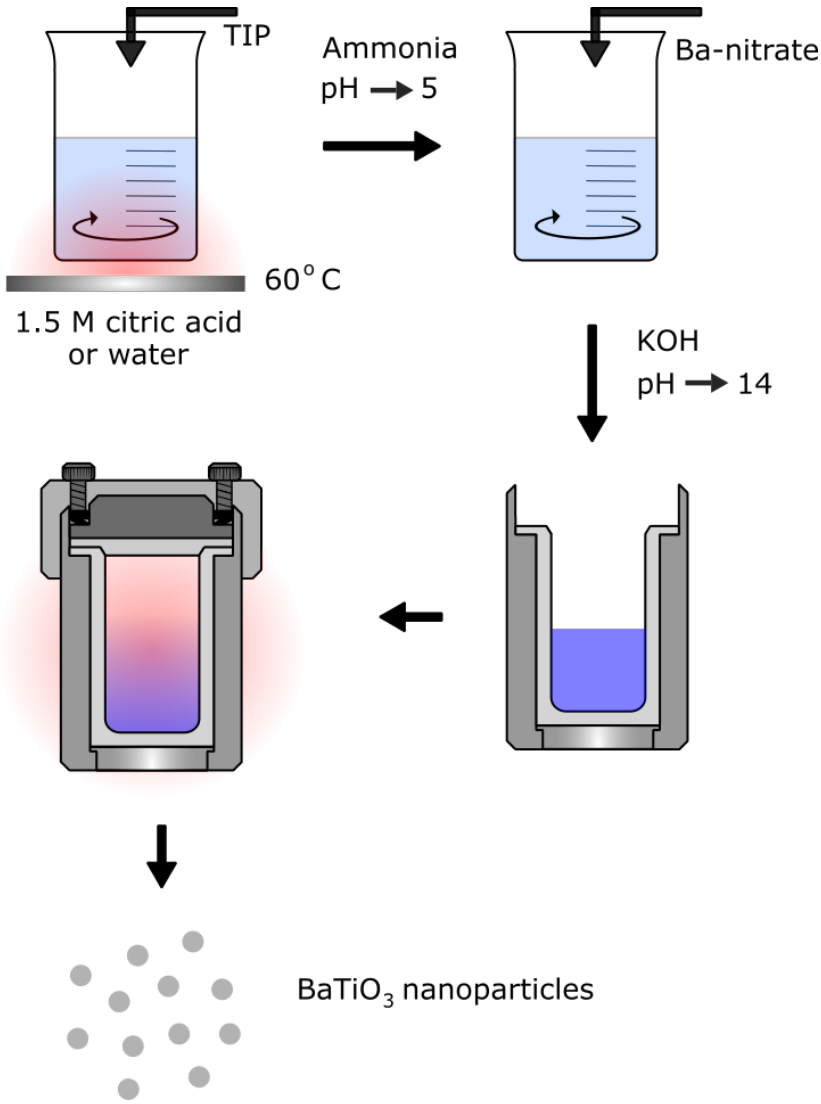

Figure 3.1: Flow chart showing the standard hydrothermal synthesis of $BaTiO_3$ nanoparticles. Only the unchanged parameters is included, while heating time, temperature and precursor concentration is summarized in table 3.2.

Table 3.2: Hydrothermal synthesis parameters and chemicals for $BaTiO_3$ synthesis. The complexing agent (CA) is citric acid.

Name	TIP [ml]	$Ba(NO_3)_2$ [g]	H_2O [ml]	CA	NH_4OH [ml]	KOH [g]	Time [h]	Temp [°C]
Ref	3.05	2.61	20	1.5 M CA	∼3.5	10	2	125
w20	3.05	2.61	20	-	-	10	2	125
w80	8	6.85	79.5	-	-	21	2	125
T-150	3.05	2.61	20	1.5 M CA	∼3.5	10	2	125
t-0.5	3.05	2.61	20	1.5 M CA	∼3.5	10	2	125
Ann-800	6.04	5.17	10	1.5 M CA	∼3.5	10	2	125
Ann-900a	3.05	2.61	20	1.5 M CA	∼3.5	10	2	125
Ann-900b	3.05	2.61	20	1.5 M CA	∼3.5	10	2	125

Table 3.3: Hydrothermal synthesis parameters and chemicals for $BaTiO_3$ synthesis.

Name	Annealing temperature [°C]	Annealing time [h]	Heating/Cooling rate [°C/hour]
Ann-800	800	2	200
Ann-900a	900	2	200
Ann-900b	900	2	200

minutes. The pH was raised to 14 by addition of KOH (10g). It was poured directly into an autoclave and heated to 125°C for 2 hours. The powder was then washed with water and dried over night at 100°C. The described recipe is used as the standard, sample "ref", and all modifications was done with this as a reference. The modifications was done to the standard recipe, summarized in table 3.2, which is expected to influence the particle size.

This recipe uses citric acid as a complexing agent, which was expected to give a more homogenous particle size distribution and a smaller size than the particles without a complexing agent. Some modifications were made to give spherical particles instead of the novel structures described by Rørvik, and therefore ethylene glycol and SBDS were excluded. The access to carbon should be limited, which increases the possibility of producing $BaCO_3$ instead of $BaTiO_3$, and stirring time of the solution before pouring into the autoclave was reduced, to avoid the uptake of carbon by KOH.

Annealing

Three of the samples was annealed after the hydrothermal synthesis to increase the particle size. The annealing parameters is summarized in table 3.3. This heating program was adopted from Uchino et. al.[9]

Table 3.4: The dielectric constants of the dispersion mediums.

Medium	Dielectric constant	Temperature
Oil[51]	3	25°C
Water[52]	78	25°C
eGaIn	-	-

3.2 Dispersion mediums

Three dispersion mediums was chosen to provide different levels of electrostatic shielding for the surface charges. The mediums was chosen as they have about an order of magnitude difference in the dielectric constant, which is summarized in table 3.4. Deionized water and olive oil are both simple to use and have very few HSE concerns.

Gallium and indium have an eutectic point of 75 wt.% Ga and 25 wt.% In, which gives a liquid metal at about room temperature.[50] Metals does not have a dielectric constant as they are conductive and therefore not polarizable, and will have superior shielding properties.

3.3 Characterization

3.3.1 X-ray Diffraction

Three different X-ray diffraction experiment was conducted, as the requirement for the sample preparation is very different for the dry particles, the particles dispersed in liquid and the particles covered by eutectic indium gallium. The dry particles need to adhere to the Si-wafer, the samples with dispersed particles needs to avoid evaporation and the eGaIn covered particles needs to be a thin layer to reduce cost, giving the three sample preparations shown in figure 3.2.

Sample preparation of the dry particles was done by dispersing the particles in ethanol, dripped on a flat Si-wafer, before the ethanol was evaporated and the sample was put into a rotating sample holder and scanned. This is explained in figure 3.2a.

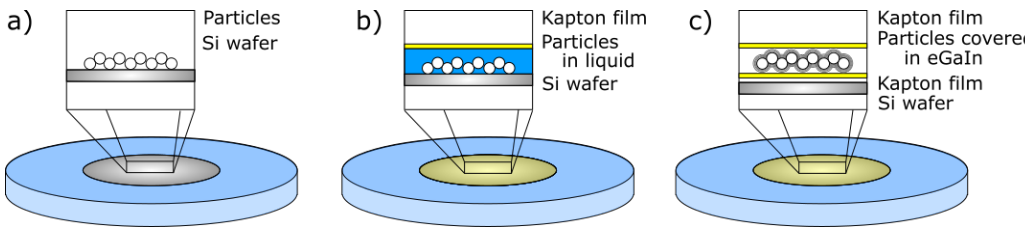

Figure 3.2: (a) Sample preparation for dry particles, evaporating the ethanol to leave only dry particles on a Si wafer. (b) Sample preparation of the particles dispersed in oil or water, under a kapton film. (c) Sample preparation of the eGaIn covered particles, where the particles are in between two kapton films.

Table 3.5: (a) Atomic positions tetragonal $BaTiO_3$, cited from Rother.[18]

Symmetry group		*P4mm*	99
Lattice parameter	a	b	c
	3.995	3.995	4.039
Atom	x	y	z
Ba	0	0	0
Ti	1/2	1/2	0.4883
O1	1/2	1/2	0.0247
O2	1/2	0	0.5139

The particles dispersed in oil and water used the same sample preparation. A high concentration of particles and the respective liquid was mixed together dispersed on top of a Si wafer. The dispersion was then covered by a kapton film to avoid evaporation and reduce spill. This is shown in figure 3.2b.

The particles dispersed in eutectic indium gallium was stirred together, so that the liquid metal coated the particles. The a thin layer of the coated particles was then placed between two kapton films, as shown in figure 3.2c.

Diffraction was done on the dry particles in a D8 Focus diffractometer with CuKα radiation with a LynxEye SuperSpeed Detector and a 0.2 mm slit, from 20°to 120°2θ with 2.5 seconds per step and a step size of 0.01428°, which gives approximately a 5 hours scan. This was run twice per sample and the two diffractograms was accumulated.

A different machine was used for the particles dispersed in oil, water or eGaIn, since the liquid needed an instrument with 2θ-2θ to avoid spilling of the liquid. These was scanned in a D8 A25 DaVinci X-ray Diffractometer with CuKα radiation with a LynxEye SuperSpeed Detector and a 0.3 mm slit, from 20°to 120°2θ with 2.5 seconds per step and a step size of 0.01435°. This also gives an approximately 5 hour long scan, which was run twice per sample and the two diffractograms was accumulated.

Rietveld refinement and Pawley fit

The diffraction pattern for the dry particles was analyzed with Topas v.5, and the crystallite size is calculated by Rietveld refinement, which is a method that fits the measured diffraction pattern to a pattern calculated from a crystal with a symmetry described by a space group. The starting points of the calculations was the values adopted from Rother *et. al.* for tetragonal $BaTiO_3$.[53]

The crystallite size from the Rietveld refinement will only be used as input parameters for the further Pawley refinements, but as the peak broadening for size should not be overestimated, other parameters is refined as well: Scale, sample displacement, lattice parameters a and c, size broadening described by a Lorenzian function, and the polar displacement along the z-axis for Ti^{4+} ion and both O^{2-} ions. Only the tetragonal crystal structure *P4mm* is used to determine size, as it is expected to describe the larger particles better. Descriptions of the crystal system is given in table 3.5. It is important to note that the calculated crystallite size will be the same as the grain size in a polycrystalline material, and the same as the particle size in a single crystalline particle.

Table 3.6: (a) Atomic positions for cubic $BaTiO_3$, cited from Lu *et. al.*[17]

Symmetry group		$Pm\bar{3}m$	221
Lattice parameter	a	b	c
	4.009	4.009	4.009
Atom	x	y	z
Ba	0	0	0
Ti	1/2	1/2	1/2
O	1/2	1/2	0

Pawley refinements was done for the dry particles, in addition to the particles dispersed in oil, water and eGaIn. These refinements does not calculate the intensity from structural information, but uses it as a free parameter. Thus, the atomic positions in the unit cells can not be fitted using the Pawley refinement and the simpler fitting method reduces the chance of overfitting.

The particles is fitted to both a tetragonal crystal structure $P4mm$ and cubic crystal structure $Pm\bar{3}m$, using the input parameters from Rother *et. al.* for tetragonal $BaTiO_3$[53] and from Lu *et. al.* for cubic $BaTiO_3$.,[17] described in in table 3.5 and 3.6. The tetragonal is fitted for scale, sample displacement and the lattice parameter a and c, while the crystallite size uses the input value from the Rietveld refinement. The cubic is fitted for scale, sample displacement, lattice parameter a and the strain broadening modeled by a Lorenzian function, with the same crystallite sizes as an input.

3.3.2 Background fitting

As background subtraction could remove vital information from the diffractogram, background fitting should be done in Topas. A series of fits to a tetragonal structure with the fixed values from Rother *et. al.* is done, only increasing the amount of coefficients describing the background and reporting the agreement factor R_{wp}.

3.3.3 Synchrotron X-ray Diffraction

Synchotron powder diffraction data was collected at the SPring-8 facility in Japan, at the BL08W beamline, using high energy X-rays. The total scattering data needs a high Q range for a good PDF description, which is why high energy X-rays is necessary, as described in section 2.4.1. The detector used was a XRD1621 AN3 produced by PerkinElmer, with a screen of 2048x2048 pixels, with $200\mu m/pixel$ resolution.

The particles dispersed in the oil or water was put in a 1.0 mm quartz capillary, as shown in figure 3.3a. A reference sample with dry particles was measured as well, in addition to three capillaries for background subtraction was measured: empty, water and oil.

The raw data sets was integrated into a 1D diffraction pattern from the pattern shown in figure 3.3b, using the program PIXIA. A calibration was made using a CeO_2 sample, which gave the sample-detector distance, panel tilt and beam center, in addition to an effective wavelength of 0.1071 nm and a distance between the sample and the detector of

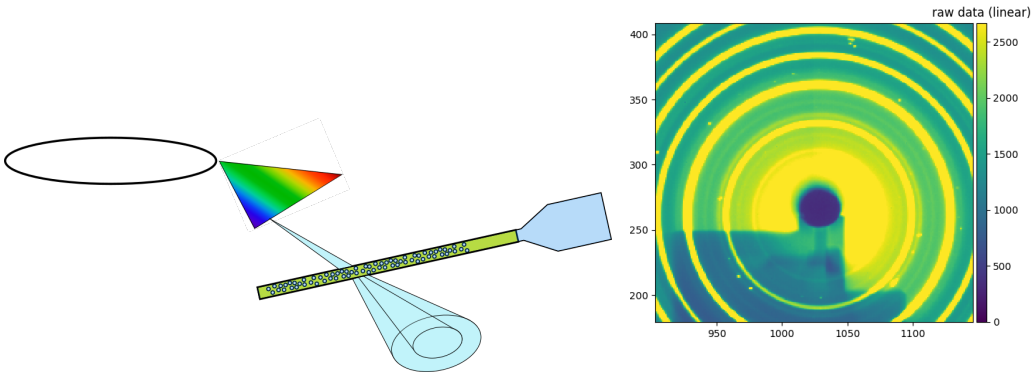

(a) (b)

Figure 3.3: (a) A capillary filled with particles and dispersion medium radiated by synchotron radiation, producing the 2D pattern, (b) the 2D pattern from the total scattering X-ray diffaction, which is integrated to give a 1D diffraction pattern.

532.6195 mm. The calibration using CeO_2 was done in PDFgui. The Fourier transform was done in MaterialsPDF with a Q_{max} of 30, with additional background subtraction of either the dispersion medium or the empty capillary. The programs used is a part of the Orochi project, and the conversion follows the method described by Tominaka *et. al.*[40,41]

The fit to the calculated PDF for a space group symmetry was done in PDFgui, using the same input parameters as the for the Pawley fits.[18,17] The parameters for the fits using the cubic $Pm\bar{3}m$ symmetry was the scale factor, the Q_{damp}, the atomic displacement parameter (ADP) and the lattice parameter a, while the fits using the tetragonal $P4mm$ symmetry was the same, with the additional lattice parameter c and polar displacement of Ti^{4+} in the z-direction. A separate fit was done with the ADP instead of the displacement of Ti^{4+} for the tetragonal structure. All parameters was fitted simultaneously at the r-range 20 to 40 Å.

These results of the 20 to 40 Å fit range was used as the input parameters for fits for three smaller r-ranges: 0.1 to 8 Å, 8 to 16 Å and 16 to 24 Å. To stabilize the refinements, each parameters was fit individually with the other parameters fixed to the values from 20 to 40 Å.

3.3.4 Raman spectroscopy

The Raman spectroscopy was made using a Renishaw InVia Reflex Spectrometer System using a blue 532 nm laser.

Two different Raman series was done. The first comparing two different dispersion mediums, where the particles was heated at 200°C and left over night to remove surface adsorbed species, before a high concentration of particles was dispersed in the respective liquids and dripped on to a glass plate.

The second Raman series was done to compare the influence of the dispersion medium thickness on top of the particles, which are heavier and will sink to the bottom. Water

and particles was mixed with a low particle concentration and a droplet was dripped on a glass plate and scanned. The sample was then left until most of the water was evaporated, leaving only a slurry of particles, and scanned again.

The analysis was done by comparing the Raman spectra visually after normalization for a selected peak, the peak at 500 cm^{-1}. An additional comparison of a single peak was made by normalizing for the maxima and comparing the different spectra for the same particle in different liquids.

No background removal for the dispersion mediums was done, as it could remove important information from the system. The peaks from both the oil and the water dispersed samples is expected to be either before 100 cm^{-1} or after 1000 cm^{-1}, which will then be excluded from the analysis.[54,55]

3.3.5 Scanning electron microscope particle characterization

As the Rietveld refinement only determine the crystalline size, a particle size characterization was done using scanning electron microscope (SEM), which is an imaging technique that scans a surface with a focused electron beam. This have the advantage of finding the particle morphology in addition to the particle size. The SEM used was the S-5500, which is an in-lens cold field emission electron microscope. Both dry particles and particles covered in eutectic Ga-In was characterized.

Chapter 4

Results

4.1 Particle characterization

The dry particles was fitted by Rietveld refinement to determine the crystallite size, which is summarized in table 4.1, and the Rietveld fits are shown in the appendix B. These crystallite sizes were used as input parameters for the Pawley refinements.

The observed diffractogram have peaks corresponding to $BaCO_3$, which is present in varying degrees for all samples, visible as the peak around 24 °, which is shown in the reduced range in figure 4.1b.

The SEM imaging characterizing particle size was limited by the low vacuum, which prevented clear images at the length scale needed for individual particle characterization. Some images of the larger magnification is provided in appendix D. Neither particle size or particle morphology can be determined from these images, and the following discussion can therefore only use the crystallite size from the Rietveld refinements, as it is impossible to determine if the particles are single crystalline with no grains.

Table 4.1: Calculated crystallite size from Rietveld refinement

Sample	Crystallite size [nm]
Ann900a	94
Ann-900b	76
Ann-800	40
w80	34
w20	24
T-150	20
Ref	15
t30	11

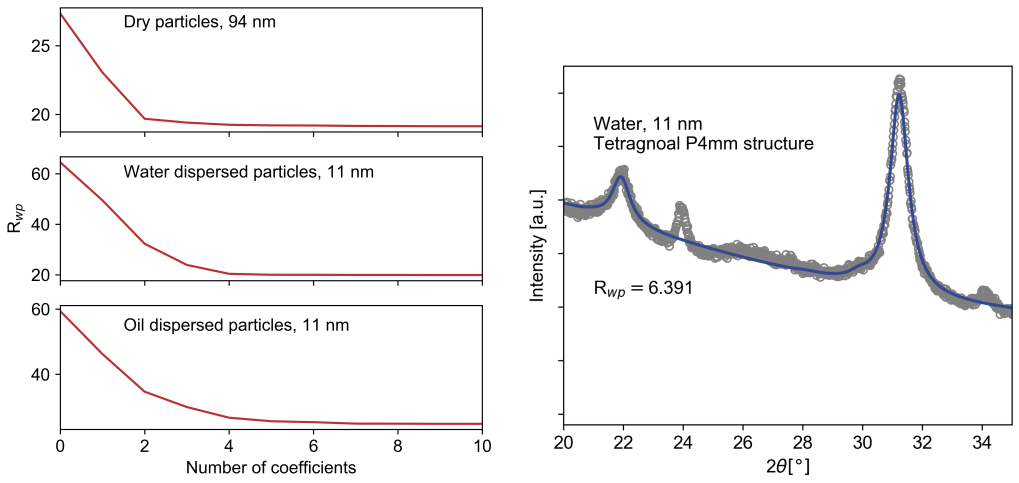

(a) (b)

Figure 4.1: (a) Changes in the quality of fit R_{wp} as a function of number of coefficients in the background. (b) Calculated spectra for tetragonal $P4mm$ symmetry and data for the 11 nm crystallites, reduced spectra from 20 to 35 2θ where the largest mismatch between calculated fit and background data, which is in the range 25-28 2θ.

4.2 Pawley fit on dispersed particles

4.2.1 Background fits

The relationship between the number of coefficients used to model the background and the R_w is shown in figure 4.1a. All types of samples was found to be well modelled at around 6 coefficients, but the calculated spectra is not able to model the background properly, as can be seen in the mismatch in figure 4.1b. Two additional coefficients was added, and all fits was modeled with 8 coefficient for the background.

4.2.2 Pawley fit of particles dispersed in oil and water

The Pawley fits for the 94 nm and the 11 nm crystallites, dispersed in both oil and water is shown for a reduced 2 θ range in figure 4.2 and 4.3, while the full range of 20 to 120 2θ is summarized in appendix A. The 11 nm crystallites have less intense maxima and the background feature is more dominating, in addition to the expected peak broadening from the reduction in size.

The resulting structural parameters of the Pawley refinements for dry, oil and water dispersed $BaTiO_3$ nanoparticles are shown in figure 4.4, where the dry particles are included and will be used as a reference for the influence from the dispersion medium. The particles dispersed in eutectic gallium indium will be discussed separately in section 4.2.3, and is excluded from the further discussion.

The Pawley fits using a cubic $Pm\bar{3}m$ symmetry display an increase in the lattice parameter for smaller crystallite size. The increase reaches a plateau at a smaller crystallite size, with very little expansion between the 15 nm and 11 nm crystallites. The largest difference in the lattice parameter is between the 20 and 24 nm crystallites.

The Pawley fits using a tetragonal $P4mm$ symmetry display an anisotropic expansion, where the a and the c parameter scale differently with size. The a parameter display a similar trend as the lattice parameter for the fits using the cubic symmetry, where the largest difference of expansion is between the 24 and 20 nm crystallites. The 15 nm crystallite has the largest value for the a lattice parameter, as the 11 nm crystallite display a reduction in the a parameter. The lattice parameter c parameter follows a very different trend with the size reduction than the a parameter. There is a slight reduction from the 94 nm crystallite to the 40 nm crystallite, and further size reduction gives a steady increase of the lattice parameter c.

The unit cell volume show a similar trend for the fits using both symmetry models. Fits to cubic symmetry has a trend is comparable to the trend of the lattice parameter a, there is a large increase between 24 and 20 nm crystallites, with a reduction in the expansion rate for the smaller crystallites.

The crystallites fit to the cubic symmetry uses lattice strain as a fit parameter, which is shown to not scale linearly with size. The 94 nm crystallites display the largest strain, followed by the 24 nm crystallites and then the 11 nm crystallites. The 41 nm, 20 nm and 15 nm crystallites have the lowest degree of strain, with very similar values.

The fits using tetragonal symmetry do not use the strain parameter for the fit, as tetragonality, expressed in the c/a ratio, is highly correlated with strain, where the trend mirrors the strain trend for the cubic symmetry. There is a large variations in both strain and tetragonality depending on the dispersion medium, but no conclusions about the influence of the dispersion medium can be drawn from these results due to the correlation between the two parameters.

4.2.3 Pawley refinement of particles dispersed in eutectic gallium indium

The results of the Pawley fits of the particles dispersed in eGaIn is shown in figure 4.5, with the dry particles as a reference. The strain and the tetragonality is excluded from the analysis, as discussed in section 4.2.2. The lattice parameters and unit cell volume of both the tetragonal $P4mm$ and the cubic $Pm\bar{3}m$ symmetry is very similar for both the dry and the eGaIn particles.

The dispersion was characterized by SEM imaging, which is shown in figure 4.6. The imaging shows aggregated particles on the surface of the metal. The dispersion have a large degree of aggregation of $BaTiO_3$ particles on the surface of the eGaIn. There might be areas where the particles are better dispersed, but there is such an amount of particles aggregated at the surface with limited wetting that the signal should be expected to be dominated by these unwetted particles. The similarity of the lattice parameters for the dry and the eGaIn dispersed particles supports the theory that the particles are not in contact at the surface, and the dispersion medium does not influence the particles.

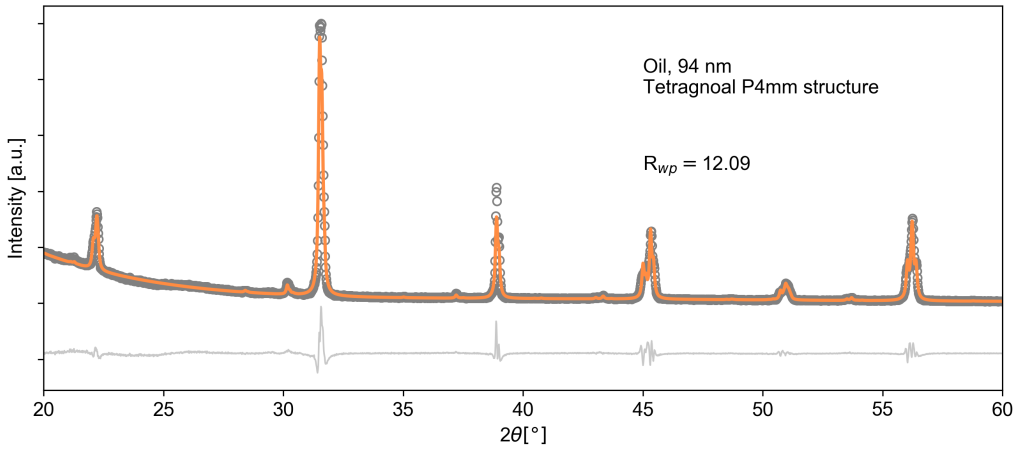

(a)

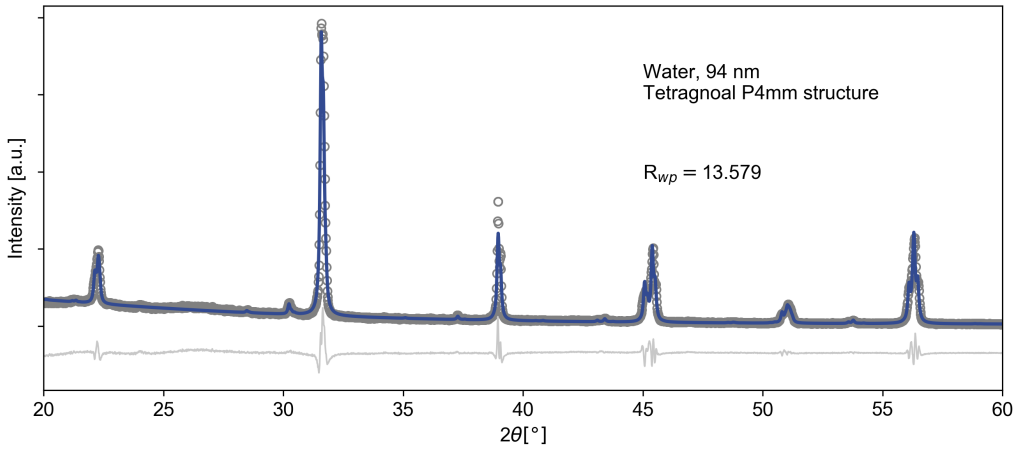

(b)

Figure 4.2: Pawley fits of the 94 nm crystallites dispersed in (a) oil (yellow) and (b) water (blue), showing the range between 20 and 60 2θ. The data as circles, the Pawley fit as the colored line and the difference between fit and observed data offset in grey.

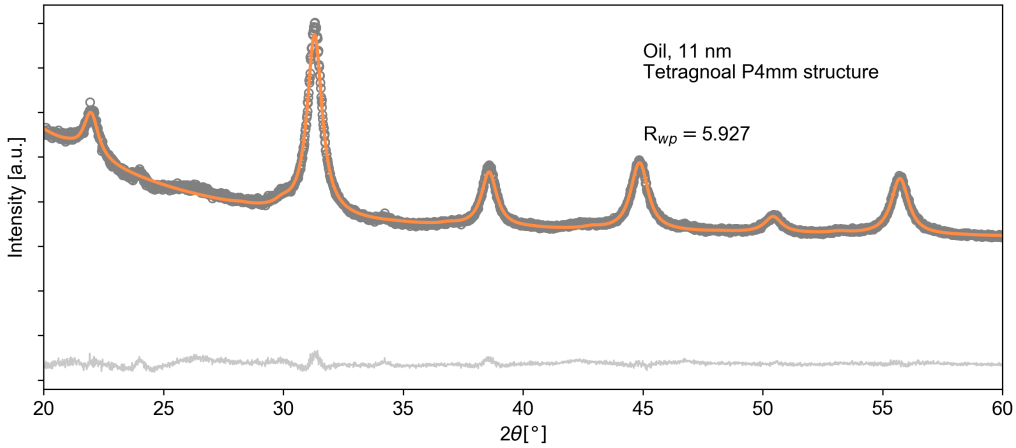

(a)

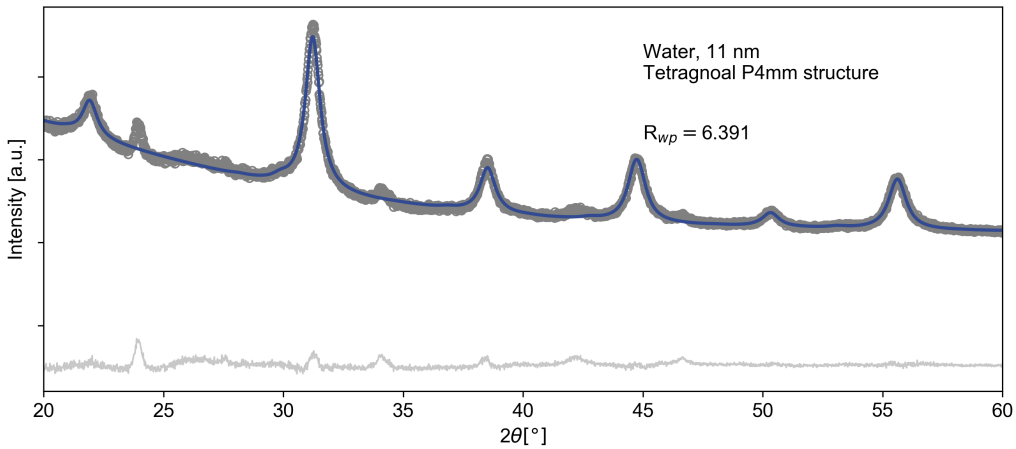

(b)

Figure 4.3: Pawley fits of the 11 nm crystallites particles dispersed in (a) oil (yellow) and (b) water (blue), showing the range between 20 and 60 2θ. The data as circles, the Pawley fit as the colored line and the difference between fit and observed data offset in grey.

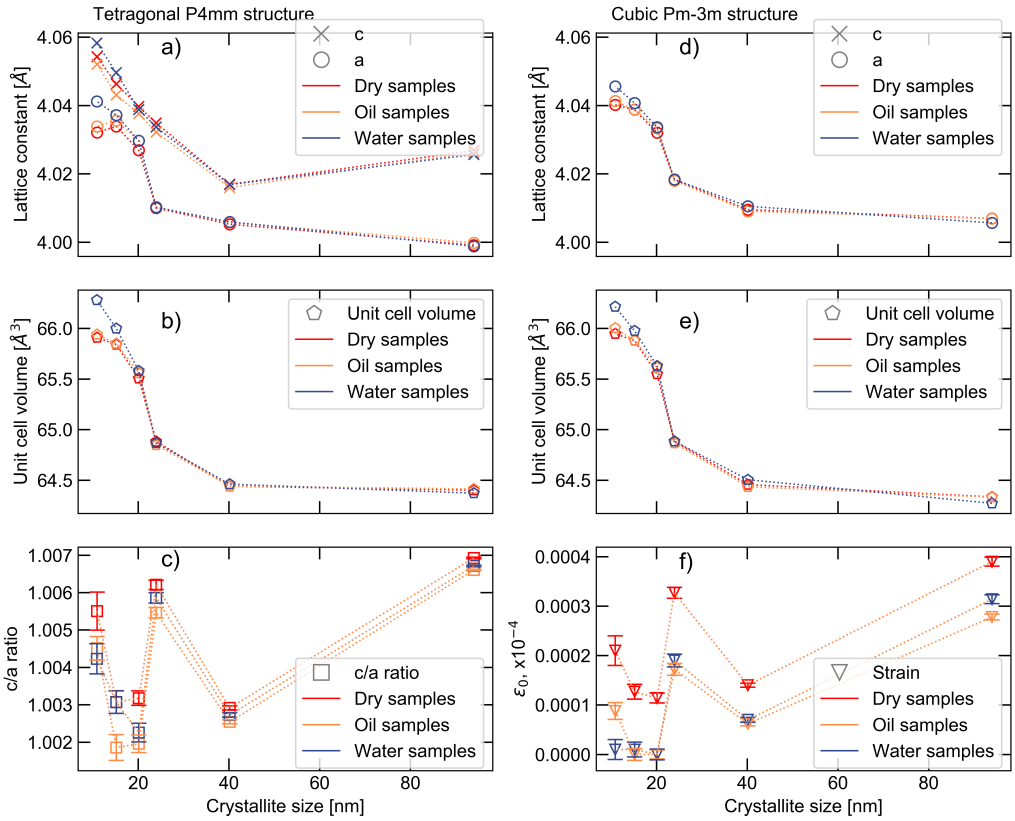

Figure 4.4: Results from the Pawley refinements of $BaTiO_3$ nanoparticles of 79 nm, 31 nm and 11 nm, displayed for dry particles (red), dispersed in oil (yellow) and water (blue). The symmetry models are (a-c) tetragonal $P4mm$ and (d-f) cubic $Pm\bar{3}m$ symmetry: with (a, d) lattice parameters, (b, e) unit cell volume, (c) tetragonality in the c/a ratio and (f) degree of strain. The errorbars for the lattice parameters a and c and for the unit cell volume are within the marker, and is therefore excluded for simplicity.

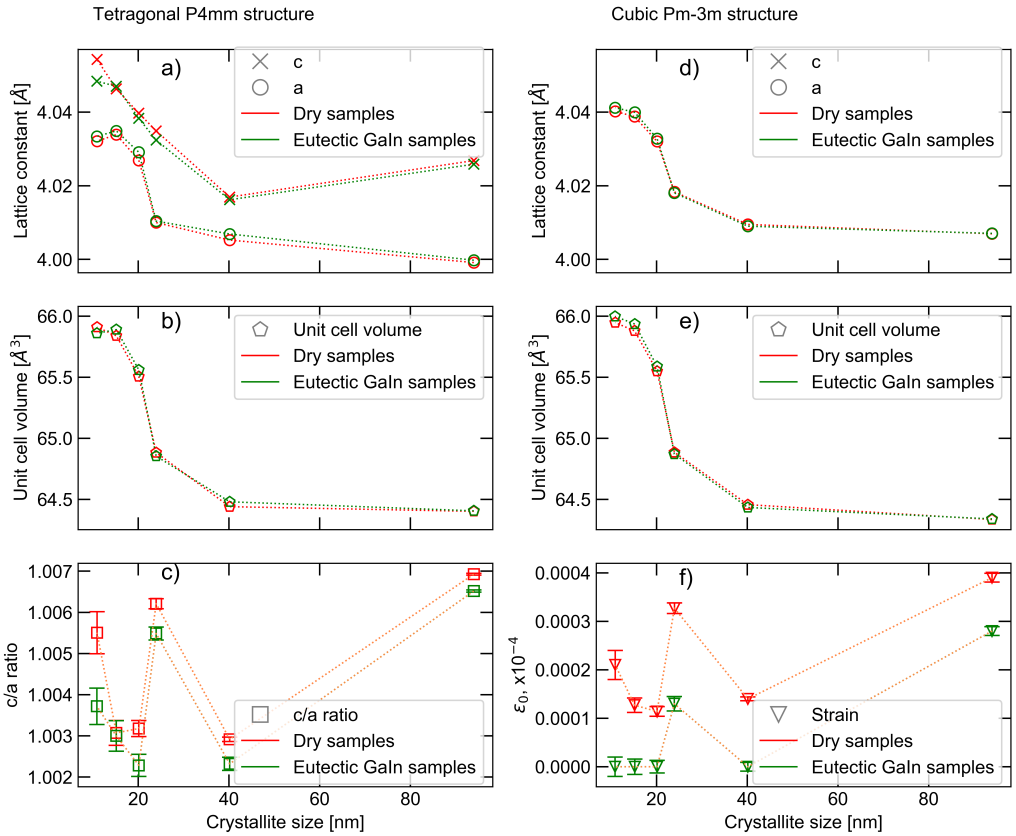

Figure 4.5: Results from the from Pawley fits for dry particles (red) and eutectic GaIn (green). The symmetry models are (a-c) tetragonal $P4mm$ and (d-f) cubic $Pm\bar{3}m$ symmetry: with (a, d) lattice parameters, (b, e) unit cell volume, (c) tetragonality in the c/a ratio and (f) degree of strain. The errorbars for the lattice parameters a and c and for the unit cell volume are within the marker, and is therefore excluded for simplicity.

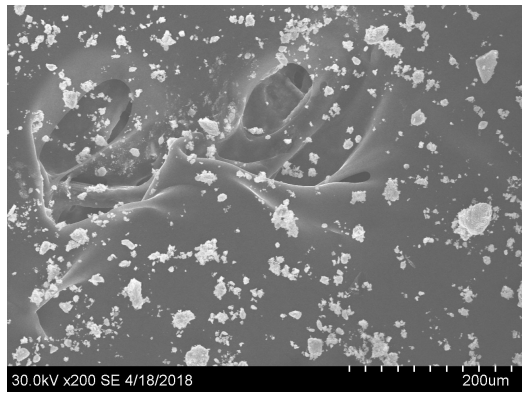

Figure 4.6: SEM image of a dispersion of 41 nm $BaTiO_3$ particles in eutectic gallium indium, where the particles are the bright aggregates with liquid metal visible as brighter features in the background.

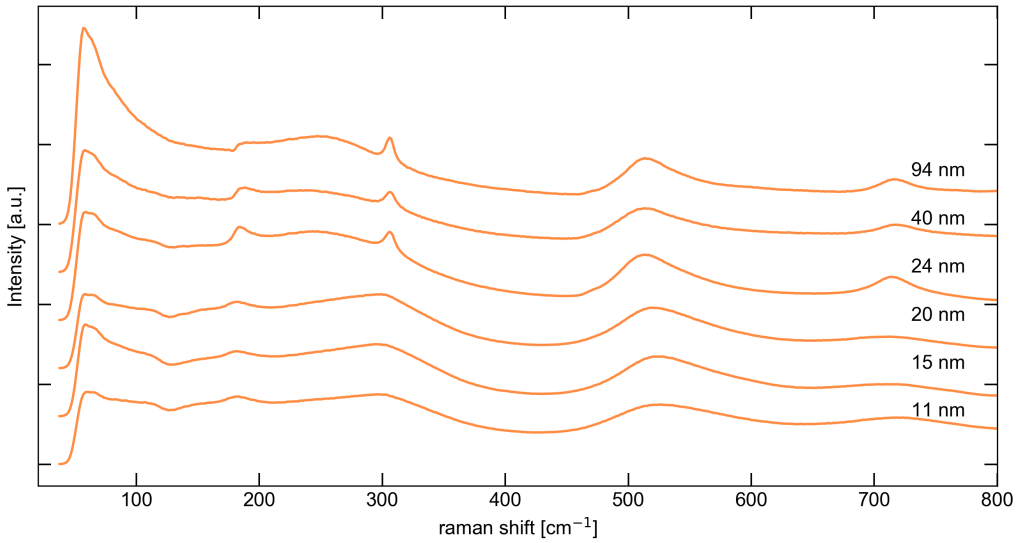

Figure 4.7: Full raman spectra for $BaTiO_3$ nanoparticles dispersed in in oil (yellow).

4.3 Structure characterization from Raman spectroscopy

4.3.1 Size dependence

The Raman spectra for $BaTiO_3$ show the uneven baseline, with broad peaks at 50 cm^{-1}, 180 cm^{-1}, 510 cm^{-1} and 710 cm^{-1}. The plots are normalized for the peak at 510 cm^{-1}, which allows comparison of the relative intensity within the spectra. The larger 94, 40 and 24 nm crystallites have a sharp peak at 308 cm^{-1} and a broader peak at 250 cm^{-1}. The crystallites under 20 nm has no visible peak at 250 cm^{-1} or sharp peak at 308 cm^{-1}, but a very broad feature at around 300 cm^{-1}. The peaks at both 510 cm^{-1} and 710 cm^{-1} gradually broaden with size reduction.

The peak at 50 cm^{-1} is much more intense for the 94 cm^{-1} crystallites than for the smaller ones. The intensity does not scale completely with size, while the 40 nm, 24 nm and 15 nm crystallites have a very similar intensity, the 20 nm and the 11 nm crystallites slightly less intense, but similar to each other.

The peak at 180 cm^{-1} is somewhat irregular. The three smaller crystallites have a very similar profile, but the 24 nm particle displays a very sharp 180 cm^{-1} peak. The peak at 40 nm is a little less intense, while the 94 nm particle have a large reduction in intensity.

The continuing analysis will only concern peaks over 200 cm^{-1}, as the frequencies under will have peaks corresponding to $BaCO_3$.

4.3.2 Influence of liquid layer thickness on Raman spectroscopy

The influence of the dispersion medium layer thickness is compared for the water samples, to determine if the peak shape and relative intensity is influenced by the thickness of the dispersion medium layer. It is important to know if the layer thickness influence is significant before the dispersion medium comparison, as sample preparation variations might influence the resulting Raman spectra.

The peak shapes are compared in figure 4.8, where the individual peaks are normalized for the peak maxima. The influence of the water layer follows no clear trend, as seen in the 500 cm^{-1} peak where the two layers alternate in what is the most intense when following the size reduction. The influence of the thickness of the water layer is not clear, and the origin of the variations is inconclusive, but the effect is not large enough to dominate the signal in relation to other effects and will be assumed to be negligible.

4.3.3 The influence of dispersion medium

A comparison between the full spectrum of the samples dispersed in oil and water are shown in figure 4.9, where the samples are normalized for the peak at 180 cm^{-1}. The 94 and the 40 nm crystallites have a very similar profile, where the samples dispersed in oil have reduction in the intensity above the peak at 308 cm^{-1} compared to the particles dispersed in water. The 24 nm crystallites have very similar spectres for both oil and water dispersion, although with a slightly higher intensity for the dry particles.

The broad peak at 300 cm^{-1} and the 510 cm^{-1} peak does show a large intensity difference relative to the normalized 180 cm^{-1} peak for the 20 and 15 nm crystallites.

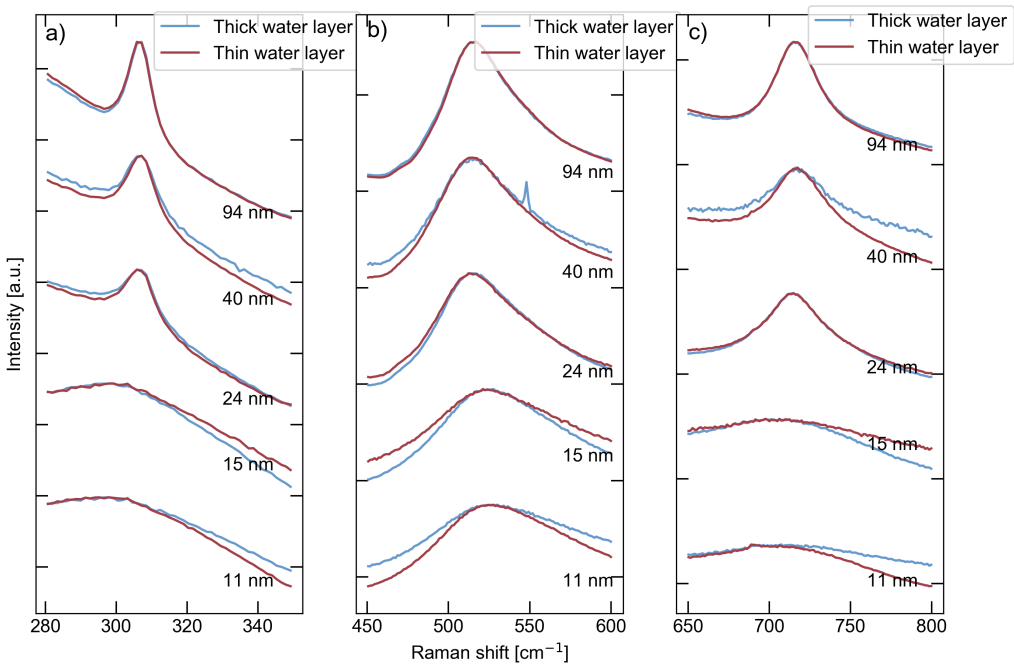

Figure 4.8: Peaks normalized for peak maxima for raman spectra for $BaTiO_3$ nanoparticles with a thin layer of water (purple) and a thick layer of water (blue).

The water samples have a visibly more intense peak, while the oil samples display a flatter feature. This difference is reduced for the 11 nm crystallites, which have a very similar shape for the two dispersion mediums. The oil samples still have smaller internal difference in intensity, as the valley between the peaks around 420 cm^{-1} are deeper for the water dispersed particles and the peak maxima is higher.

The individual peak comparison of the peak at 500cm^{-1}, 700 cm^{-1} and approximately 300 cm^{-1} is shown in figure 4.10. The intensity difference is the difference between the maximas to the baseline, where the spectra is normalized for the peak maxima. The difference between the two mediums is very similar for all three peaks, where the 94 nm and the 40 nm crystallites display a more intense peak for the samples dispersed in water than in oil. The 24 nm particle have a slightly more intense 510 cm^{-1} and 710 cm^{-1} peak for the water dispersed samples, while the 308 cm^{-1} is pretty similar. The same is true for the 300 cm^{-1} peak for the 20 nm and the 15 nm particle, while the 510 and 710 cm^{-1} have a more intense oil dispersed sample. The 11 nm sample display more intense peaks for all the oil samples.

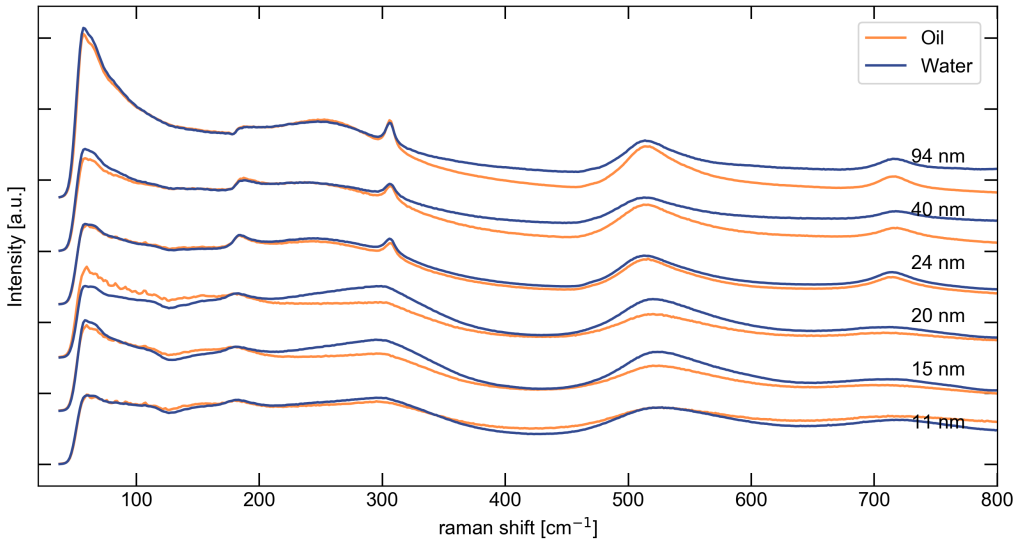

Figure 4.9: Full raman spectra for $BaTiO_3$ nanoparticles with a thin layer of oil (yellow) and water (blue).

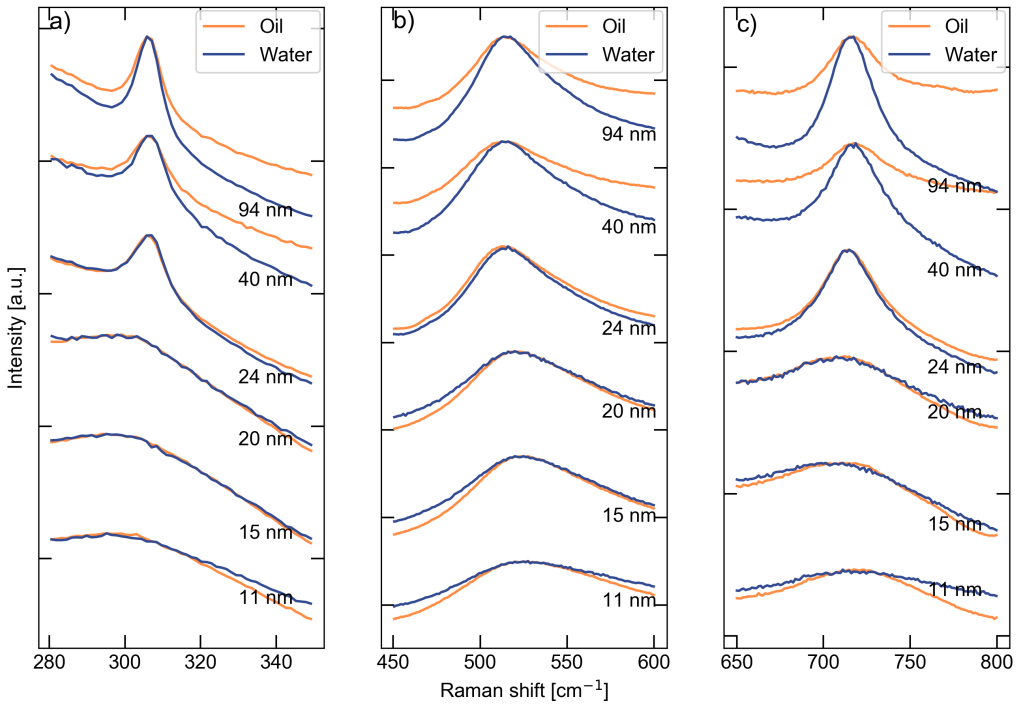

Figure 4.10: Peaks normalized for peak maxima for raman spectra for $BaTiO_3$ nanoparticles dispersed in oil (yellow) and water (blue).

4.4 Local structure

4.4.1 Size dependence of the local structure

The PDF for the dry particles are plotted in figure 4.11, and it is clear that the intensity for the different PDFs scale with the size. The 76 nm crystallites displays clearly defined and narrow peaks, especially for the low r-values, while the 11 nm crystallites have lower intensity and broader peak features, even within the first unit cells. The higher r-values have broader features and slightly reduced intensity for all particles, but the 11 nm crystallites have very undefined and broad peaks above 30 Å, which is earlier than in the larger particles.

The broadening due to size is especially noticeable for the peaks with a "splitting" type shape, where two different atomic distances have similar lengths. Within the the first unit cells this is especially noticeable for the peak at 7 Å, with an increasing shoulder feature with increasing size, and for the peak at 10 Å, where the positions are clearly separated into two peaks for the 94 nm crystallites, but have a shoulder feature for the 11 nm crystallites.

From 30 Å and above there is a clear shift in the peak positions towards a higher r-value for the smaller crystallites. This is a clear display of the ionic expansion, as the subtle difference in the lattice parameter will give a prominent shift in positions at higher r-values.

The 11 nm crystallites have a very low signal above 40 Å, where the peak display a significant broadening combined with a reduced intensity to such a degree that this range will be excluded from further discussion.

The size series for all particles display a very similar size dependent change in the PDF. The exception is the 11 nm crystallites dispersed in oil, which have peaks below 2 Å, which is for distances shorter than the shortest bonds in the crystal. For larger r-values, there is clear periodic noise patterns dominating the atomic positional peaks. The pattern will therefore be excluded from the following analysis, as it is impossible to distinguish the atomic positions from the amplified noise.

4.4.2 Influence from dispersion medium on the local structure

Higher r-range

To allow comparison between peak shape and relative intensity, the particles dispersed in different mediums are normalized for the peak at 8.9 Å. Figure 4.12 shows the 34 nm and the 76 nm crystallite from 40 to 80, where effects such as lattice expansion will give more prominent differences. PDFs for the 76 nm particles are very similar for all dispersion mediums, showing very little structural changes from the different dispersion mediums. Above 70 nm, the PDF for the water dispersed particles are shifted slightly to a higher r-value. This shift is characteristic of the increased lattice parameter, where the ionic expansion shifts the atomic positions to higher distances.

The influence of the dispersion medium is much more prominent for the 34 nm crystallite, especially below 65 Å, after normalization for the peak at 8.9 Å. The particles in water and oil are clearly sifted to higher r-values compared to the dry particles, and

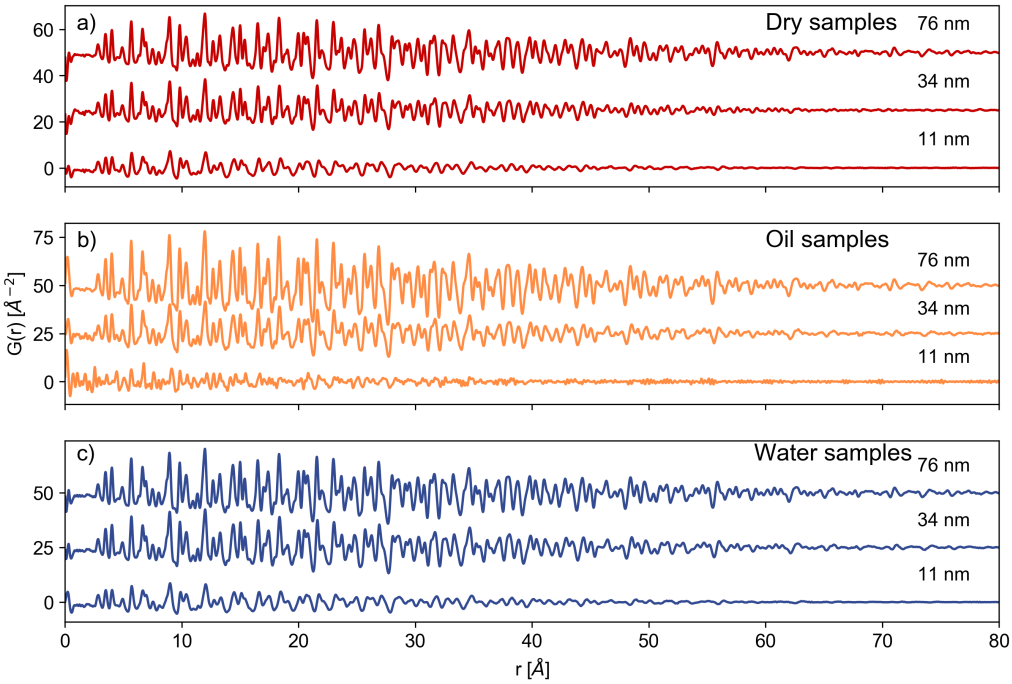

Figure 4.11: PDF of $BaTiO_3$ nanoparticles of 76 nm, 34 nm and 11 nm, displayed for dry particles (red), dispersed in oil (yellow) and water (blue).

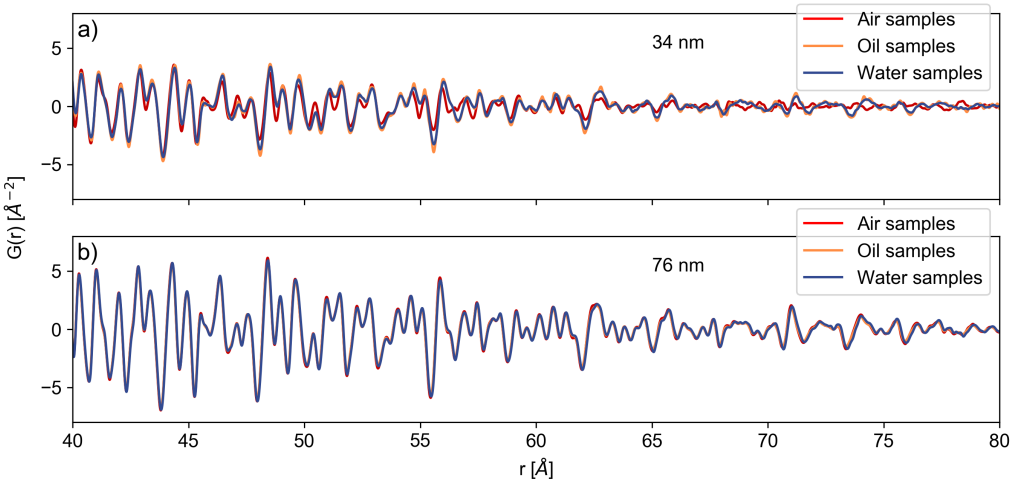

Figure 4.12: PDF of $BaTiO_3$ nanoparticles of 76 nm and 34 nm crystallites, for dry particles (red), dispersed in oil (yellow) and water (blue). The PDFs are normalized for the peak at 4 nm.

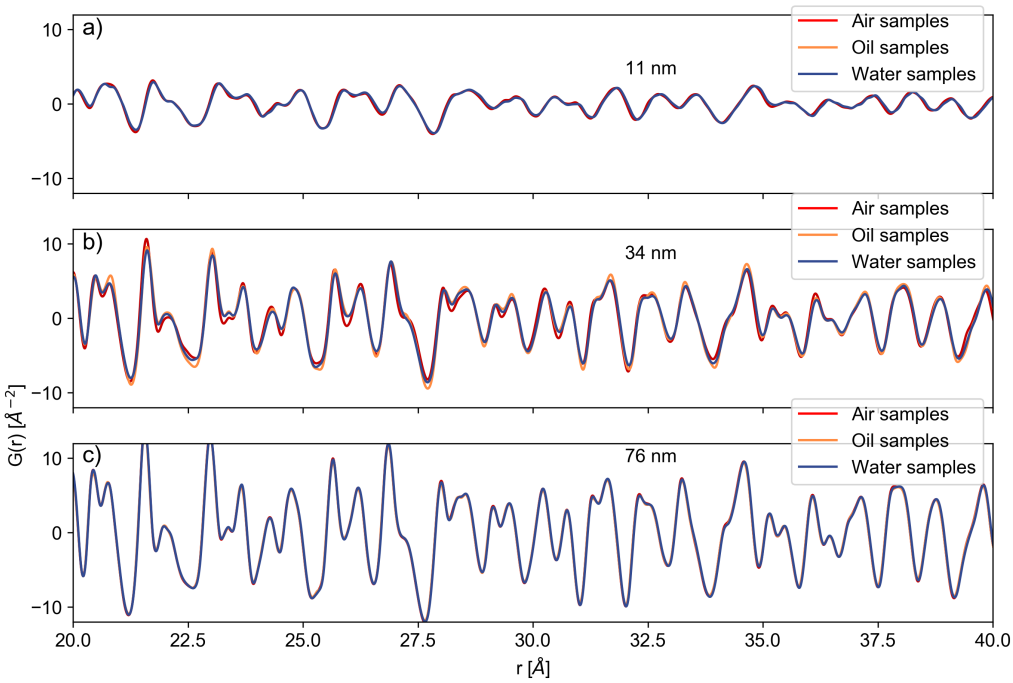

Figure 4.13: PDF of $BaTiO_3$ nanoparticles of 76 nm, 34 nm and 11 nm crystallites, for dry particles (red), dispersed in oil (yellow) and water (blue). The PDFs are normalized for the peak at 8.9 Å

the peak shapes for the three are very different. The splitting type profile is much more prominent for the dry particles, as seen in the peaks at 51 and 55 Å. The relative intensities of the double peaks also shift, as for the double peak at 53 Å, which have an intense peak at 53 Å and a less intense peak at 52.5 Å for the dry particles. In the oil and water dispersed particles, the two peaks are similar in intensity.

The difference between the water and the oil particles are less noticeable, but still prominent. All peaks for the water dispersed particles display a broader feature and a lower maximum, while the oil dispersed samples have a higher maxima for almost all peaks.

A very similar trend is visible in the range between 20 and 40 Å, shown in figure 4.13. For this range, there is absolutely no distinguishable differences between any of the dispersion media for the 76 nm particles. The 34 nm particle have the most prominent difference of the three particle sizes. The water dispersed particles are less intense and the peak shape is slightly broader than the dry or oil dispersed particles. Both these two have sharper peaks than the water samples, but some peaks are most intense for the dry particles, like the peak at 22, 30.5 and 34 Å, while other peaks have a sharper maxima for the oil samples, like the peak at 23, 25.5 and 32 Å. The relative intensities are also different for the oil and the dry samples.

The double peak at 20.5 Å display a clear splitting for the 76 nm crystallite, with a clear difference in intensity between the two peaks. The 34 nm crystallite display the same difference in intensity between the peak maxima for the dry and the water dispersed particles, where the dry particles have a more prominent split between the two peaks. The oil dispersed particles matches the water dispersed particles in the intensity of the lower r-peak and the more shallow dip between the peaks. The higher r-peak is different for the oil and water dispersed particles, with increased intensity for the oil peak, giving two peaks of the same intensity. The interactions between the dispersion mediums and the particles are therefore not straight forward.

The 11 nm crystallites are only compared for the dry and the water dispersed particles, due to the low signal from the oil dispersed particles. The difference between these two samples are less prominent than the same dispersion mediums for the 34 nm particles. The peak at 20.5 displays splitting only for the water dispersed particles, and not the dry particles. The water spectra show a slight shift towards higher r-values, which is the most prominent difference between the two mediums. The double peaks at 25.5 and 30.5 Å have a reduced splitting for the water compared to the dry particles.

Lower r-range

To compare the different samples for the lower r-ranges, the PDF are slightly shifted in the relative y-position. This comparison will be done without any normalization, allowing the intensity to be unchanged.

The 76 nm crystallite have a much higher intensity for the oil dispersed samples than for the dry and water dispersed. There are also some relative differences. The shoulder peak at 6.5 Å is much less intense relative to the corresponding peak at 6 Å for the oil dispersed particles than for both the dry and water dispersed. The same is true for the feature on the side of the peak at 9 Å, where only the oil samples display a reduced intensity for the shoulder.

The dry samples are the least intense, as the baseline of the spectra matches with the water dispersed particles, while the peaks are lower in intensity, something that is true for all particle sizes. The oil samples are the most intense for the 76 nm crystallite, where the peak maxima is higher and the peak minima is lower than the two other particle sizes.

The 34 nm crystallite have a noticeably difference on the shoulder feature at 7 Å for the dispersion mediums. The dry and water dispersed particles are relatively similar, while the oil samples have a reduced intensity for the higher r-value peak.

The 11 nm crystallites also have the 7 Å peak as the most noticeably different, where the water dispersed particles have a higher intensity for the higher r-peak than the dry particles.

4.4.3 PDFs fitted to crystallographic models

The local symmetry of the particle is fitted to both a cubic $Pm\bar{3}m$ and a tetragonal $P4mm$ crystal structure, where the quality of the fit is given in an agreement factor R_w. The largest fit range used is the fits between 20 and 40 Å, and in this range the fit is done for all possible parameters simultaneously. The plotted R_w for all particles in the different dispersion medium is shown in figure 4.15. The difference between the particles is clear,

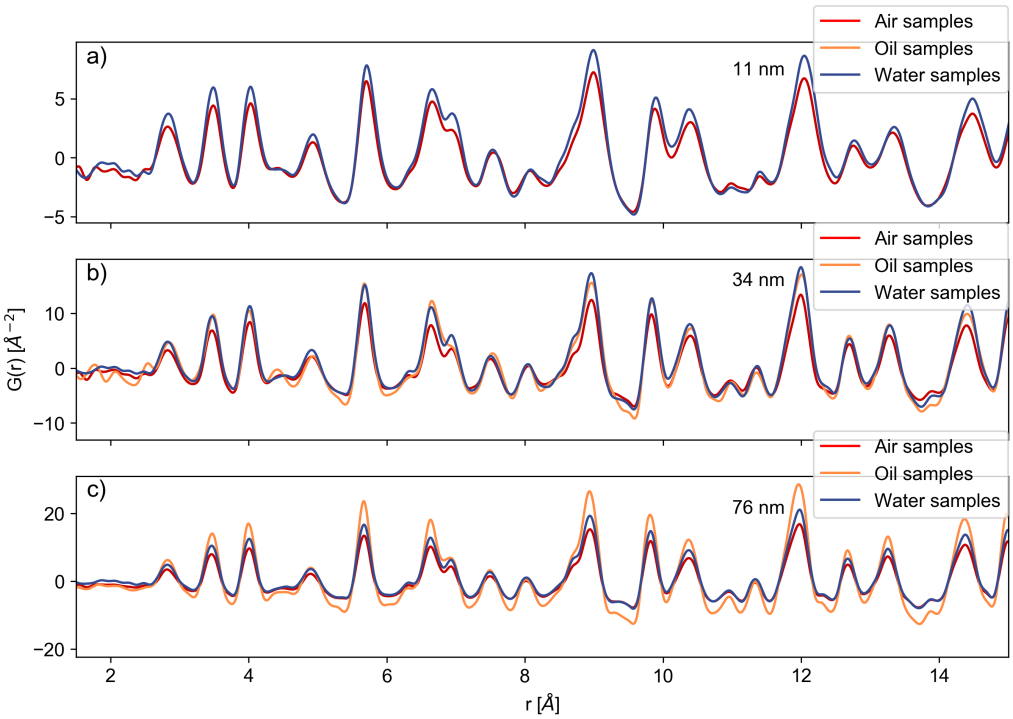

Figure 4.14: PDF analysis of $BaTiO_3$ nanoparticles of 76 nm, 34 nm and 11 nm crystallites, for dry particles (red), dispersed in oil (yellow) and water (blue).

where the large particle have a better fit for all dispersion mediums and for both crystal symmetries. The difference between the fit quality of the 76 and the 34 nm crystallites is not very large, while the 11 nm crystallite have a much higher R_w for all dispersion mediums and crystal symmetries.

The difference between the fit quality of the two crystal symmetries is very clear: The agreement factor for fits using the tetragonal structure is lower for all particles in all three dispersion mediums. The influence from the dispersion mediums is not as obvious, there is not any large differences in the agreement factor. There is however a noticeable influence when the particles of different sizes are compared, there is almost no difference from the dispersion medium for the 76 nm crystallites, while there are clear, but not large, differences for the 34 nm and the 11 nm crystallites.

How the fit agreement factor changes for fits in different ranges will give an indication of how the local structure changes through the crystal. There are only two fit parameters fitted for both the tetragonal and the cubic structure, the lattice parameter a and the ADP. A comparison of the changes in the agreement factor for fits with lattice parameter a is show in in figure 4.16, while the agreement factor for the ADP fits is summarized in appendix C as the trends of the two are very similar. Each plot range is about two unit cells, which is the lowest range where the fit converge.

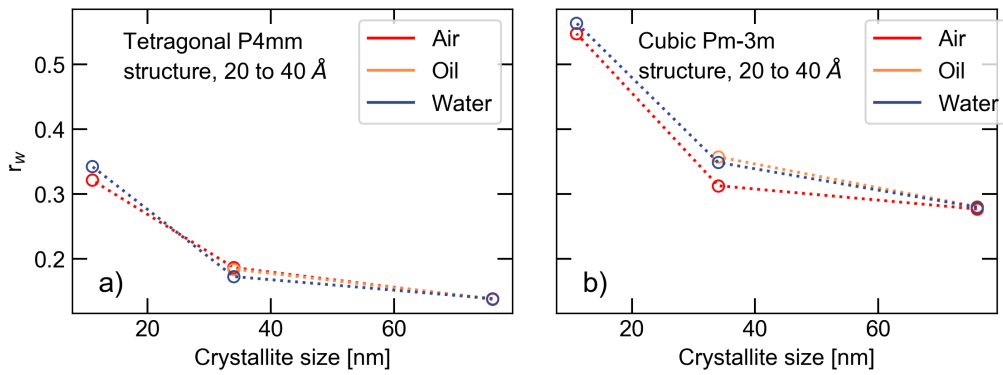

Figure 4.15: R_w value for the fit range 20 to 40 Å. Scaling factor, Q_{damp}, lattice and parameter a is fitted for both crystal symmetries, in addition to lattice parameter c for the tetragonal symmetry.

The first two unit cells gives a fairly poor fit for both symmetries and almost all samples. There is a very clear influence from the dispersion medium on the local symmetry within this range: The 76 nm and the 34 nm crystallites dispersed in water have a much lower value for R_w than the same dry or oil dispersed particles. 11 nm crystallites behave oppositely, the water dispersed particles have the highest R_w of all samples. The agreement factor for the dry and oil dispersed particles are quite similar for the three different crystallite sizes. This is true for both the crystal symmetries, with a slightly higher R_w value for the fits using the cubic crystal symmetry.

For the other two fit ranges, there is a much more obvious influence from crystallite size, and not as distinctive influence from dispersion medium. The 76 nm crystallites have no distinguishable influence on the fit quality from either the crystal symmetry or the dispersion medium. The smaller particles have a distinguishable influence from the crystal symmetry, where the cubic fit becomes much worse with decreasing size with a very large R_w value for the 11 nm crystallites. The tetragonal fit is very similar for the 34 and the 76 nm crystallites, with the 11 nm crystallites slightly higher. The fit quality is slightly different for the different dispersion mediums, but the influence is very small.

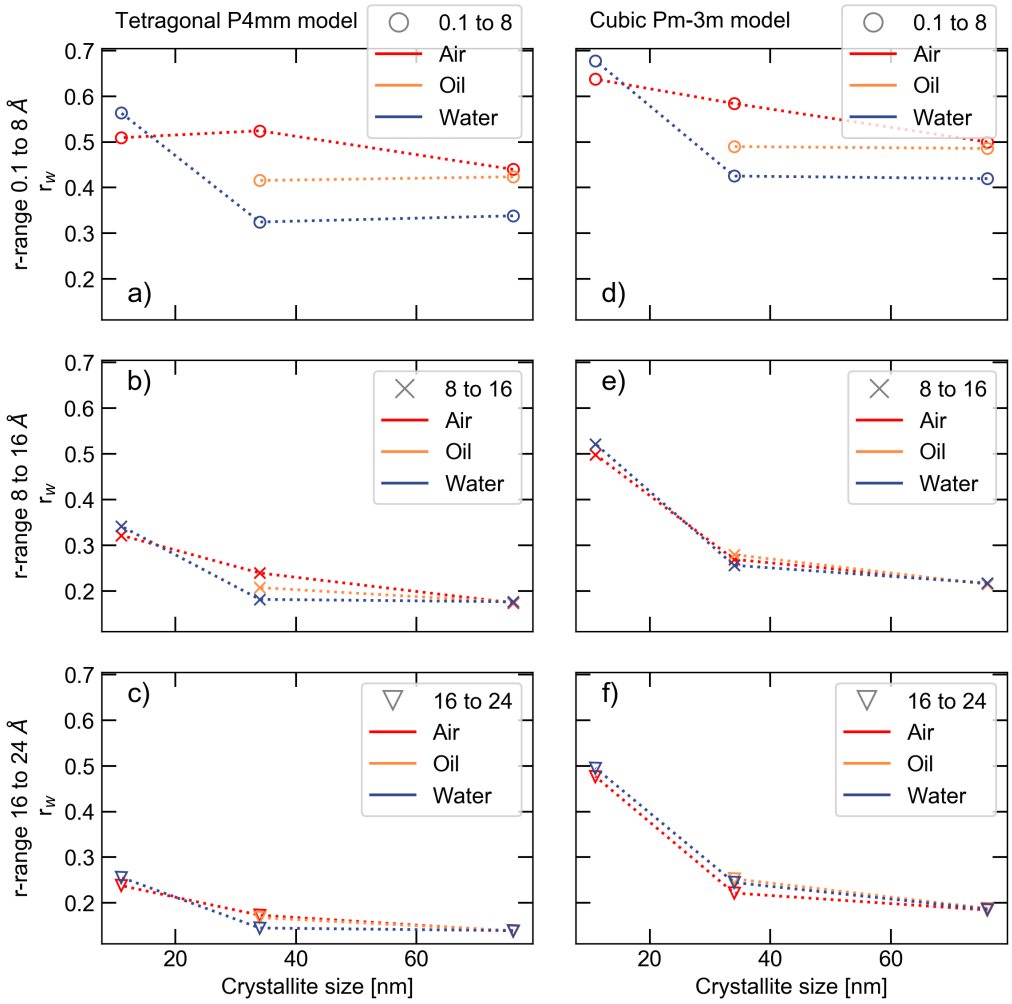

Figure 4.16: R_w value for the fits in the ranges from 0.1 to 8 Å (circle), 8 to 16 Å (cross) and 16 to 24 Å (triangle). The fitted parameter for both particles is the scaling factor, Q_{damp} and the lattice parameter a.

4.4.4 Local structure analysis

A structural analysis is done for the range between 20 and 40 Å, with the results shown in figure 4.17, as this is the highest r-values where the structural data for the 11 nm crystallites are still reliable. At these ranges, shifts due to changes in the lattice parameter is expected to be prominent enough to pronounce the difference between the different dispersion mediums.

The sample with 11 nm crystallites dispersed in oil will be excluded, as the signal from the particles is not intense enough.

The a parameter is very similar for the three different sizes, with a slight increase in the water dispersed 11 nm crystallites as compared to the dry. The dry particles have a smaller c parameter compared to the oil and water dispersed particles, but the difference is larger for the 34 nm crystallites than for the 11 nm crystallites. The water dispersed particles have a very similar c parameter as the oil dispersed particles.

The tetragonality is very similar for 76 nm particles, where the dry particles have the lowest tetragonality, followed by the water dispersed particles and finally, the oil dispersed particles have the largest c/a. The 34 nm crystallites have the same order, but the difference between the different dispersion mediums is larger. The tetragonality of the dry 76 nm and the 34 nm crystallites is almost the same, while both the oil and water dispersed particles have significantly increased tetragonality. The tetragonality of the 11 nm crystallites is much larger than the larger particles, but the difference between the water dispersed and the dry particles is not clear, as the mean value fall within the error of the other sample.

The 76 nm crystallites display no difference in the ADP from the different dispersion mediums. The dry 34 nm crystallites show a decreased ADP value compared to the 76 nm crystallites, while the water and the oil dispersed samples show an increase, with the water dispersed particles showing a steeper increase than the oil dispersed particles. The 11 nm crystallites have the same difference in the ADP as the 34 nm particle for the ADP, shifted to a larger value.

The position of the Ti^{4+} ion is refined only for the z-direction with the Ba^{2+} locked in origo. The 76 nm crystallites show no influence on the Ti^{4+} placement from the dispersion medium. The dry 34 nm crystallites have a similar displacement as the 76 nm crystallites, with a slight increase for the oil dispersed samples and a further increase for the water dispersed sample. The 11 nm crystallites have indistinguishable Ti^{4+} placement, as the errors are large and the points are within the errorbars of the other samples.

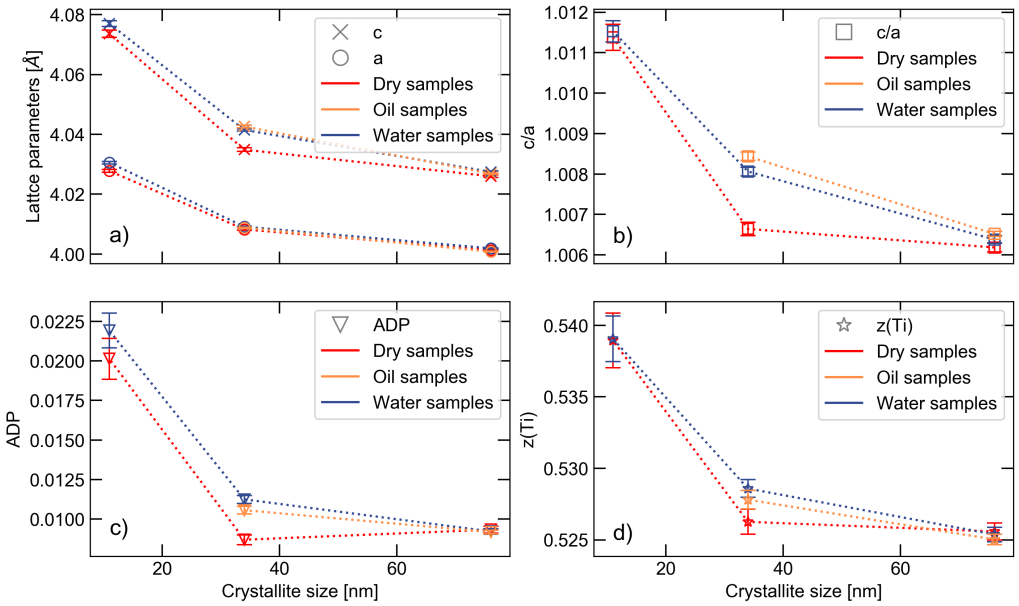

Figure 4.17: Result from fit to the crystal structure $P4mm$ for PDF. (a) lattice parameters, (b) c/a, (c) ADP and (d) z(Ti).

Chapter 5

Discussion

5.1 Agreement between observed structure and crystal symmetry model

The quality of the fit reveals something fundamental about the crystal structure. On the local scale the tetragonal symmetry is clearly a better description than the cubic symmetry. For the 76 and the 34 nm crystallites, the difference between the fits using the cubic and the tetragonal symmetry is clear but not very large. The 11 nm crystallites is not as well fitted as the two larger crystallite sizes, but the cubic fit is exceedingly poor and should not be used as a realistic description of the structure at all.

The reduction of fit quality is, for the lower r-regions, similar to the trends shown by Smith *et. al.*, where the parameters are badly fitted for low r-values, especially in the 0.1 to 8 Å range.[31] The crystal parameters for the 20 to 40 Å range should be used for discussing local crystal parameters.

The high R_w values for the first two unit cells could also be an indication of the local rhomohedral structure described by both Page *et. al.* and Senn *et. al.* for bulk $BaTiO_3$.[22,13] The rhombohedral local structure is not expected to be visible for these particles, as they are characterized by the Ti-O bonds, where the oxygen does not have a high scattering power for the X-rays. The rhombohedral structure could contribute to the bad quality of fit of the structure for the low r-ranges, as there are too the few unit cells to give an average tetragonality.

5.1.1 Dipole order coherence length

Polking *et. al.* demonstrates that there is a clear influence from the surface on the coherence length.[12] The 10 nm spheres have about 10 Å structural coherence, while nanocubes, which exposes low energy crystal planes as surfaces, have at structural coherence for 20 Å for the 8 nm cubes and about 40 Å for the 15 nm cube.[12]

Calculating the coherence length of the particles is not trivial and will involve a range of assumptions, and determination of exact values is impossible. By looking at the spectra it should be possible to identify a range within which the structural coherence is lowered

sufficiently. A loss of structural coherence will give a broadening of the peaks combined with a loss of intensity, as the atomic distribution becomes more drawn out. The coherence length will therefore be at in the range where the amplitude is reduced by some defined fraction of the starting peaks with a definitive peak broadening. This analysis will not give any definite value or certain approximate, as the fraction of amplitude reduction and peak broadening will have to be determined visually, but some estimation of a range in the PDF where the peaks change shape sufficiently can be made.

The 11 nm crystallites is expected to have the shortest coherence length of the three sizes. The particle have a large peak at 12 Å, and after this peak there is no peak with the same amplitude and sharpness. The difference is clear when comparing the spectra before 10 and after 15 Å, where earlier peaks are well defined and sharp, and the peaks after have a definitive reduction in intensity and a broadening. A comparison of the two regions with the mid section removed is shown in figure 5.1a. A coherence length of between 10 and 15 Å is consistent with the values reported for a nanosphere by Polking *et. al.*, with a coherence length of 10 Å for the 10 nm particle.[12]

The larger crystallites does not have a similarly abrupt transition as the 11 nm crystallites. The PDF from the two different sizes is also very similar, making it harder to distinguish a point of disorder. For the 76 nm crystallites, there is a clear difference in the peak shapes in the spectra above about 65 Å and below 60 Å. The peak shape of the low r-region is sharper and more narrow compared to the higher r-values, as shown in figure 5.1c.

For the 34 nm crystallites there is a clear difference between the peaks before 35 Å and after 45 Å. The peak shape before 35 Å is clearly defined with sharp peaks, while after 45 Å there is a clear decrease in the peak intensity and the peak shape is broader, giving a much larger degree of disorder. A comparison of the two regions is shown in figure 5.1b.

Even more noticeable is the clear difference between the dispersion mediums after 45 Å, where the atomic distribution for the dry particles differ visibly from the particles dispersed in oil and water, as shown in figure 5.2. The dry particles have a larger loss of intensity and the peaks have a broader shape than the oil and water dispersed particles, in addition to a larger splitting. This could be because disorder gives a reduced coherence length for the dry particles, but it could also be a different dipole ordering for higher r-values.

5.1.2 Influence from the dispersion medium on ionic lattice expansion

There is a clear influence from the dispersion medium on the particles. The increased ionic expansion for the smallest particles is apparent in both the average and the local structure refinements, shown in figure 5.3. As it is the water dispersed particles that display the largest ionic expansion, it is possible that the water molecules shield the surface charges, and allowing a larger degree of ionic expansion.

The interactions is not as simple to explain when considering the particles with no shielding provided. If the interactions is only electrostatic, the oil dispersed and the dry samples should have a very similar structure, but the lattice parameter calculated

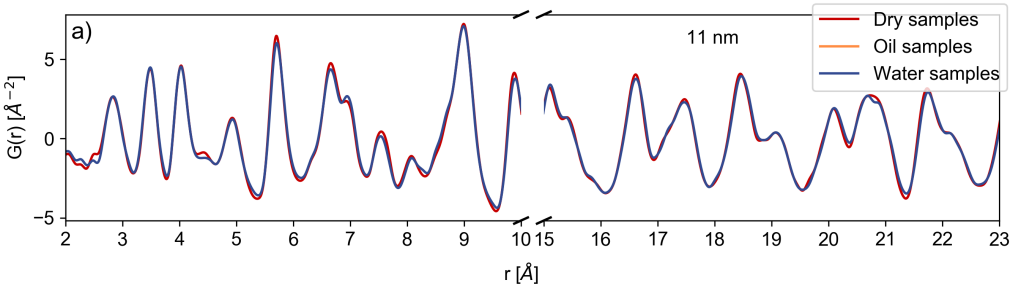

(a) PDF for 11 nm crystallites between 2 and 23 Å, with the range between 10 and 15 Å removed.

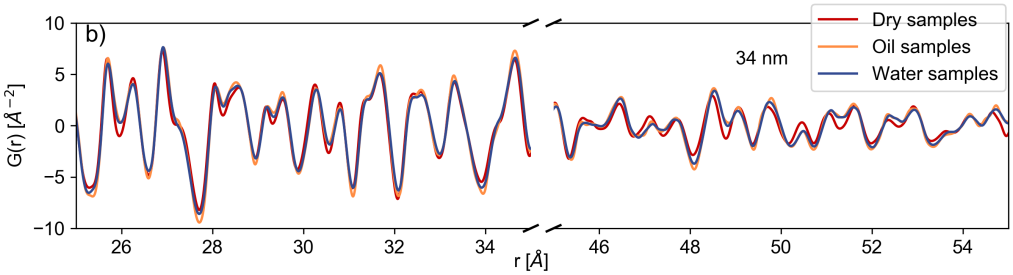

(b) PDF for the 34 nm crystallites between 25 and 55 Å, with the range between 35 and 45 Å removed.

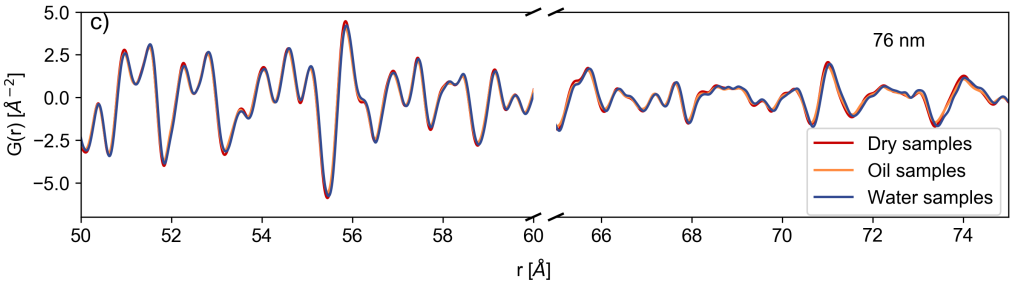

(c) PDF for the 76 nm crystallites between 50 and 75, with the range between 60 and 65 Å removed.

Figure 5.1: PDF of the all particles in all dispersion mediums, with some range removed for better comparison of peak shape and amplitude. The lower r-range display sharp peaks with a high degree of order and the higher r-range have broader peaks due to a lower degree of order.

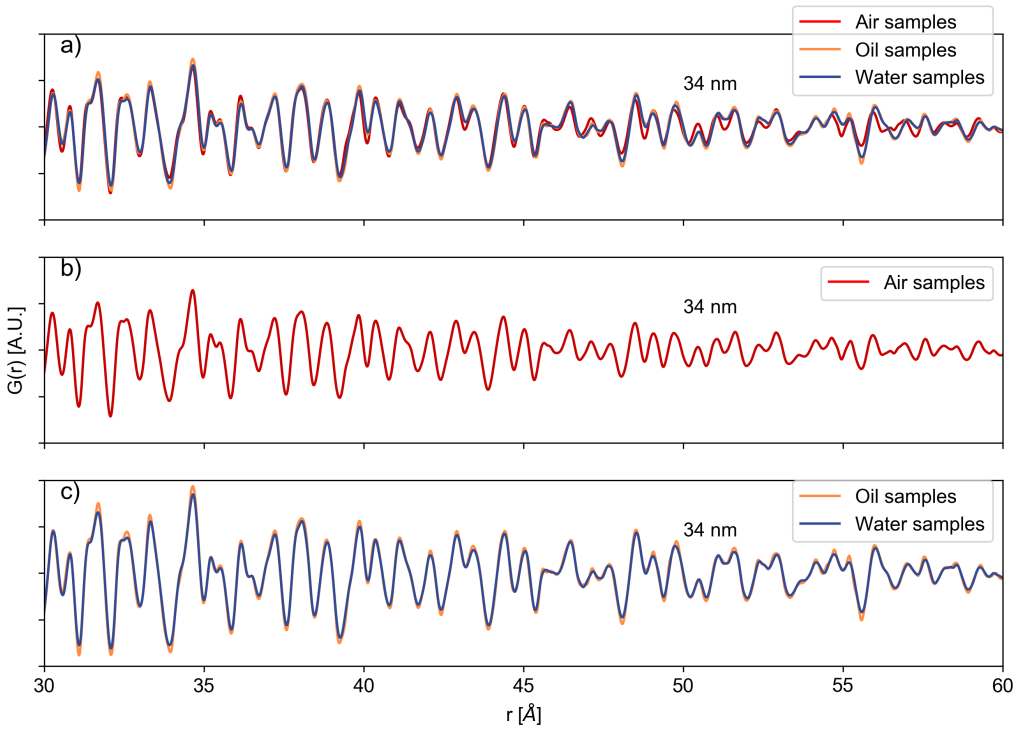

Figure 5.2: PDF of the 34 nm crystallite for (a) all dispersion mediums, (b) only water dispersed particles and (c) oil and water dispersed particles, to reveal the different atomic distribution after 45 Å.

in both the average and the local structure differ noticeable for the different dispersion mediums. One explanation would be the different dielectric constant of oil and air. Air have a dielectric constant of about 1, while the oil used has a value of about 3. The counterargument to this hypothesis is the similarity with the water sample, which have a dielectric constant of on order of magnitude difference. If the difference between the oil dispersed and the dry particles was only electrostatic, it is probable that the effects on the structure should be much less prominent compared to the effects from the water sample. This indicates the presence of other interactions in addition to electrostatic shielding.

The dispersion medium show an influence on the average structure of the particles below 20 nm, with the water dispersed particles display a clear ionic expansion, where both the a and the c parameters is increased significantly. This effect could be an effect of the electrostatic shielding, where the water molecules shield the surface dipoles, reducing surface rearrangement and relaxation, increasing ionic expansion. For the larger crystallites, the signal is dominated by the core of the particle, and the changes on the surface has a very limited influence on the average particle structure. This is consistent with what is known about the behaviour of nanoparticles in general. The fact that the local structure for the 34 nm particles is influenced by the dispersion medium shows this simple

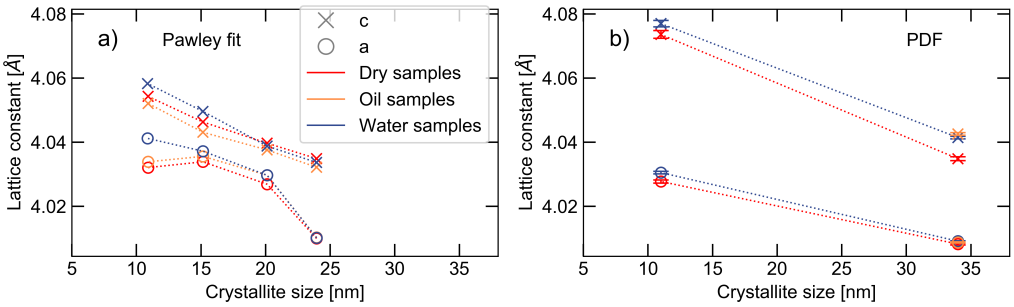

Figure 5.3: Comparison between the local and average lattice parameters a and c for $BaTiO_3$ crystallites under 35 nm.

explanation of the water and the lattice parameter is incomplete, and will be discussed further in section 5.4.

The average structure of the oil dispersed samples does not simply increase with size, necessitating a careful consideration of the anisotropic behaviour of the average structure. The crystal structure is expected to have a larger increase in the a parameter than the c parameter, leading to the expected reduced tetragonality described by Smith *et. al.*.[31] The gradual decrease of the tetragonality with a reduction in size is not reproduced for the average structure of the particles in this project work. This irregular behaviour could be because of limitations in the model, which will be discussed further in section 5.1.3, but there no conclusions about changes in the average structure can be reached from the trend of the tetragonality. This also suggest that the absolute values of the lattice parameters should be considered with caution, but the trend of the lattice parameters could still illuminate something about the structure. The influence of the dispersion medium is not linearly increasing with the dipole moment of the liquid, as was hypothesized, but the changes are anisotropic for the different dispersion mediums. The lattice expansion for the oil dispersed particles have a higher lattice parameter a than the dry particles for crystallites smaller than 20 nm. At the same time, the c parameter is lower. The water dispersed particles have an increase in both lattice parameters compared to the dry particles, showing that the electrostatic shielding alone cannot explain the difference between the interaction between the dispersion medium and the particles. These differences show that there is more to be considered when describing the interaction between the dipoles and the dispersion medium.

This is supported by the fact that the measured influence from the dispersion medium on the local scale is not the same as the measured influence on the average scale. Most importantly, for the local scale the largest difference between the dispersion mediums is for the 34 nm crystallite, while the first visible differences on the average structure is for the 20 nm crystallites. The difference in the average structure increases with a reduction in size, while on the local structure scale the differences decrease for the 11 nm crystallites compared to the 34 nm crystallites. The other large difference is the similarity of the oil and the water dispersed particles on the local scale, where the lattice parameter is calculated to be completely the same locally, while the average lattice parameter is not

only different, but show a difference in size dependent changes.

These differences suggest there are either different interactions between the dispersion mediums or and the particles or a more complex dipole ordering than just stabilized tetragonality versus disordered. Possible candidates for this will be discussed in section 5.3 and in section 5.4.

5.1.3 Limitations of the crystal structure model

Before looking into the possible explanations for the structure parameters, the limitations of the crystal structure model should be considered. The crystal structure can only describe an infinite, defect free crystal at 0 K perfectly. The problem of the thermal vibrations is solved by the fact that the average position of the atom in question is described from the crystal structure.

The defect free crystal will never be true, all crystals will have dislocations, impurities, interstitial or vacant lattice sites. This will make sure that there are always deviations between the crystal and the model, but the differences are usually small enough to be neglected.

A bulk material will have a length that is so much larger than the lattice spacing, so the infinite crystal can be a good approximation. A nanoparticle can have dimensions much closer to the lattice spacing, making the infinite crystal approximation much less accurate.

In addition to the size limitation, there will be reconstruction on the surface of any particle, which will not be described by the crystal symmetry model. For a bulk material, the surface contribution is usually negligible and only give minor deviation from the crystal symmetry. For a nanoparticle, the high surface to volume ratio will have a large influence on the structure, as the rearrangement will strain the crystal significantly. The ability of the crystal symmetry to describe the actual crystal structure might be limited to such a degree that the description is not realistic at all.

5.1.4 Surface structure and the penetration depth of Raman spectroscopy

The particle's structure parameters are not only influenced by the model used, but it is also important to consider the measurement techniques. Before possible interpretations will be discussed, some time should be taken to discuss the length scale and placement of the different measurement techniques.

Both X-ray diffraction and the total scattering is pretty simple to interpret. The XRD interacts with all atomic planes in the structure, which is why the structure calculated will be the average structure. It is similarly simple for the length scales described using the PDF, as it is from the same interaction area as the XRD, and the length scales are explicitly stated.

For Raman spectroscopy the interactions described is a little more complicated. As the measurement uses visible light instead of X-rays, there is a higher possibility of the light not illuminating the whole sample. Raman spectroscopy is thus known to be a surface sensitive technique. There is also the problem with $BaTiO_3$ being a ferroelectric material containing dipoles; there will be interactions between the light and the dipoles, which in

turn will give a much more complicated nature of the refractive index, and possibly limit the penetration depth and therefore the area of the particles that is measured.

Surface sensitivity could also be the source of an important difference between the XRD, PDF and Raman measurements. If the Raman spectroscopy is more surface sensitive, the measured difference in the strain could be because of a difference in the strain throughout the particle. This assumption will be used when discussing the Raman spectra in the further discussion, where the peak broadening is interpreted to be due to increased strain on the surface. This could also explain why the strain differences is not as large in the other measurement techniques. Both the methods using X-ray diffraction measures the whole particle, and would not be sensitive to strain gradients in the particles.

5.1.5 Surface adsorbed species

While examining the limitations of the models, some of the assumptions of the interactions between the particles and the dispersion medium should be commented on as well. The particle is assumed to be completely covered by the dispersion medium without any impurities, and is assumed to not aggregate. This is probably not true, as the particles are small and no surface modification is done to prevent aggregation, because changes in the surface energy will influence the interactions between particle and dispersion medium and might come to dominate the interactions. The influence of possible surface adsorbed molecules is not included in the hypothesis. This might be inaccurate, as only the particles in air will get surface adsorbed water and CO_2 molecules, and there is at least a possibility that these particles have a higher concentration. The dry particles might therefore have some polar shielding or a larger degree of surface rearrangement to accommodate chemisorption, and this might influence the results from the dry particles.

5.1.6 Difference in crystallite and particle size

The following discussion will also be limited by the lack of knowledge about actual particle size. The crystallite size is used to describe the particles, assuming that the particles are singe crystalline. But there is no way of knowing if the particles are actually single crystalline and that particle and crystallite size is the same. This is especially important as the particles does not have the same thermal history, and there is a chance that annealing can create polycrystalline particles. This means that the particles could both have different sizes and larger differences between the particles. The following discussion will assume the particles are single crystalline and the particle and crystallite size is the same, but will still state sizes as the crystallite sizes.

5.2 Size dependent changes in the dipole ordering

The average strain and the Raman spectroscopy data both display an abrupt change in the size series. The cubic symmetry model is the only of the two fits including the strain, and the results of the Pawley fits for crystallites below 20 nm reveal no strain for both the water and the oil dispersed particles. This situation is highly unrealistic, as nanoparticles are known to have a high surface to volume ratio and surface rearrangement will effect

a large portion of particles in the system, giving a high degree of strain. The fact that these particles are fitted to have no strain suggest that the symmetry is unable to describe the realistic structure, which was discussed in section 5.1.3. At the same size where the model is unable to fit the strain, there is also an abrupt change in the Raman spectra. Both Shiratori *et. al.* and Smith *et. al.* uses the peak at 306 cm^{-1} as the signature of tetragonality,[47,31] and the former comments that the disappearance of the peak for the 12 nm particle in their study makes it impossible to determine that the structure is tetragonal. The disappearance of this peak is interpreted as a sign of the particle becoming a mixture of the cubic and possibly the tetragonal crystal structure. Shiratori *et. al.* shows that for a particle of 33 nm, the 306 cm^{-1} peak is distinct, while the 22 nm particle has a slight shoulder feature on the broader 250 peak.[47] The next particle at 12 nm has no distinguishable peak for this size. The size limit is in agreement with the results in this work, where the 24 nm crystallite displays a clear and distinguishable peak at 308 cm^{-1}, while the 20 nm crystallite only have the broader 295 cm^{-1} peak. The change in crystal structure that is represented by this peak disappearance is quite abrupt, going from a clearly tetragonal to losing the feature within the span of 4 nm.

To understand the nature of this change, the nature of the Raman peaks should be considered carefully. It is important to keep in mind that the structure is a result of rhombohedral unit cells that give an average tetragonal structure over slightly longer r-ranges, which is shown by previous studies and the latter is confirmed by the the local structure analysis in this project work. However, the fitted average structure of the crystallites below 20 nm is similarly good for both the cubic and the tetragonal symmetries.

None of the articles discuss the structural changes behind the mixed nature of the 300 cm^{-1} peak, so the forward discussion and interpretation should be applied with caution. The peak at approximately 300 cm^{-1} is a mix of the 250 cm^{-1} and the 308 cm^{-1} peaks.[47] These peaks are the result of very different structural components: the 308 cm^{-1} is the wing flapping mode of the tetragonal structure, while the broad peak at 250 is related to the disorder in Ti^{+4} and as shown by Smith *et. al.* it is present above the T_c.[31] The fact that $BaTiO_3$ is present above T_C hints toward some local displacement even at this temperature, as the centrosymmetric symmetry is Raman inactive. This is consistent with the phase transitions described by Senn *et. al.*, where the changes in structure is on the average scale and the Ti^{+4} displacement will always be rhombohedral on the local scale. The relationship of the local rhombohedral structure to the tetragonal peak at 308 cm^{-1} is never explained, but it is reasonable to assume that as the phonons is a collective phenomena, it describes a row of diploles with an average tetragonal structure. The merge of the two peaks might suggest that the low range average tetragonal chain is broken or the coherence length is reduced significantly.

The same size that displays a change in the size series of the Raman spectra, display a change in the interaction with the dispersion medium. The larger particles have more intense Raman peaks for the water dispersed particles while the smaller particles have more intense Raman peaks for the water dispersed particles. The explanation of this broadening could be that there is either a change in the degree of strain or structural coherence within the particles, as mentioned by Smith *et. al.*[31] The large oil dispersed particles might therefore have a larger degree of strain or a reduced structural coherence,

while it is the water dispersed particles that display increased strain or reduced structural coherence below 20 nm. The strain difference is not confirmed by the average structure measurements, but as previously discussed the model is clearly unable to model the system properly. The coherence length difference between the dispersion mediums cannot be confirmed by the discussion in section 5.1.1, but as no conclusions could be reached, a possible influence of the dispersion mediums on the coherence length cannot be ruled out. The difference in the results could be explained by the discussion in section 5.1.4, where it is mentioned that the penetration depth of Raman spectroscopy could be quite low compared to the particle size, even for the smaller particles. The method should at least be assumed to be surface sensitive, meaning that the changes in the Raman spectra could be interpreted as changes in the ordering of the dipoles at the surface.

The fact that the size range where this change happens is such a small one is a reason to consider the underlying changes in the dipole ordering carefully. This is even more significant as the measurement by Shiratori *et. al.* also show the same change and places it within the same narrow size region.[47] The region is also highlighted for the by the results from the Pawley refinement for the average structure, where the model is unable to describe the strain in the system. All of this suggest that there is a real change in the structure of the particles between the size range of 24 nm and above and 20 nm and below. The structural changes is not a severe degree of disorder with loss of local coherency, as the PDF does not show the smeared out peaks as Polking *et. al.* shows for the melting Bi sublattice in $BiFeO_3$.[43] It is therefore probable that there is a change in the ordering of the dipoles, that the crystal symmetry models are unable to describe.

Two different dipole orderings are proposed, which is an ordering of a domain structure as proposed by Schilling *et. al.* and the vortex states, as described by Naumov and Fu.[33,35] It should be emphasized that these results cannot prove the existence of either dipole order, and the discussion will therefore not be able to draw any conclusions about the dipole ordering.

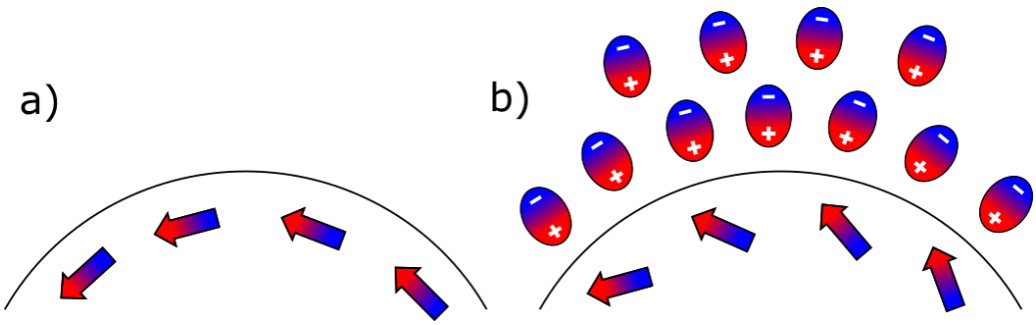

Figure 5.4: Simplified illustration of shielding from water on vortex states, with (a) a particle with no shielding and (b) a particle with shielding. The dipoles are average dipole moment at a longer length scale. Figure inspired by Naumov and Fu.[35]

5.3 Vortex states

The polarity of the water samples is thought to stabilize out of plane polarization, which is hypothesized to stabilize the ferroelectric ordering. The weakness of this hypothesis is that more complex ordering states is completely excluded, and the particles are thought to be in a linear spectrum between an average ordered, tetragonal state and a disorder in the dipole direction giving a average symmetry of cubic symmetry. This ordered, tetragonal state would be the type of dipole ordering observed by Polking *et. al.* for a particle between 8 and 15 nm.[12] If the particles in this study have this configuration, they should display the expected tetragonality on the average scale, as well as a stabilization of the dipoles along the surface in the polar liquid, which is expected to result in a higher tetragonality on the local scale as well, which is not what is observed. Shielding is however not the only way the particle can minimize the energy related to the unshielded charges.

The particles with 20 nm crystallite size or smaller are characterized by some significant structural features. The Raman spectra show a change related to the structure at the surface, which could either be a higher degree of stress or a lower coherence length in the dipole ordering. The same particles display a large influence on the average structure from the dispersion medium, where the water particle induce a larger ionic expansion, while the oil particles have an anisotropic change in the lattice parameters. The difference in the local structural parameters are notably similar internal difference between the 34 nm crystallites in different disperison mediums.

Naumov and Fu suggest that the vortex states occur as a way to reduce lattice strain, which is assumed to be large for nanosized particles.[35] The article describes a coexistence of both a polarization and a vortex state, which is what these results will be compared to. There are two directions that should be considered separately, the z-direction which is the direction of the polarization domain and the toroid moment of the vortex state and the xy-plane where the vortex state orders the local dipoles, as the surface charges are oriented differently at the surface and will interact differently for the dispersion mediums.

The interactions on the surface for the xy-plane will be considered first, with a simplified illustration shown in figure 5.4. The particle aligns all dipoles parallel to the surface, and therefore follows the curvature along the particle. The oil will have no interactions with the dipoles, leaving the particle in a configuration with reduced strain. The electrostatic interactions between the water and the particles might lower the energy configuration of the dipoles pointing perpendicular to the surface and stabilizing this state. The system now have two energy configurations close together, giving both dipole orientations similar energy cost. This might disrupt the vortex state, or just create more strain for the dipoles on the surface which will have a lower difference between the energy of the two states. This might be a possible explanation of the Raman results of the two particles, as it might increase the surface strain or reduce the coherence length at the surface.

There is a different interaction possible along the z-direction, which is shown in figure 5.5. As explained by Naumov and Fu, the centre of the particle will be highly strained, creating the possibility of a nucleated polarization in the particle centre.[35] The nucleation demonstrated is the result of an applied electric field, which is not present for these particles. If the strain in the particle centre is high, there is the possibility that a do-

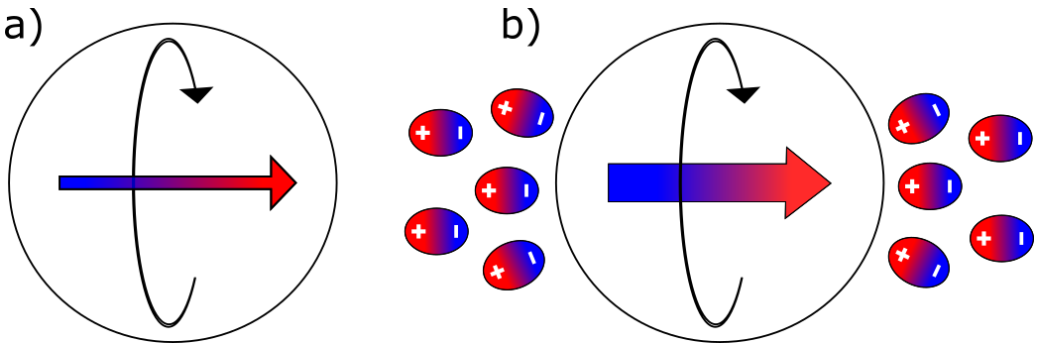

Figure 5.5: Illustration of simplified possible effect on shielding from water on a polarization domain in a vortex state. (a) Particle with no shielding of surface dipoles, (b) Particle with shielding. The dipoles are average dipole moment at a longer length scale. Figure inspired by Naumov and Fu.[35]

main with large linear polarization is stabilized in the middle of the vortex state. The stabilization of the surface charges provided by the water molecules could stabilize the polarization, increasing the average and local ionic expansion but giving a large degree of surface strain or reduced coherence length on the surface, as the explanation of the polarization direction does not contradict the interactions in the xy-plane.

The particles described by Naumov and Fu is cylindrical, so any dipole on the surface is either exposed in the xy-plane or in the z-direction. There is no reason for expecting these particles to be as ordered, they are expected to be more spherical, leaving many dipoles with a much more strained and complicated interaction with the surface.

The domain pattern described by Schilling *et. al.* should also be considered for this size range.[33] The crystallite size makes the domain structure improbable, as each domain would be very narrow, creating several domain walls, and the atoms at a domain wall have a higher amount of stress than the atoms within the domain. The domain pattern is also not able to explain the increased surface stress for water dispersed particles compared to the oil dispersed particles, as the areas with dipoles perpendicular to the surface would be shielded by the water molecules. If the broadening is due to a reduced coherence length, it would make the domains more narrow, which in turn gives more internal strain.

5.4 Polar domains

The particles with 24 nm crystallite size and above are characterized by almost no influence on the average lattice parameters from the different dispersion medium. The average fits for both strain and tetragonality is different depending on the dispersion medium, but as discussed previously, these results should be excluded from the further analysis. On the local structure, the 34 nm crystallites are the ones showing the largest changes in crystal structures from the different dispersion mediums. The 76 and 94 nm crystallites shows no difference as a result of the dispersion medium, so it could be that these particles have a different dipole ordering structure than the 34 nm crystallites. As the dispersion medium

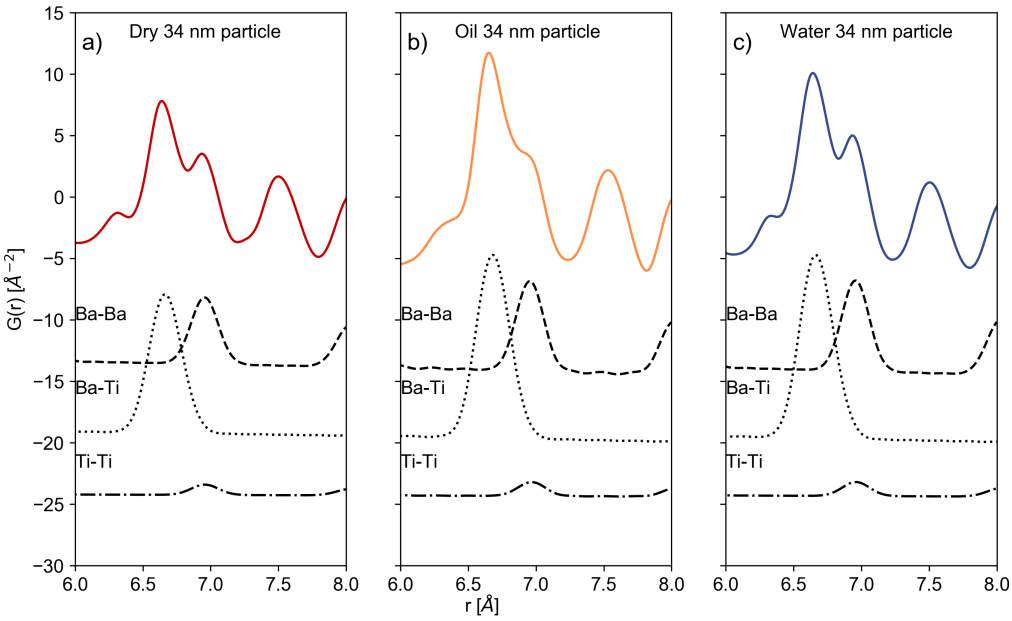

Figure 5.6: PDF for 6 and 8 Å for 34 nm $BaTiO_3$ particles, displayed for dry particles (red), dispersed in oil (yellow) and water (blue). The contributions from the different bond types is displayed by the broken lines.

influence is the most notable feature of the 34 nm crystallites, and the 76 nm crystallites is unchanging for both local and average structure, the different dipole ordering is not impossible and would maybe not be detected in these results. The reduced influence is more likely to be due to size effects, where the 76 and 94 nm crystallites are heavily dominated by the inter-particle atoms and the surface effects are negligible, which is consistent with known nanoparticle behaviour. There is also not any feature to suggest a change in the dipole ordering, as there is in the Raman spectra between 20 and 24 nm crystallites. It is safer to assume that the dipole ordering is the same for the 34 nm and larger crystallites, but only the 34 nm crystallites show an influence from the dispersion medium due to size effects. This crystallite size will therefore be the centre of the further discussion.

To discuss the influence of the dispersion medium on the particles, the PDF is split into the contributions from the different bond types and significant peaks will be discussed in depth. Only the metal-metal bonds will be discussed, as the oxygen have a very weak scattering ability, giving a weak signal and limited influence on the spectra. All particles are shown without normalization, but the discussion will focus on the relative intensity within the spectra in question.

The double peak at between 6.5 and 7 Å is plotted in figure 5.6. The peak shape is very similar for the dry and water dispersed particles, but the water dispersed particles are more intense than the dry particles. The oil dispersed particles have a distinctly different shape, giving the peak a shoulder feature instead of the splitting feature displayed by the

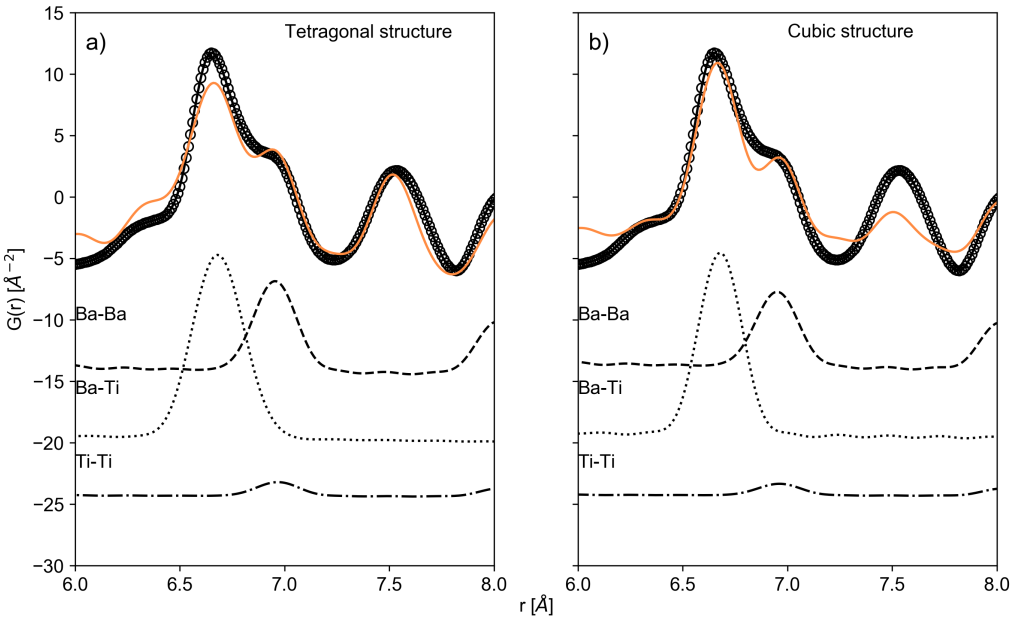

Figure 5.7: PDF for 6 and 8 Å for 34 nm $BaTiO_3$ particles, fitted to both tetragonal and cubic crystal symmetry. The contributions from the different bond types is displayed by the broken lines.

dry and water dispersed particles. The peak at 6.5 Å is due to Ba-Ti distances within the second unit cell. There is not a very large difference in the broadening of the three particle types, which could be expected to broaden for a large disorder in the placement of the Ti^{4+} ion. The differences between the oil dispersed particles compared to the dry and water dispersed particles could be due to a difference in dipole order.

The peak is discussed in depth by Petkov *et. al.*, as it gives important information about the dipole ordering.[42] The calculated PDF for a cubic symmetry gives a reduced peak intensity for the shoulder peak compared to the calculated tetragonal shoulder peak. The shoulder shapes shown by Petkov *et. al.* is less pronounced than the shoulder shapes shown in this project, and it becomes even more pronounced with a reduction in size. The difference between the cubic and the tetragonal fit is shown for the oil dispersed 34 nm crystallite in figure 5.7. The lower peak at lower r-values is better described by the cubic structure, and according to the interpretation from Petkov this hints that the change in shape for the oil dispersed particle is in fact a sign of a more cubic structure on the local scale. This interpretation should be applied with caution, as the other peaks in the range between the 6 and 8 Å is much better described by the tetragonal symmetry, showing that the local structure is not described well by either. This fits well with the assertion by Page *et. al.* and Senn *et. al.* of the local rhombohedral structure, as two unit cells cannot give an average tetragonal structure.[13,22]

The peak at 21 Å display a similar feature as the 7 Å peak, which is plotted in figure

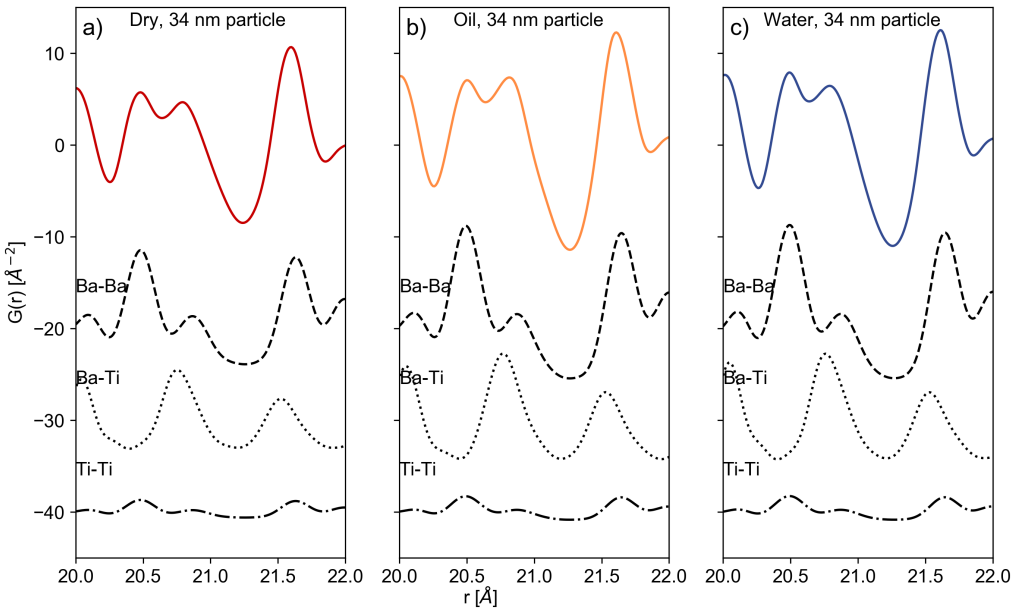

Figure 5.8: PDF for 20 and 22 Å for 34 nm $BaTiO_3$ particles, displayed for dry particles (red), dispersed in oil (yellow) and water (blue). The contributions from the different bond types is displayed by the broken lines.

5.8. The splitting for the dry and the water dispersed particles is very similar, with a distinctively higher intensity for the peak maxima compared to the baseline for the water dispersed particles. The splitting feature is due to one Ba-Ba bond which is the same intensity for all three dispersion mediums, and a Ba-Ti bond which gives a more intense peak for the oil dispersed particles. This could suggest a higher degree of order in the Ti-sublattice for the oil dispersed particles.

The peak at 26 Å, shown in figure 5.9, is very similar for the oil and water dispersed particles, while the dry particles have a more distinct splitting. This is due to a relative shift between the Ba-Ba distance and the Ba-Ti distance for the dry particles. From this size and onward there is a shift from the oil dispersed particles showing a different local structure, to the dry particles being the different one. The nature of this difference is very obvious in the region between 45 and 65 Å, shown in figure 5.10. The Ba-Ti peaks is much broader for the dry particles, suggesting a very low degree of order. Both the oil and the water dispersed particles have distinguishable Ba-Ti peaks up to 65 Å, while the dry particles have a very low degree of order already at 45 Å. This could suggest that the dry particles have a reduced coherence length.

This gives two important features of the local structure of the 34 nm crystallites. For low r-values the oil dispersed particles diverge from the local structure of the dry and water dispersed particles. For higher r-values the dry particles show a larger degree of disorder, something which is mirrored in the structure parameters, where the dry particles

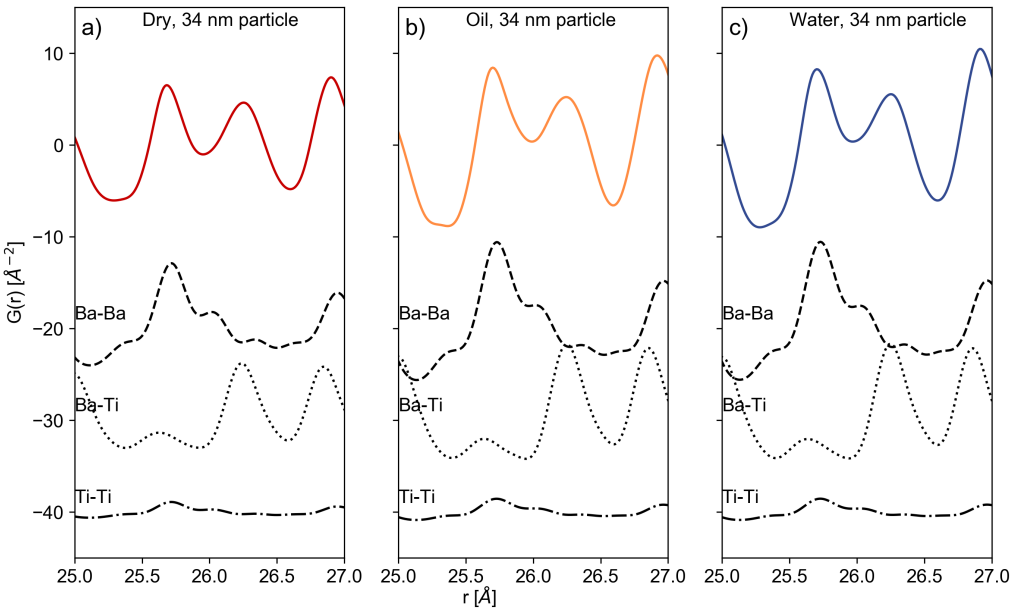

Figure 5.9: PDF for 25 and 27 Å for 34 nm $BaTiO_3$ particles, displayed for dry particles (red), dispersed in oil (yellow) and water (blue). The contributions from the different bond types is displayed by the broken lines.

have the lowest lattice parameters, tetragonality, ADP and Ti^{4+} displacement. It should be stressed that the structure parameters is fitted to the region 20 to 40 Å, where the dry particles start to show a large difference from the other particles. There is no reason to believe that the difference from the structural parameters is the same for all r-ranges.

The vortex states should be investigated as a possible candidate. One important detail is that the particle sizes described by Petkov *et. al.* is an order of magnitude smaller than the smallest in this range, and should not be determined to be stable at the lower size. The Raman spectra of the larger particles have much broader peaks, and therefore strain, for the oil dispersed particles compared to the water dispersed particles, showing a different interaction between dispersion medium and the particles compared to the particles with crystallite size below 20 nm, where the peak shape and therefore strain is larger in the water dispersed particles. As discussed in section 5.3, this is not how the dipole ordering is expected to interact with the dispersion medium in a vortex state.

The Raman spectra is consistent with what is expected for the simpler dipole ordering, where the water dispersed particles having a low degree of surface stress or a higher coherence length at the surface due to electrostatic shielding of the surface charges. The PDF show the oil dispersed particles having a different dipole ordering for low r-ranges, and the dry particles a lower degree of order for higher r-values.

Another possible ordering structure is the stripe domain configuration described by Schilling *et. al.* for 100 nm particles.[33] A domain structure could have local differences

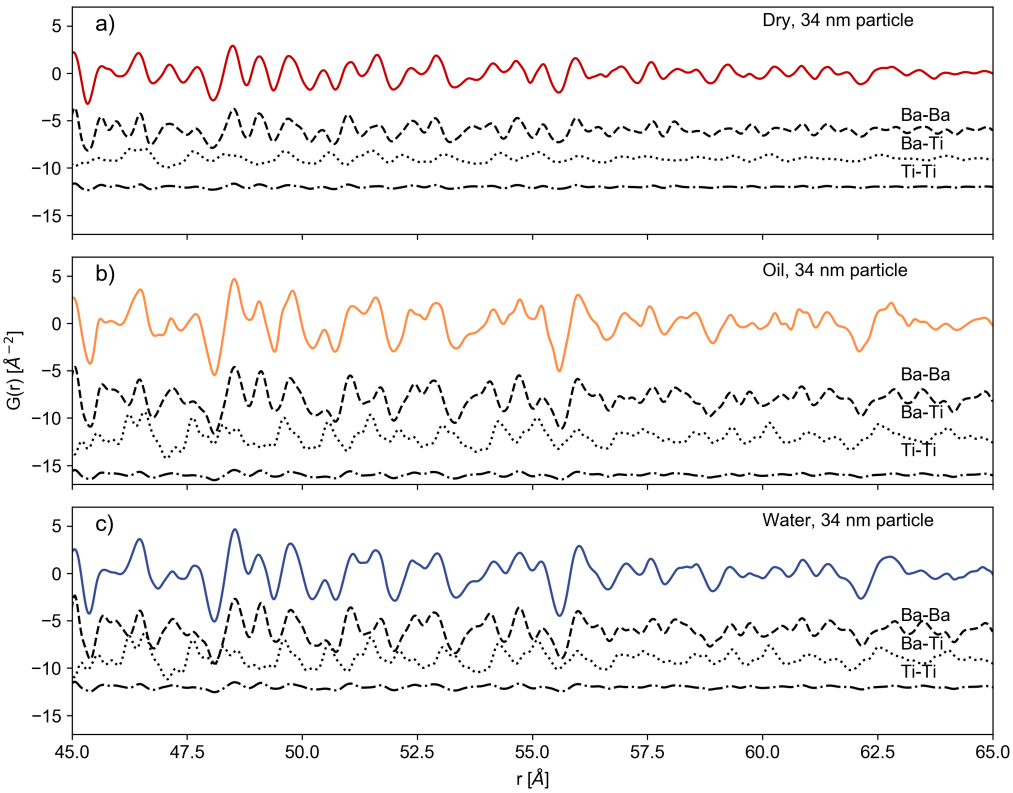

Figure 5.10: PDF for 45 and 65 Å for 34 nm $BaTiO_3$ particles, with dry (red), dispersed in oil (yellow) and water (blue).

with little change in the average structure, as the average structure will be an average of all domains. A change in the width of the domains would change the structure locally, as illustrated in figure 5.11.

The difference between degree of disorder for the dry particles versus dispersed particles at higher r-ranges could be explained by a reduction in the width of the domains. Fong *et. al.* explains the stripe domain with alternating polarization as a method for neutralizing the depolarization field, where the width reduces with an increasing depolarization field.[10] It could be that by reducing the line width of the domains, the particles reduce a stronger depolarization field, which could explain the difference between the water dispersed particles and the dry particles.

The oil dispersed particles are not as easily explained by the stripe domain, as the particles are different only within the first few unit cells, before reverting to a very similar structure as the water dispersed samples for higher r-ranges. The particle morphology and the orientation of the domains has been excluded from the discussion, but as the calculation from Schilling *et. al.* show, both have a large influence on the domain structure.[33] As neither of these are known, it is impossible to determine this as the reason

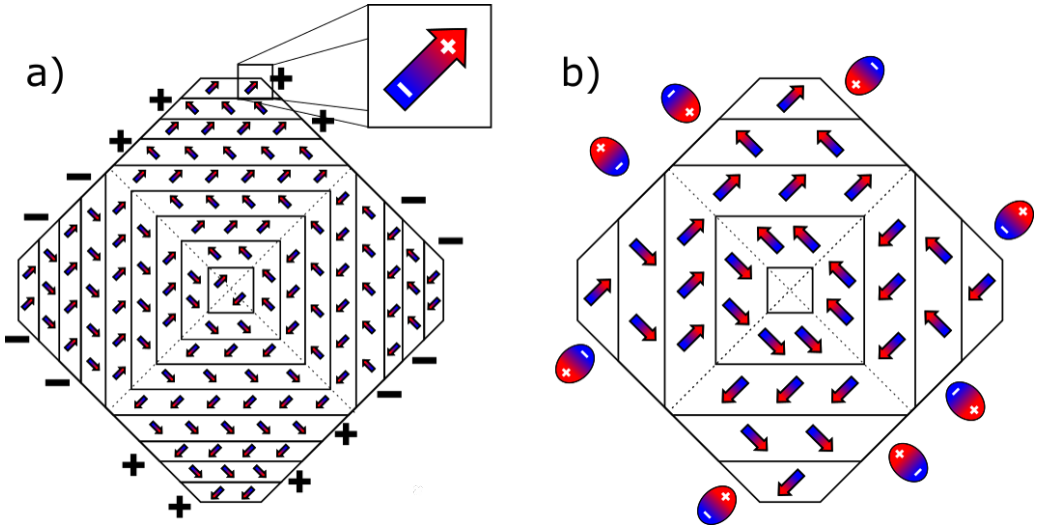

Figure 5.11: Possible domain structure for (a) dry and (b) water dispersed particles, with the domain wall length increased by water molecules providing shielding for the dipoles.

for the difference in the dipole ordering difference for low r-range, but it is a possible explanation as domains along different crystallographic axis might give a very different local structure within the first few unit cells.

There is a variety of different stripe domain structures both theorized and observed, as discussed by Gregg, which gives reason to believe that if the larger particles does have a domain structure, these could be much more complicated than the relatively simple domains described by Schilling *et. al.*[37,33]

5.5 Further work

This study has shown that the crystallographic models based on the symmetries of the space groups is unable to explain the dipole ordering in $BaTiO_3$ nanoparticles. Further work is necessary for determining both the ordering structure of the dipoles and to determine the influence of the shielding on the depolarization field.

The measurements used in this study should be repeated for a material with a better shielding ability. A liquid metal with a better wetting ability than eutectic gallium-indium is the preferable option, but molding the particles into a solid solution of an ionic salt with a very low eutectic point could be a simpler option. The salt mixture is melted around the particles, giving a disc with the particles at the bottom, as most salts will be much lighter than $BaTiO_3$ which can then be measured by normal X-ray diffraction. This should provide a better shielding for the particles than the liquid water, and could provide a better understanding of the nature of the shielding.

The particle morphology is expected to influence the dipole ordering heavily. Controlling the particle morphology will require a better knowledge of hydrothermal synthesis or

using high precision methods like FIB milling, which makes this a much more complicated procedure than within the scope of a master thesis. Repeating the experiments within a single size, while for particles that are either spherical, rod or disc shaped or cubic with different crystallographic phases exposed could give a better understanding of the influence from the dispersion medium.

As no final conclusions about the presence of the more novel dipole ordering can be drawn from the present work, further work should include imaging that can identify this ordering. As there is more articles published that observe vortex states and domain structures directly, the techniques of imaging domains or vortexes could become more common. TEM imaging in a liquid is challenging, but would give new insight on the dipole ordering and therefore on the stability of ferroelectricity at the nanoscale. The size range between 20 and 24 nm is especially important for further characterization as this size range display an abrupt change in the Raman spectra, which is in this work interpreted as a change in the dipole ordering and used to hypothesize two different phases of dipole ordering.

Chapter 6

Conclusion

$BaTiO_3$ nanoparticles was prepared using hydrothermal synthesis, giving crystallites between 11 and 31 nm, and an additional annealing gave crystallites in the range of about 40 nm to 94 nm. The particles was then dispersed in mediums with different dielectric constants and the structural parameters were characterized by Raman spectroscopy, X-ray diffraction and synchotron total scattering X-ray diffraction.

The results show clear deviations from the expected results of the influence of the dispersion medium, and can not be explained as a single crystal with a simple tetragonal $P4mm$ or cubic $Pm\bar{3}m$ symmetry, even taking into account the expected nanoparticle strain and disorder. The influence of dispersion medium on the local structure is different from the average structure, which, coupled with the abrupt change in the Raman spectra between 20 and 24 nm, suggest a change in dipole ordering, interpreted to be a transition between two phases. The two particle regions are characterized by different traits. For 24 nm crystallites and larger, there is a lower surface strain for the water compared to the oil dispersed crystallites, and no influence from the dispersion medium on the average structure. The dispersion medium have a large influence on local structure, with the dry particles exhibiting reduced coherence length and oil dispersed particles displaying dipole ordering with a more cubic symmetry within the first few unit cells. This is interpreted as a polar domains: Oil dispersed particles have a different structure compared to the water and dry particles for the first unit cells, that could be explained by a different orientation of the domains. The reduced order in the dry particles compared to the water dispersed particles could be due to a reduction in domain width.

20 nm crystallites and smaller are characterized by a large influence from the dispersion medium on the average structure, where the water dispersed particles have an ionic expansion both on average and local scale and increased strain on the surface measured by Raman spectroscopy. This is interpreted as a coexistence of a polarization and a vortex state, where the ionic shielding increases the ionic expansion in the polarization region, while straining the dipoles in the vortex state. No definitive conclusions about the dipole order can be drawn from this work.

These results illuminate the uncertainties connected to using only one method for structure characterization, as the conclusions about the influence of the dispersion medium would be very different depending on the characterization method used.

Bibliography

[1] Gordon E. Moore. "Cramming more components onto integrated circuits". *Proceedings of the IEEE*, 86 (1998): 82–85.

[2] G. I. Meijer. "Who wins the nonvolatile memory race?" *Science*, 319 (2008): 1625–1626.

[3] T. Mikolajick, C. Dehm, W. Hartner, I. Kasko, M.J. Kastner, N. Nagel, M. Moert, and C. Mazure. "FeRAM technology for high density applications". *Microelectronics Reliability*, 41 (2001): 947–950.

[4] R. Ramesh, S. Aggarwal, and O. Auciello. "Science and technology of ferroelectric films and heterostructures for non-volatile ferroelectric memories". *Materials Science and Engineering: R: Reports*, 32 (2001): 191–236.

[5] P. Wurfel and I. P. Batra. "Depolarization-field-induced instability in thin ferroelectric films — experiment and theory". *Physical Review B*, 8 (1973): 5126.

[6] I. P. Batra, P. Wurfel, and B. D. Silverman. "Phase transition, stability, and depolarization field in ferroelectric thin films". *Physical Review B*, 8 (1973): 3257.

[7] Thomas Tybell, C. H. Ahn, and J. M. Triscone. "Ferroelectricity in thin perovskite films". *Applied physics letters*, 75 (1999): 856–858.

[8] Javier Junquera and Philippe Ghosez. "Critical thickness for ferroelectricity in perovskite ultrathin films". *Nature*, 422 (2003): 506–509.

[9] Kenji Uchino, Eiji Sadanaga, and Terukiyo Hirose. "Dependence of the crystal structure on particle size in barium titanate". *Journal of the American Ceramic Society*, 72 (1989): 1555–1558.

[10] Dillon D. Fong, G. Brian Stephenson, Stephen K. Streiffer, Jeffrey A. Eastman, Orlando Auciello, Paul H. Fuoss, and Carol Thompson. "Ferroelectricity in ultrathin perovskite films". *Science*, 304 (2004): 1650–1653.

[11] Soma Chattopadhyay, Pushan Ayyub, V. R. Palkar, and Manu Multani. "Size-induced diffuse phase transition in the nanocrystalline ferroelectric $PbTiO_3$". *Physical Review B*, 52 (1995): 13177.

[12] Mark J. Polking, Myung-Geun Han, Amin Yourdkhani, Valeri Petkov, Christian F. Kisielowski, Vyacheslav V. Volkov, Yimei Zhu, Gabriel Caruntu, A. Paul Alivisatos, and Ramamoorthy Ramesh. "Ferroelectric order in individual nanometre-scale crystals". *Nature materials*, 11 (2012): 700–709.

[13] M. S. Senn, D. A. Keen, T. C. A. Lucas, J. A. Hriljac, and A. L. Goodwin. "Emergence of Long-Range Order in $BaTiO_3$ from Local Symmetry-Breaking Distortions". 207602.May (2016): 1–5.

[14] Malcolm E. Lines and Alastair M. Glass. *Principles and applications of ferroelectrics and related materials*. Oxford university press, 1977.

[15] Karin Rabe, Matthew Dawber, Céline Lichtensteiger, Charles Ahn, and Jean-Marc Triscone. "Modern physics of ferroelectrics: essential background". *Physics of Ferroelectrics* (2007): 1–30.

[16] Koichi Momma and Fujio Izumi. "VESTA 3 for three-dimensional visualization of crystal, volumetric and morphology data". *Journal of Applied Crystallography*, 44 (2011): 1272–1276.

[17] Da Yong Lu, Wei Cheng, Peng Yuan Chen, and Xiu Yun Sun. "Temperature correction for ceramic powder X-ray diffraction at a higher temperature". 718 (2013): 768–772.

[18] A. Rother, M. Reibold, H. Lichte, T. Leisegang, A.A. Levin, P. Paufler, D.C. Meyer, S. Gemming, I. Chaplygin, and G. Seifert. "X-ray investigation, high-resolution electron holography, and density functional calculations of single-crystalline $BaTiO_3$". *Physical Review B*, 74 (2006): 134116.

[19] Ronald E. Cohen. "Origin of ferroelectricity in perovskite oxides". *Nature*, 358 (1992): 136–138.

[20] Yoshihiro Kuroiwa, Shinobu Aoyagi, Akikatsu Sawada, Jimpei Harada, Eiji Nishibori, Masaki Takata, and Makoto Sakata. "Evidence for Pb-O covalency in tetragonal $PbTiO_3$". *Physical Review Letters*, 87 (2001): 217601.

[21] M Posternak, R Resta, and A Baldereschi. "Role of covalent bonding in the polarization of perovskite oxides: the case of $KNbO_3$". *Physical Review B*, 50 (1994): 8911.

[22] Katharine Page, Thomas Proffen, Markus Niederberger, and Ram Seshadri. "Probing local dipoles and ligand structure in $BaTiO_3$ nanoparticles". *Chemistry of Materials*, 22 (2010): 4386–4391.

[23] Elena Aksel and Jacob L Jones. "Advances in lead-free piezoelectric materials for sensors and actuators". *Sensors*, 10 (2010): 1935–1954.

[24] Yasuhiro Yoneda, Yoshiki Kohmura, and Yoshio Suzuki. "X-ray Diffraction Topography of $BaTiO_3$ at Phase Transition Temperature". *Japanese Journal of Applied Physics*, 48.9 (2009): 09KF01.

[25] C. Henry. "Size effects on structure and morphology of free or supported nanoparticles" (2008): 3–34.

[26] Vasili Perebeinos, Siu-Wai Chan, and Feng Zhang. "'Madelung model' prediction for dependence of lattice parameter on nanocrystal size". *Solid state communications*, 123 (2002): 295–297.

[27] S. Tsunekawa, K. Ishikawa, Z. Q. Li, Y. Kawazoe, and A. Kasuya. "Origin of anomalous lattice expansion in oxide nanoparticles". *Physical Review Letters*, 85 (2000): 3440.

[28] E. Koray Akdogan and Ahmad Safari. "Phenomenological theory of size effects on the cubic-tetragonal phase transition in $BaTiO_3$ nanocrystals". *Japanese journal of applied physics*, 41 (2002): 7170.

[29] Ming-Sheng Zhang, Jian Yu, Junhao Chu, Qiang Chen, and Wanchun Chen. "Microstructures and photoluminescence of barium titanate nanocrystals synthesized by the hydrothermal process". *Journal of materials processing technology*, 137 (2003): 78–81.

[30] Pushan Ayyub, V. R. Palkar, Soma Chattopadhyay, and Manu Multani. "Effect of crystal size reduction on lattice symmetry and cooperative properties". *Physical Review B*, 51 (1995): 6135.

[31] Millicent B. Smith, Katharine Page, Theo Siegrist, Peter L. Redmond, Erich C. Walter, Ram Seshadri, Louis E. Brus, and Michael L. Steigerwald. "Crystal structure and the paraelectric-to-ferroelectric phase transition of nanoscale $BaTiO_3$". *Journal of the American Chemical Society*, 130 (2008): 6955–6963.

[32] Jon F. Ihlefeld, David T. Harris, Ryan Keech, Jacob L. Jones, Jon-Paul Maria, and Susan Trolier-McKinstry. "Scaling Effects in Perovskite Ferroelectrics: Fundamental Limits and Process-Structure-Property Relations". *Journal of the American Ceramic Society*, 99 (2016): 2537–2557.

[33] A. Schilling, R.M. Bowman, G. Catalan, J.F. Scott, and J.M. Gregg. "Morphological control of polar orientation in single-crystal ferroelectric nanowires". *Nano letters*, 7.12 (2007): 3787–3791.

[34] C.T. Nelson, B. Winchester, Y. Zhang, S.J. Kim, A. Melville, C. Adamo, C. M Folkman, S.H. Baek, C.B. Eom, and D.G. Schlom. "Spontaneous vortex nanodomain arrays at ferroelectric heterointerfaces". *Nano Letters*, 11.2 (2011): 828–834.

[35] Ivan Naumov and Huaxiang Fu. "Vortex-to-polarization phase transformation path in ferroelectric $Pb(ZrTi)O_3$ nanoparticles". *Physical review letters*, 98.7 (2007): 077603.

[36] I. Naumov, L. Bellaiche, and H. Fu. "Unusual phase transitions inferroelectric nanodisks and nanorods". *Nature*, 432.7018 (2004): 1–4.

[37] J. M. Gregg. "Exotic domain states in ferroelectrics: Searching for vortices and skyrmions". *Ferroelectrics*, 433.1 (2012): 74–87.

[38] Simon JL Billinge. "Nanoscale structural order from the atomic pair distribution function (PDF): There's plenty of room in the middle". *Journal of Solid State Chemistry*, 181.7 (2008): 1695–1700.

[39] Valeri Petkov, Milen Gateshki, Markus Niederberger, and Yang Ren. "Atomic-scale structure of nanocrystalline $Ba_xSr_{1-x}TiO_3$ (x = 1, 0.5, 0) by X-ray diffraction and the atomic pair distribution function technique". *Chemistry of Materials*, 18.3 (2006): 814–821.

[40] Satoshi Tominaka, Akimitsu Ishihara, Takaaki Nagai, and Ken-ichiro Ota. "Non-crystalline Titanium Oxide Catalysts for Electrochemical Oxygen Reduction Reactions". *ACS Omega*, 2.8 (2017): 5209–5214.

[41] Satoshi Tominaka, Kohsaku Kawakami, Mayuko Fukushima, and Aoi Miyazaki. "Physical Stabilization of Pharmaceutical Glasses Based on Hydrogen Bond Reorganization under Sub-T g Temperature". *Molecular pharmaceutics*, 14.1 (2016): 264–273.

[42] V. Petkov, V. Buscaglia, M. T. Buscaglia, Z. Zhao, and Y. Ren. "Structural coherence and ferroelectricity decay in submicron- and nano-sized perovskites". *Physical Review B*, 78.5 (2008): 1–7.

[43] V. Petkov, S. M. Selbach, M. A. Einarsrud, T. Grande, and S. D. Shastri. "Melting of Bi-sublattice in nanosized $BiFeO_3$ perovskite by resonant x-ray diffraction". *Physical Review Letters*, 105.18 (2010): 3–6.

[44] Bo Jiang, Trygve M. Ræder, De-Ye Lin, Tor Grande, and Sverre M. Selbach. "Structural Disorder and Coherence across the Phase Transitions of Lead-Free Piezoelectric $Bi_{0.5}K_{0.5}TiO_3$". *Chemistry of Materials*, 30.8 (2018): 2631–2640.

[45] Kauzo Nakamoto. *Infrared and Raman spectra of inorganic and coordination compounds, Pt. A : Theory and applications in inorganic chemistry*. Wiley, 1997.

[46] Wei An, Tian Hui Liu, Chun Hai Wang, Chuan Ling Diao, Neng Neng Luo, Yong Liu, Ze Ming Qi, Tao Shao, Yu Yin Wang, Huan Jiao, Guang Shan Tian, and Xi Ping Jing. "Assignment for vibrational spectra of $BaTiO_3$ ferroelectric ceramic based on the first-principles calculation". *Acta Physico - Chimica Sinica*, 31.6 (2015): 1059–1068.

[47] Y. Shiratori, C. Pithan, J. Dornseiffer, and R. Waser. "Raman Scattering studies on nanocrystalline $BaTiO_3$, Part 1 - isolated particles and aggregates". *Journal of Raman Spectroscopy*, 38.April (2007): 1538–1553.

[48] Antoine Dalod, Lars Henriksen, Tor Grande, and Mari-Ann Einarsrud. "Functionalized TiO_2 nanoparticles by single-step hydrothermal synthesis: the role of the silane coupling agents". *Beilstein journal of nanotechnology*, 8 (2017): 304.

[49] Per Martin Rørvik, Tor Grande, and Mari-Ann Einarsrud. "Hierarchical $PbTiO_3$ nanostructures grown on $SrTiO_3$ substrates". *Crystal Growth and Design*, 9 (2009): 1979–1984.

[50] Daniel Morales, Nicholas A. Stoute, Zhiyuan Yu, David E. Aspnes, and Michael D. Dickey. "Liquid gallium and the eutectic gallium indium (EGaIn) alloy: Dielectric functions from 1.24 to 3.1 eV by electrochemical reduction of surface oxides". *Applied Physics Letters*, 109.9 (2016).

[51] Hu Lizhi, K. Toyoda, and I. Ihara. "Dielectric properties of edible oils and fatty acids as a function of frequency, temperature, moisture and composition". *Journal of Food Engineering*, 88.2 (2008): 151–158.

[52] Benton B Owen, Robert C Miller, Clifford E Milner, and Harold L Cogan. "The Dielectric Constant of Water As a Function of Temperature and Pressure1, 2". *The Journal of Physical Chemistry*, 65.11 (1961): 2065–2070.

[53] A. Rother, M. Reibold, H. Lichte, T. Leisegang, A. A. Levin, P. Paufler, D. C. Meyer, S. Gemming, I. Chaplygin, G. Seifert, A. Ormeci, and H. Rosner. "X-ray investigation, high-resolution electron holography, and density functional calculations of single-crystalline $BaTiO_3$". *Physical Review B*, 74.13 (2006): 1–8.

[54] BM Auer and JL Skinner. "IR and Raman spectra of liquid water: Theory and interpretation". *The Journal of chemical physics*, 128.22 (2008): 224511.

[55] Vincent Baeten, Marc Meurens, Maria T Morales, and Ramon Aparicio. "Detection of virgin olive oil adulteration by Fourier transform Raman spectroscopy". *Journal of Agricultural and Food Chemistry*, 44.8 (1996): 2225–2230.

Appendices

Appendix A

Pawley fits for particles in all dispersion mediums

Pawley fit for all particles in all dispersion mediums, using both tetragonal $P4mm$ and cubic $Pm\bar{3}m$ symmetry. Size, symmetry and the agreement factor R_{wp} is written in the figures, where the data is marked as gray circles and the Pawley fit is marked as the colored line, with the color marking the dispersion medium: dry (red), oil (oil), water (blue) and eutectic GaIn (green).

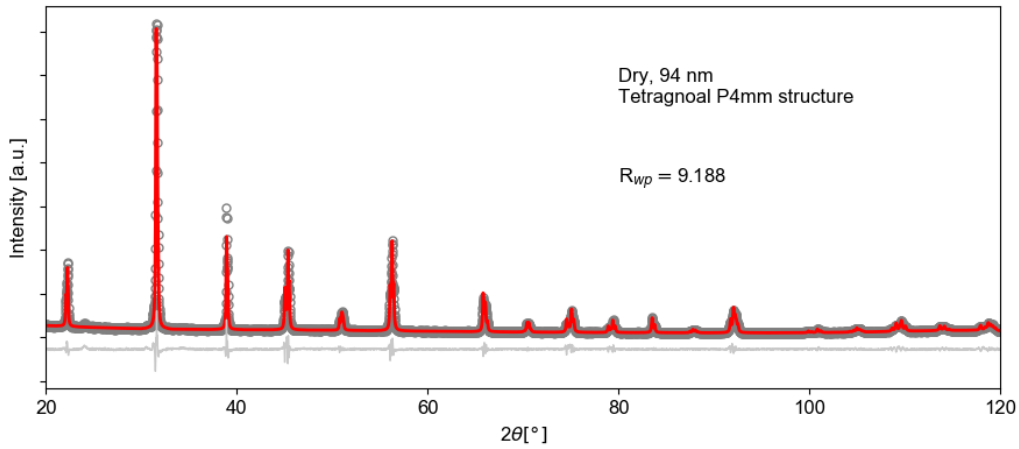
Dry, 94 nm
Tetragnoal P4mm structure
R_{wp} = 9.188
Intensity [a.u.]
20
40
60
80
100
120
2θ[°]

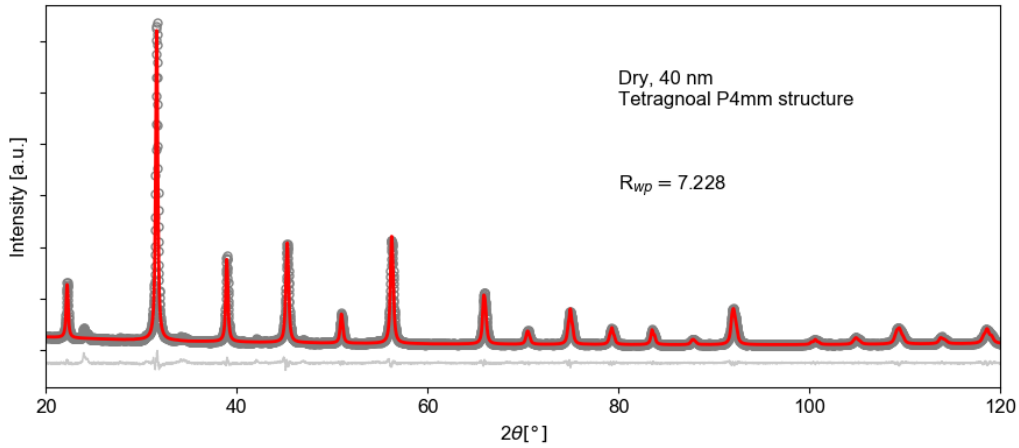
Dry, 40 nm
Tetragnoal P4mm structure
R_{wp} = 7.228
Intensity [a.u.]
20
40
60
80
100
120
2θ[°]

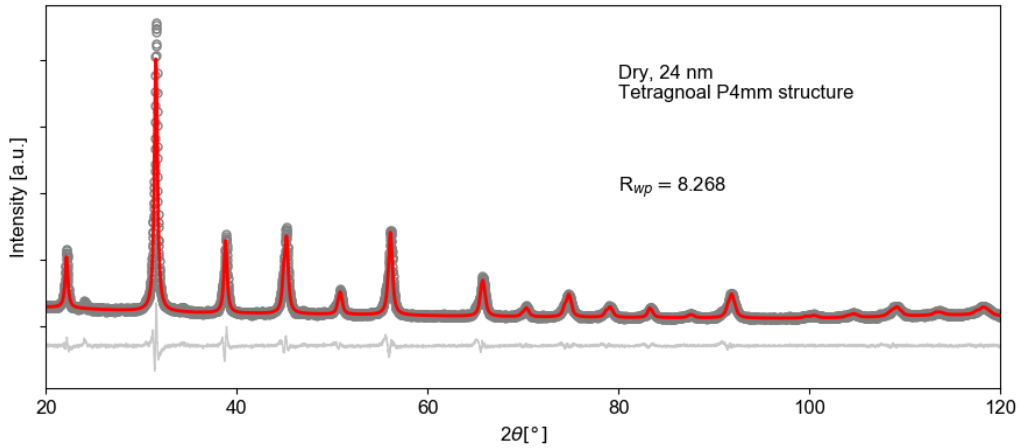
Dry, 24 nm
Tetragnoal P4mm structure
R_{wp} = 8.268
Intensity [a.u.]
20
40
60
80
100
120
2θ[°]

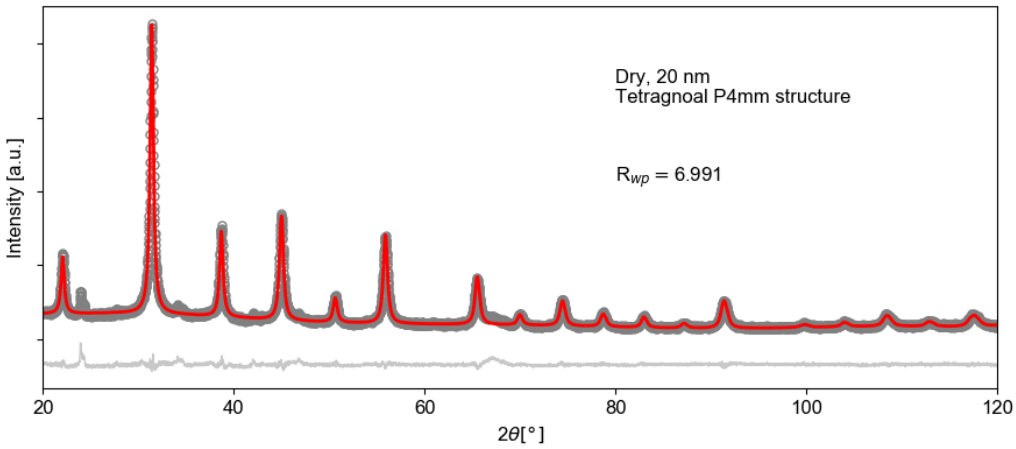
Dry, 20 nm
Tetragnoal P4mm structure
R_{wp} = 6.991
Intensity [a.u.]
20
40
60
80
100
120
2θ[°]

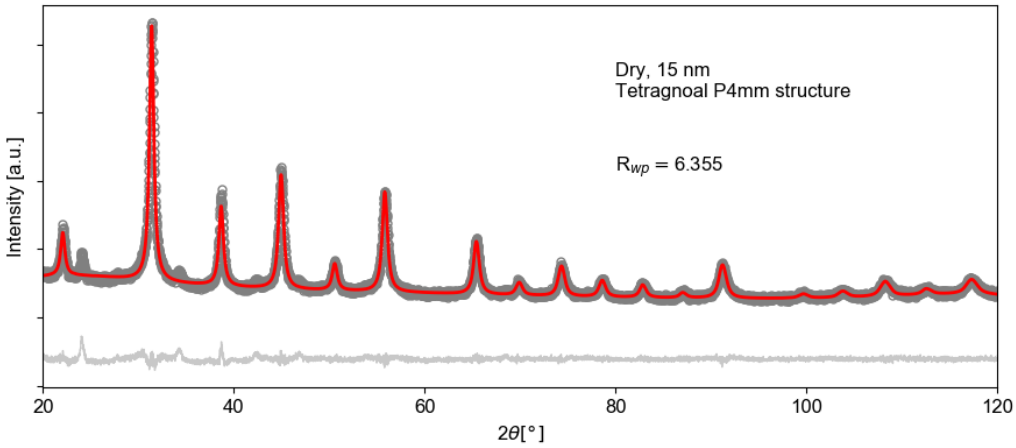
Dry, 15 nm
Tetragnoal P4mm structure
R_{wp} = 6.355
Intensity [a.u.]
20
40
60
80
100
120
2θ[°]

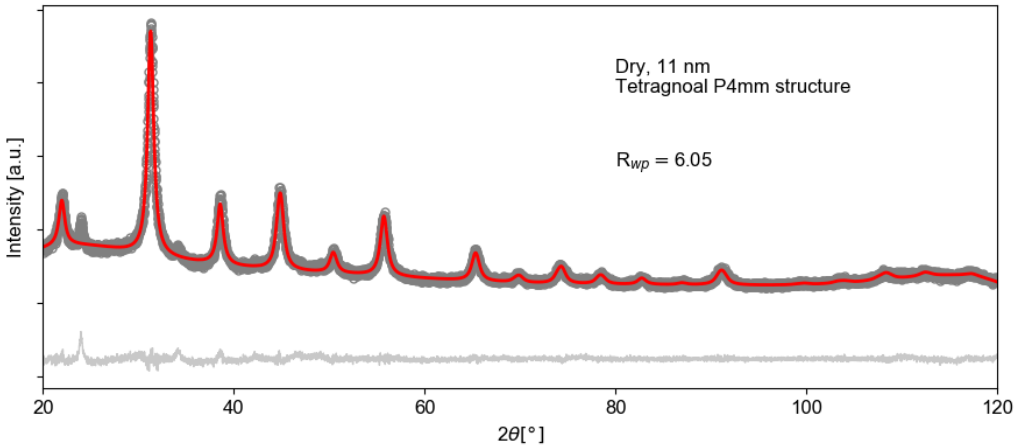
Dry, 11 nm
Tetragnoal P4mm structure
R_{wp} = 6.05
Intensity [a.u.]
20
40
60
80
100
120
2θ[°]

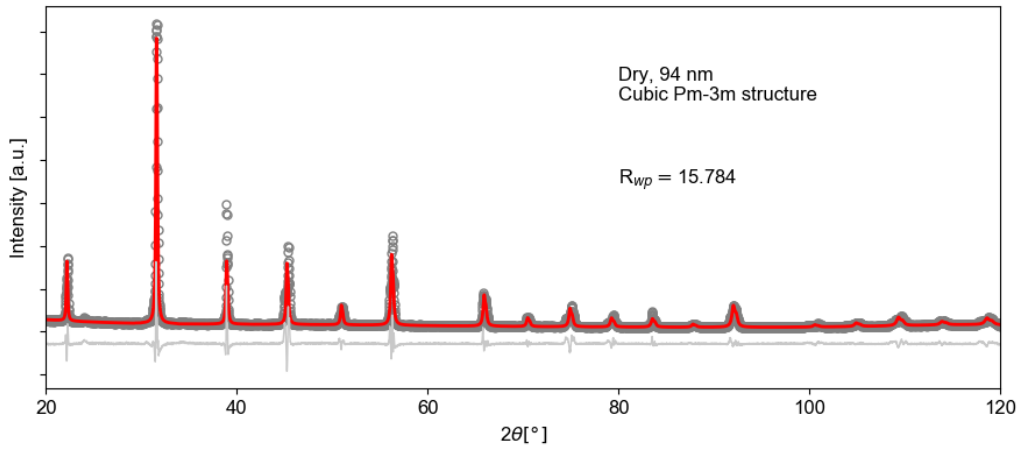
Dry, 94 nm
Cubic Pm-3m structure
R_{wp} = 15.784
Intensity [a.u.]
20
40
60
80
100
120
2θ[°]

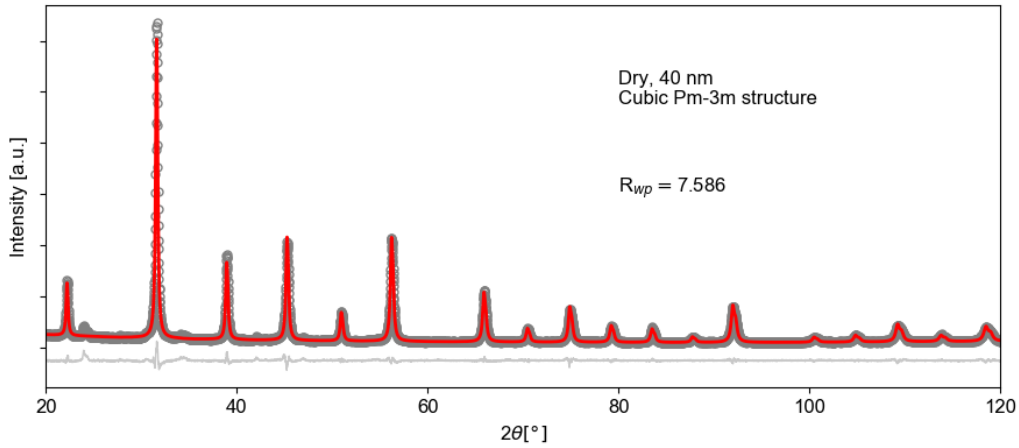
Dry, 40 nm
Cubic Pm-3m structure
R_{wp} = 7.586
Intensity [a.u.]
20
40
60
80
100
120
2θ[°]

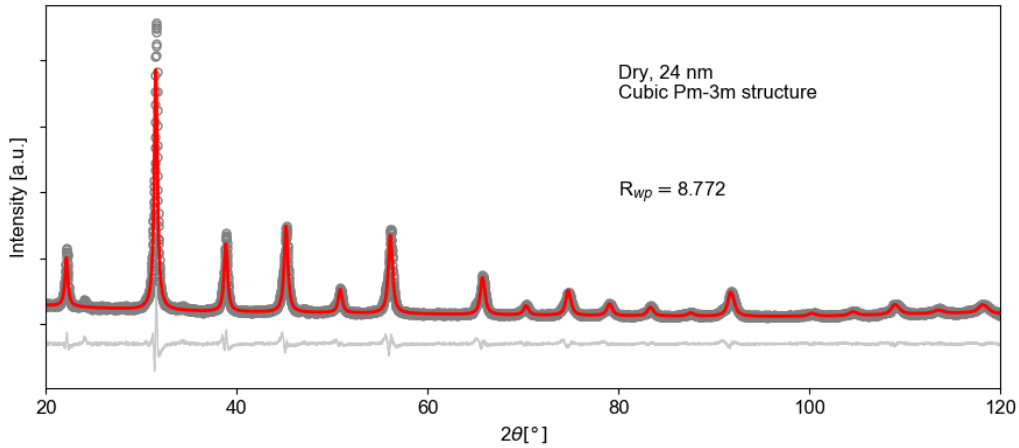
Dry, 24 nm
Cubic Pm-3m structure
R_{wp} = 8.772
Intensity [a.u.]
20
40
60
80
100
120
2θ[°]

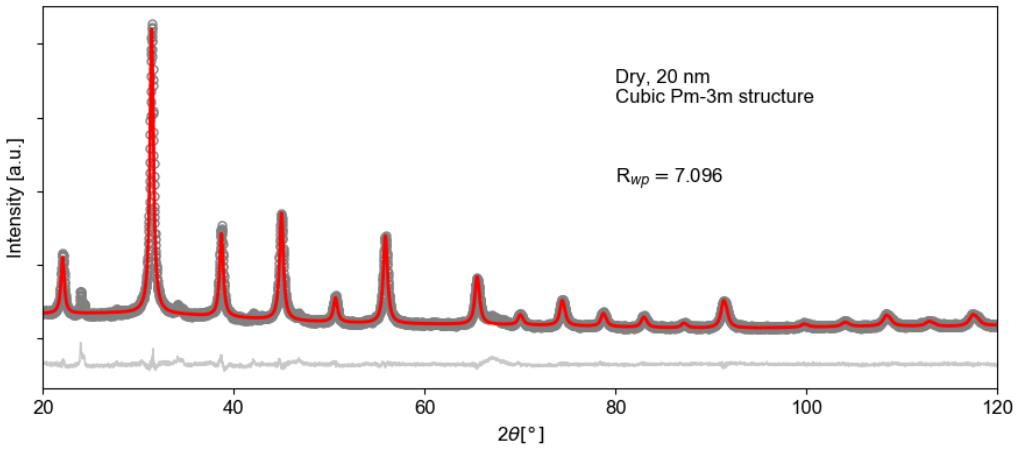
Dry, 20 nm
Cubic Pm-3m structure
R_{wp} = 7.096
Intensity [a.u.]
20
40
60
80
100
120
2θ[°]

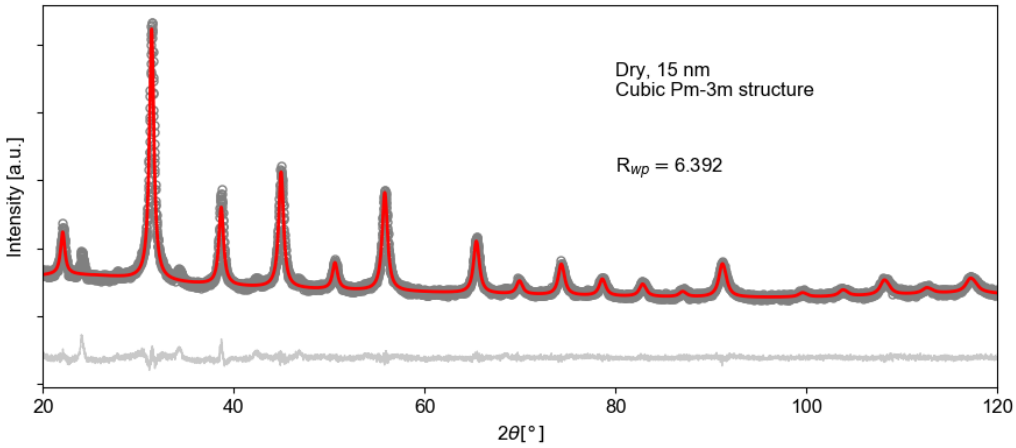
Dry, 15 nm
Cubic Pm-3m structure
R_{wp} = 6.392
Intensity [a.u.]
20
40
60
80
100
120
2θ[°]

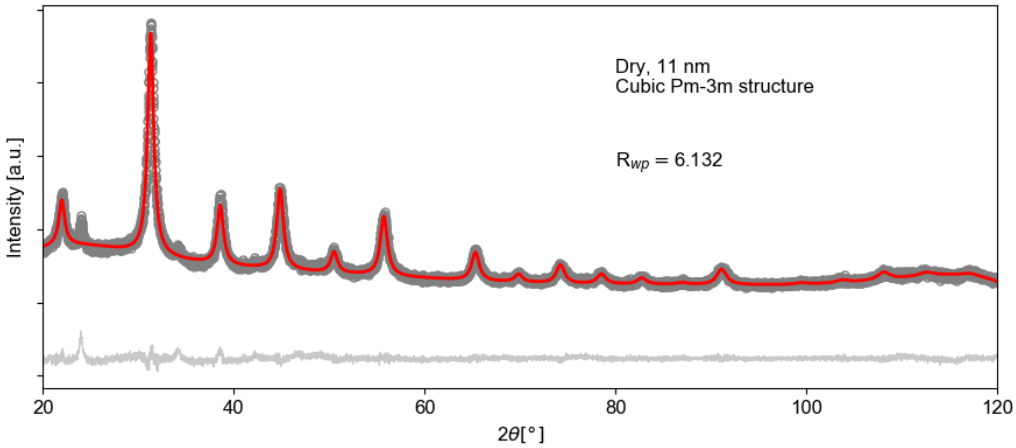
Dry, 11 nm
Cubic Pm-3m structure
R_{wp} = 6.132
Intensity [a.u.]
20
40
60
80
100
120
2θ[°]

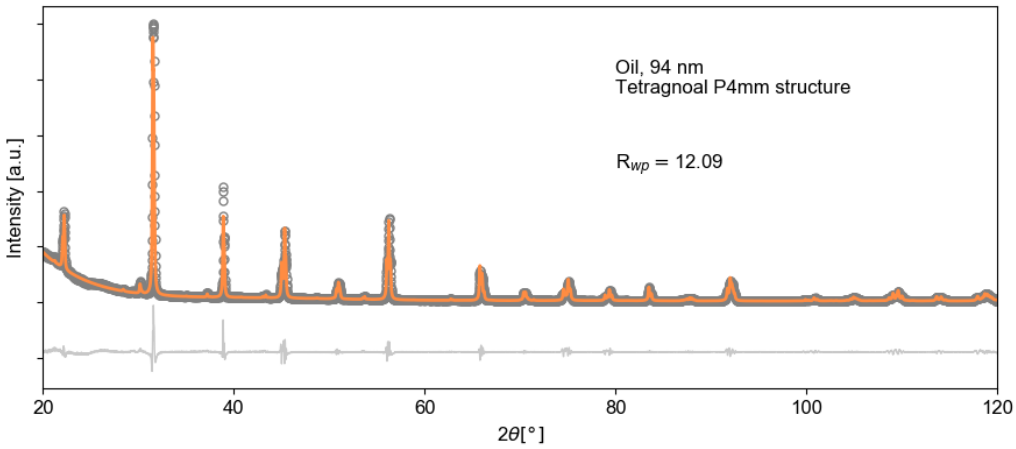
Oil, 94 nm
Tetragnoal P4mm structure
R_{wp} = 12.09
Intensity [a.u.]
20
40
60
80
100
120
2θ[°]

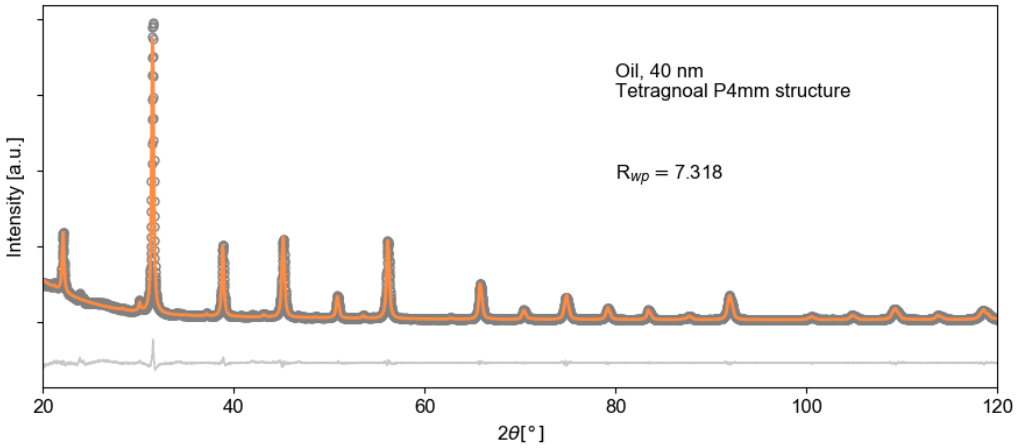
Oil, 40 nm
Tetragnoal P4mm structure
R_{wp} = 7.318
Intensity [a.u.]
20
40
60
80
100
120
2θ[°]

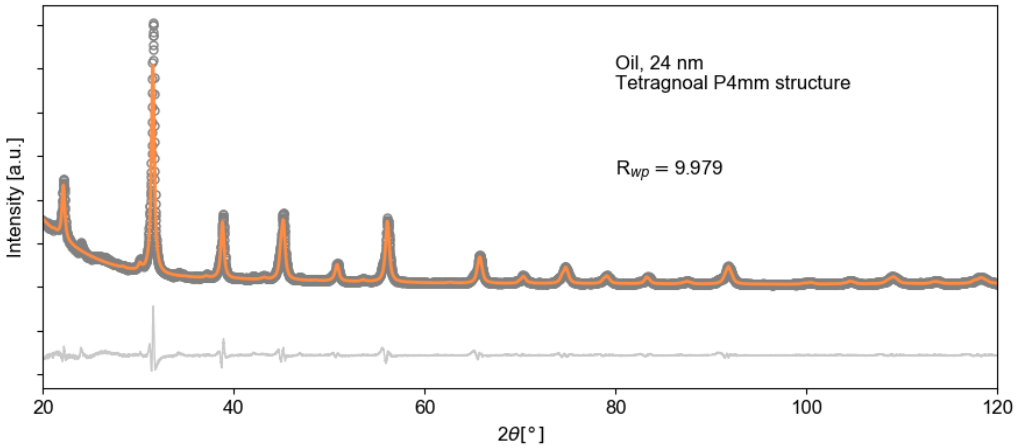
Oil, 24 nm
Tetragnoal P4mm structure
R_{wp} = 9.979
Intensity [a.u.]
20
40
60
80
100
120
2θ[°]

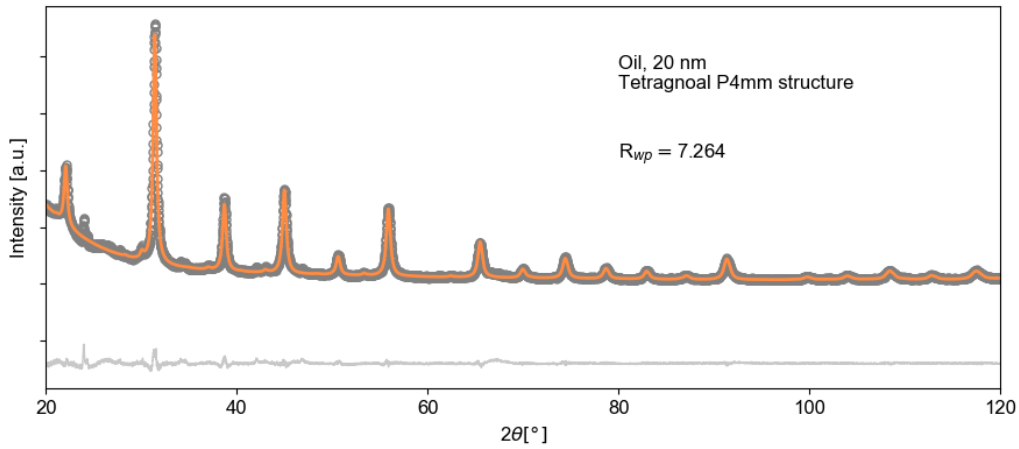
Oil, 20 nm
Tetragnoal P4mm structure
R_{wp} = 7.264
Intensity [a.u.]
20
40
60
80
100
120
2θ[°]

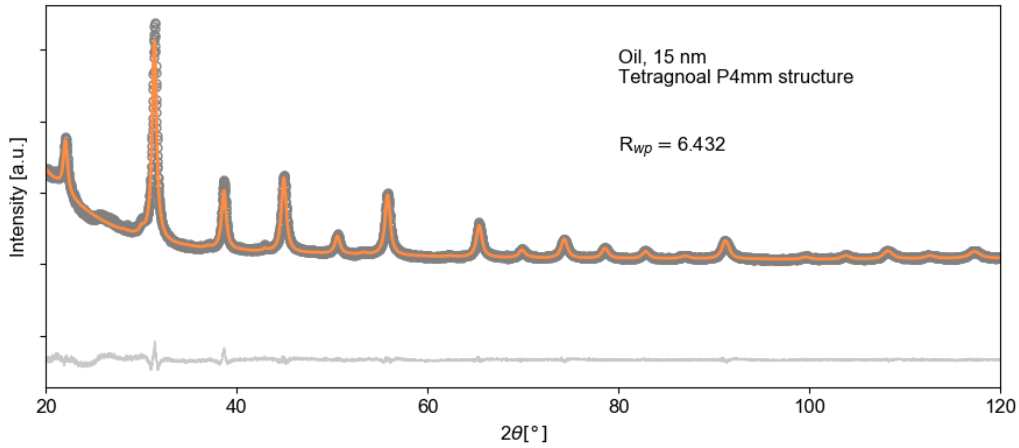
Oil, 15 nm
Tetragnoal P4mm structure
R_{wp} = 6.432
Intensity [a.u.]
20
40
60
80
100
120
2θ[°]

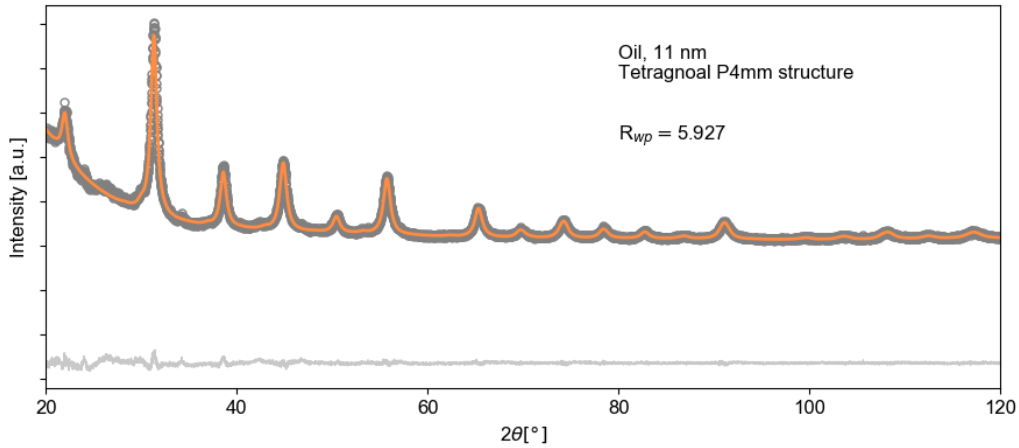
Oil, 11 nm
Tetragnoal P4mm structure
R_{wp} = 5.927
Intensity [a.u.]
20
40
60
80
100
120
2θ[°]

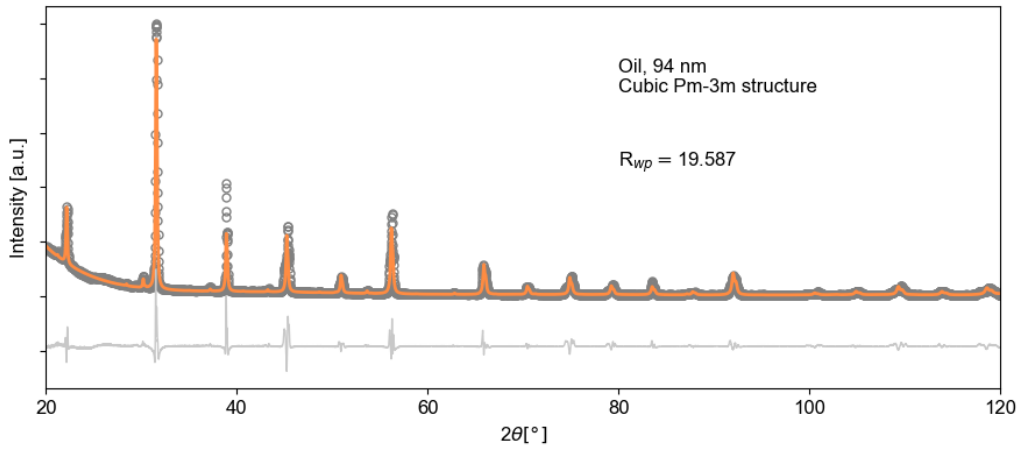
Oil, 94 nm
Cubic Pm-3m structure
R_{wp} = 19.587
Intensity [a.u.]
20
40
60
80
100
120
2θ[°]

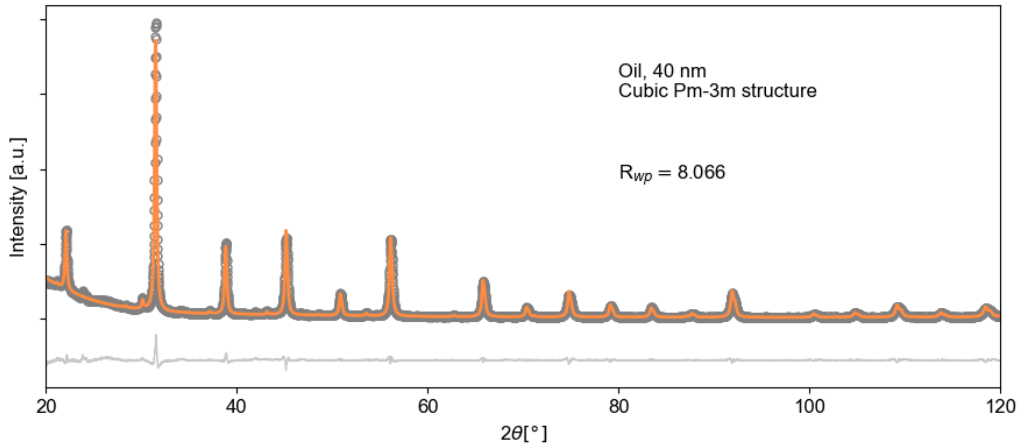
Oil, 40 nm
Cubic Pm-3m structure
R_{wp} = 8.066
Intensity [a.u.]
20
40
60
80
100
120
2θ[°]

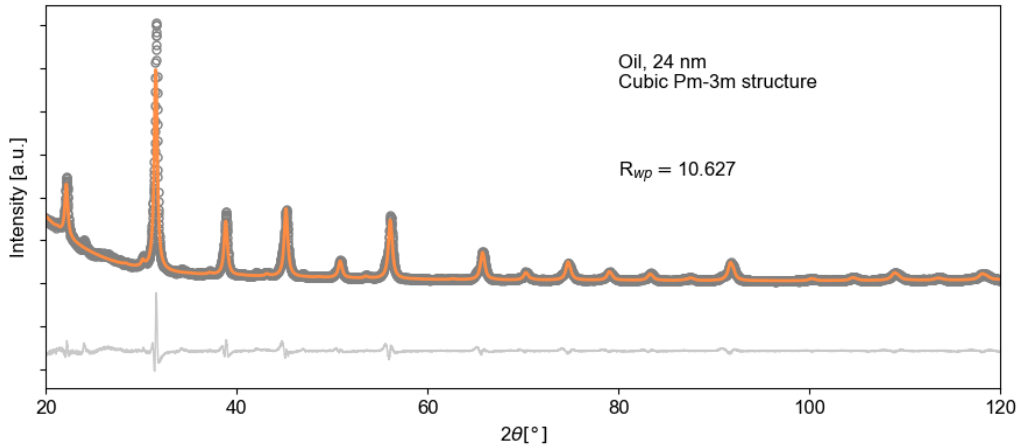
Oil, 24 nm
Cubic Pm-3m structure
R_{wp} = 10.627
Intensity [a.u.]
20
40
60
80
100
120
2θ[°]

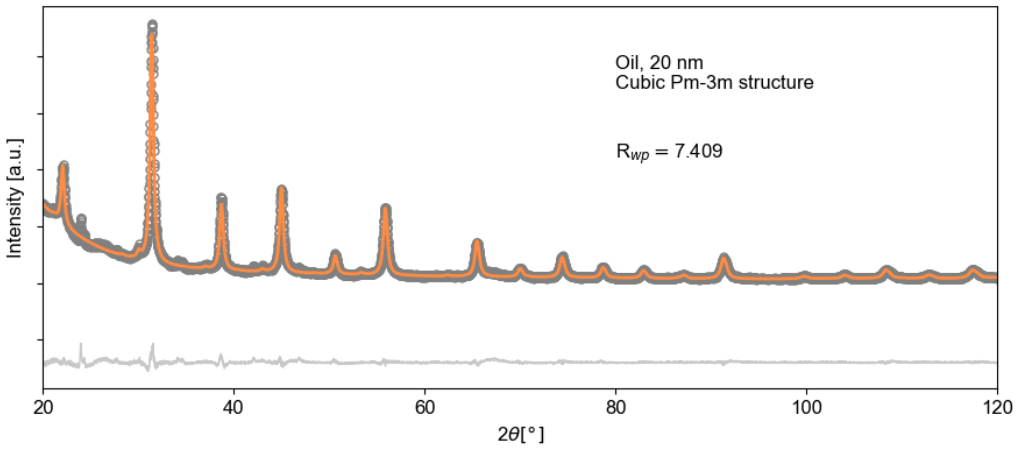
Oil, 20 nm
Cubic Pm-3m structure
R_{wp} = 7.409
Intensity [a.u.]
20
40
60
80
100
120
2θ[°]

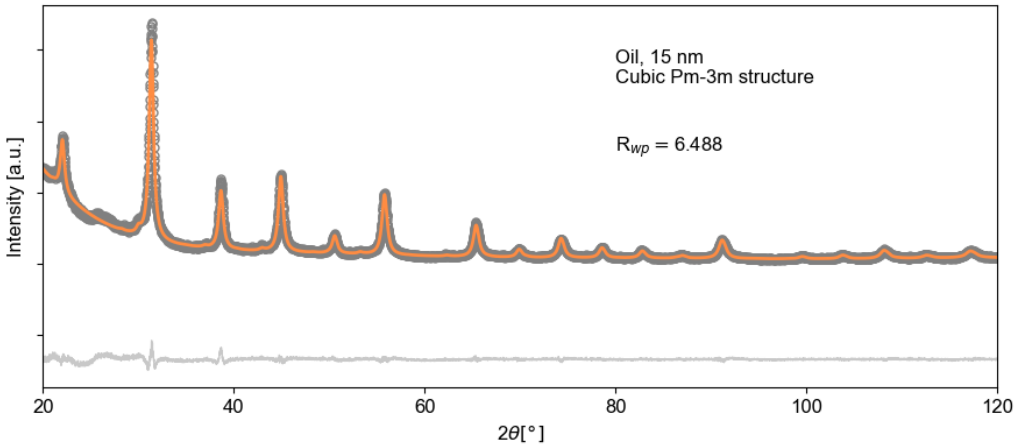
Oil, 15 nm
Cubic Pm-3m structure
R_{wp} = 6.488
Intensity [a.u.]
20
40
60
80
100
120
2θ[°]

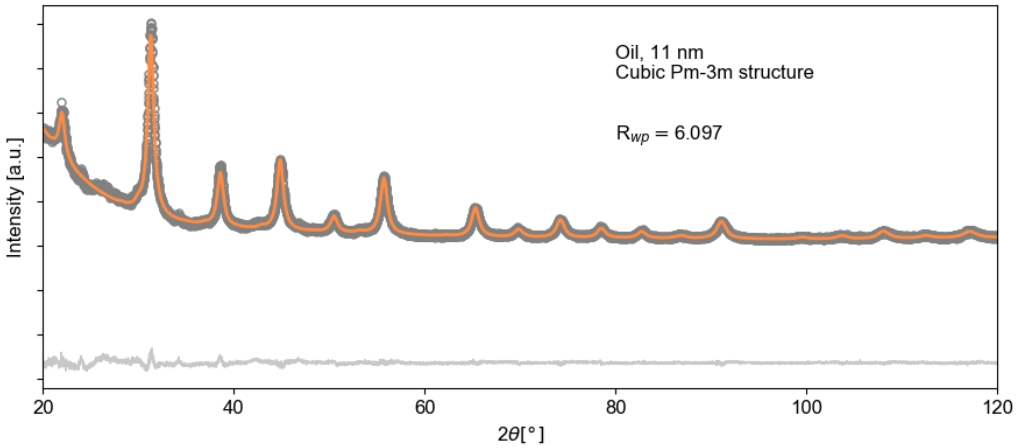
Oil, 11 nm
Cubic Pm-3m structure
R_{wp} = 6.097
Intensity [a.u.]
20
40
60
80
100
120
2θ[°]

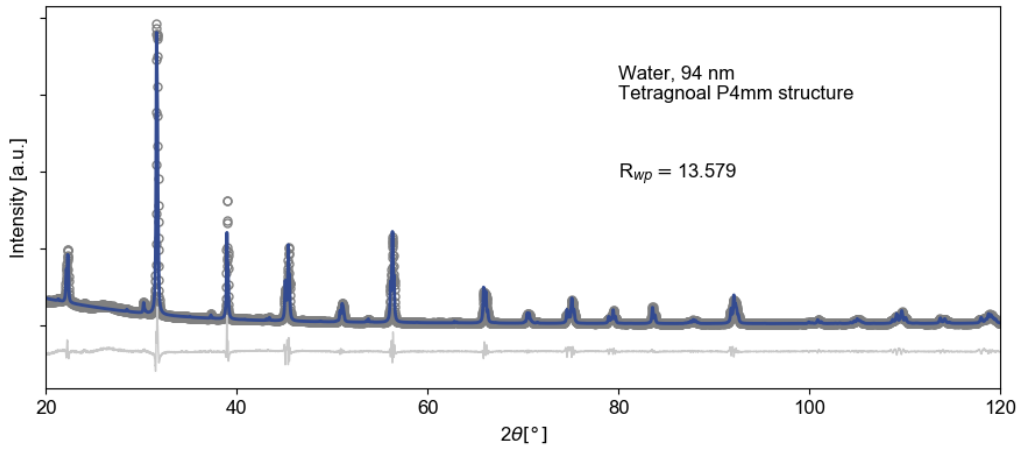
Water, 94 nm
Tetragnoal P4mm structure
R_{wp} = 13.579
Intensity [a.u.]
20
40
60
80
100
120
2θ[°]

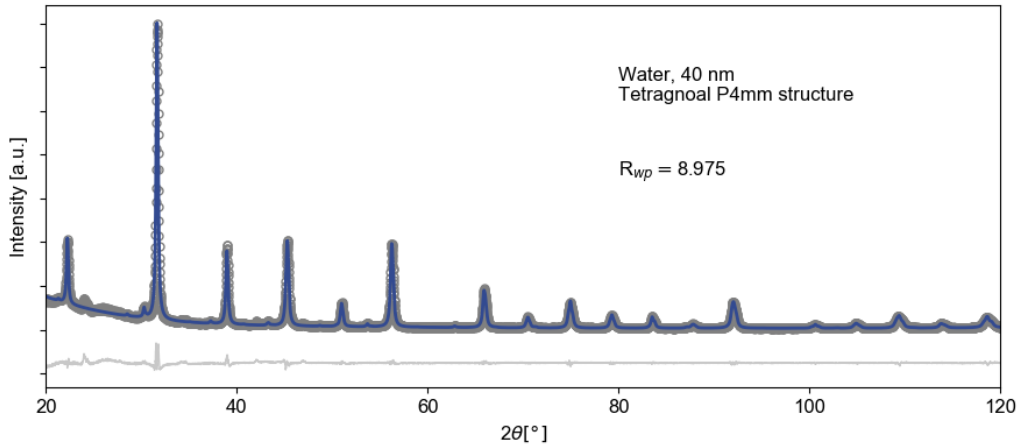
Water, 40 nm
Tetragnoal P4mm structure
R_{wp} = 8.975
Intensity [a.u.]
20
40
60
80
100
120
2θ[°]

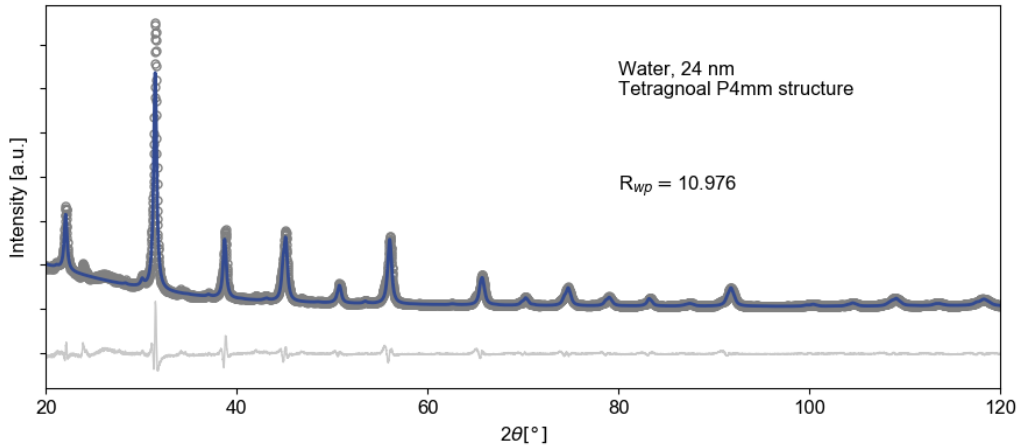
Water, 24 nm
Tetragnoal P4mm structure
R_{wp} = 10.976
Intensity [a.u.]
20
40
60
80
100
120
2θ[°]

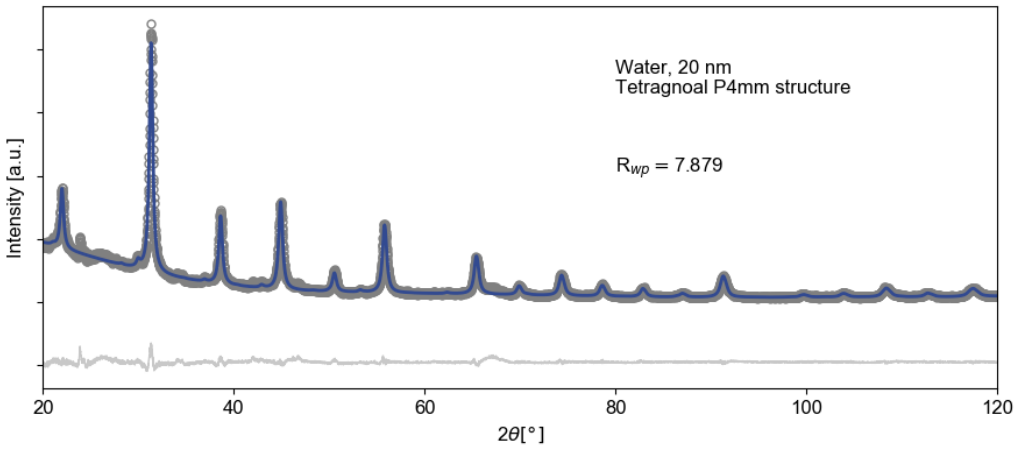
Water, 20 nm
Tetragnoal P4mm structure
R_{wp} = 7.879
Intensity [a.u.]
20
40
60
80
100
120
2θ[°]

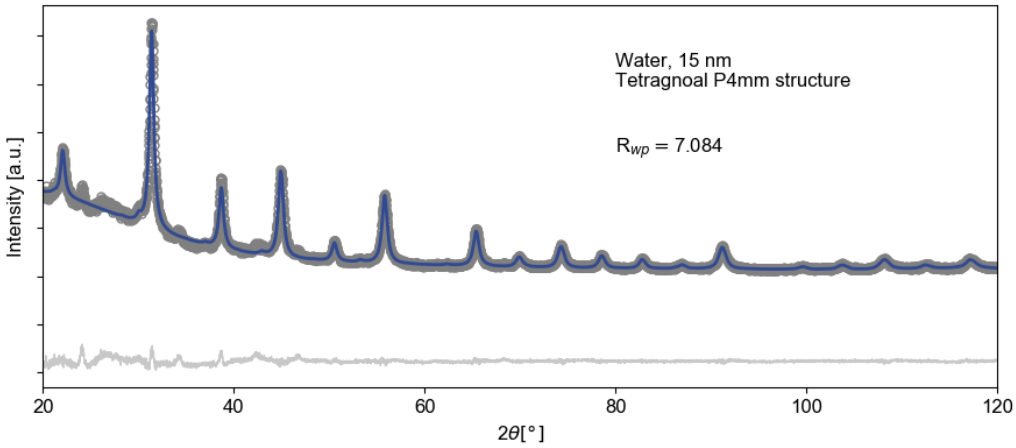
Water, 15 nm
Tetragnoal P4mm structure
R_{wp} = 7.084
Intensity [a.u.]
20
40
60
80
100
120
2θ[°]

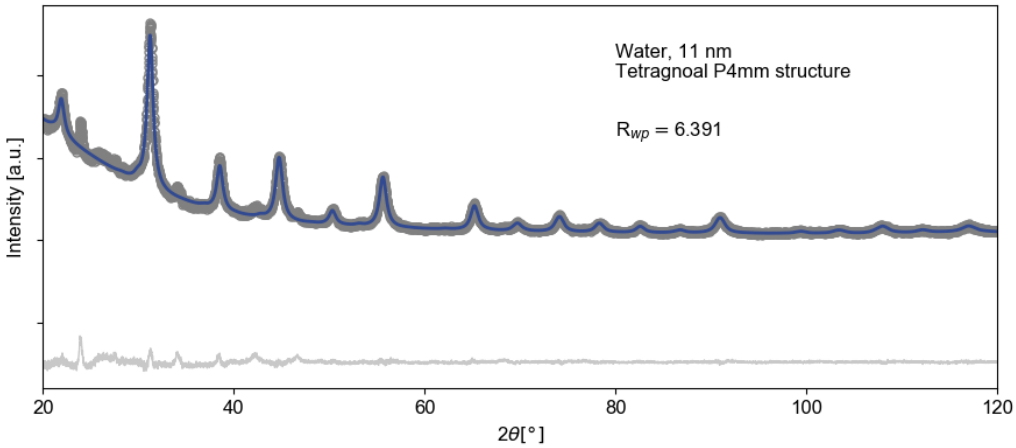
Water, 11 nm
Tetragnoal P4mm structure
R_{wp} = 6.391
Intensity [a.u.]
20
40
60
80
100
120
2θ[°]

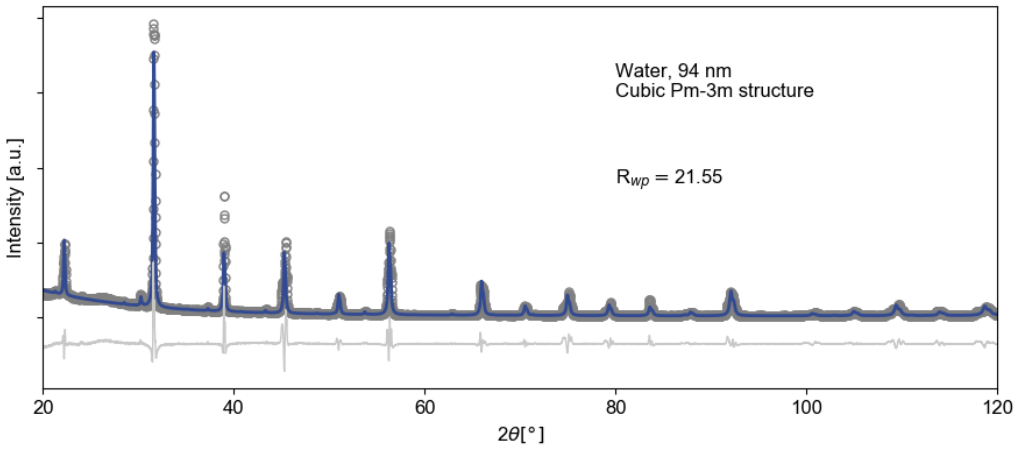
Water, 94 nm
Cubic Pm-3m structure
R_{wp} = 21.55
Intensity [a.u.]
20
40
60
80
100
120
2θ[°]

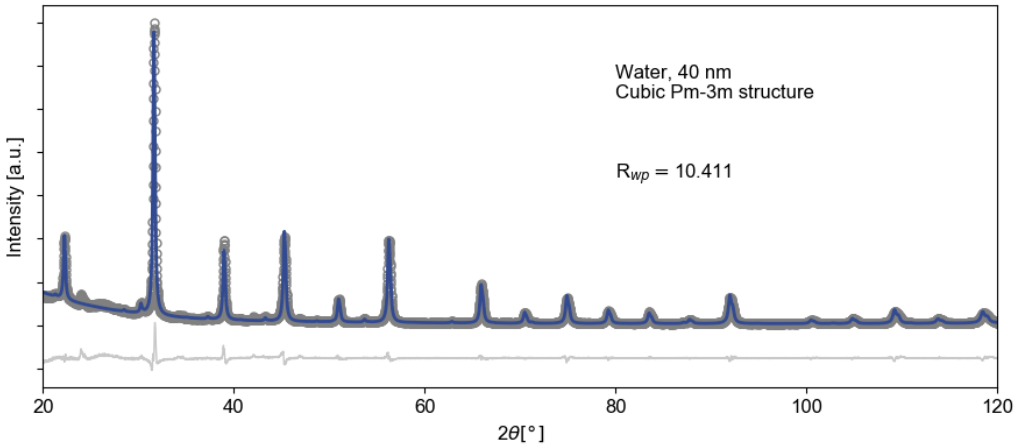
Water, 40 nm
Cubic Pm-3m structure
R_{wp} = 10.411
Intensity [a.u.]
20
40
60
80
100
120
2θ[°]

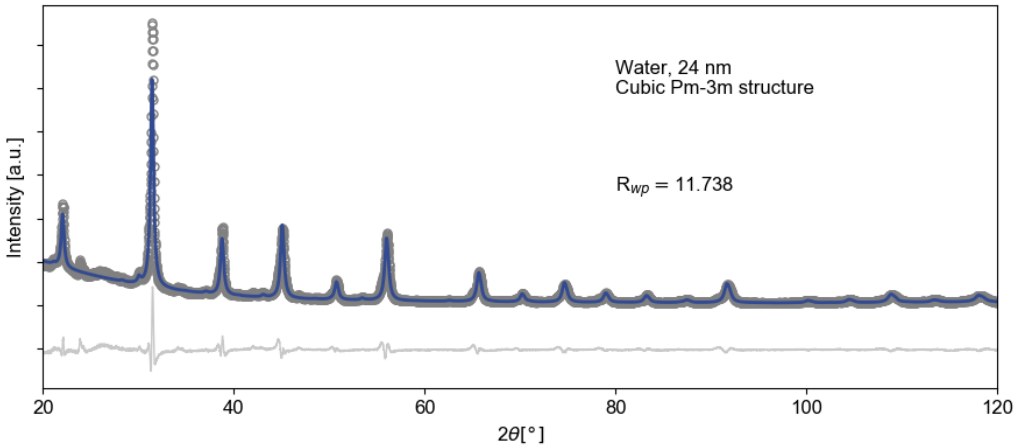
Water, 24 nm
Cubic Pm-3m structure
R_{wp} = 11.738
Intensity [a.u.]
20
40
60
80
100
120
2θ[°]

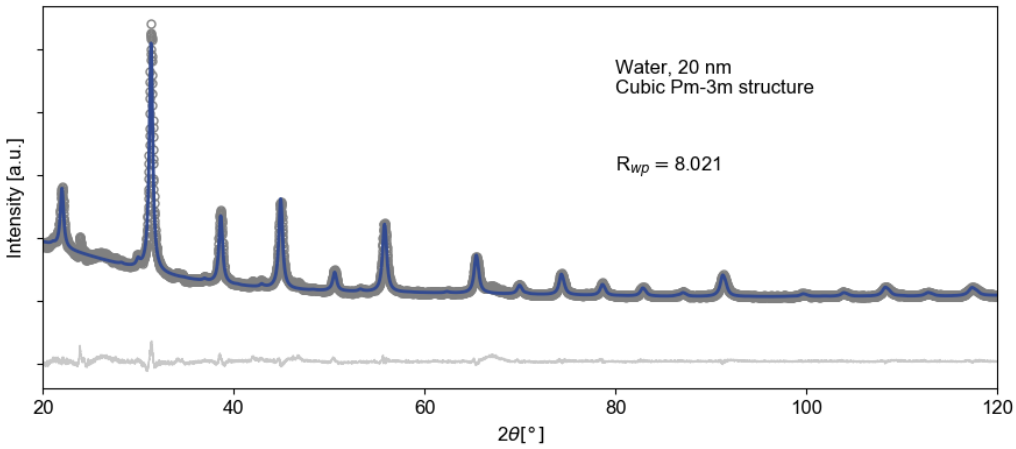
Water, 20 nm
Cubic Pm-3m structure
R_{wp} = 8.021
Intensity [a.u.]
20
40
60
80
100
120
2θ[°]

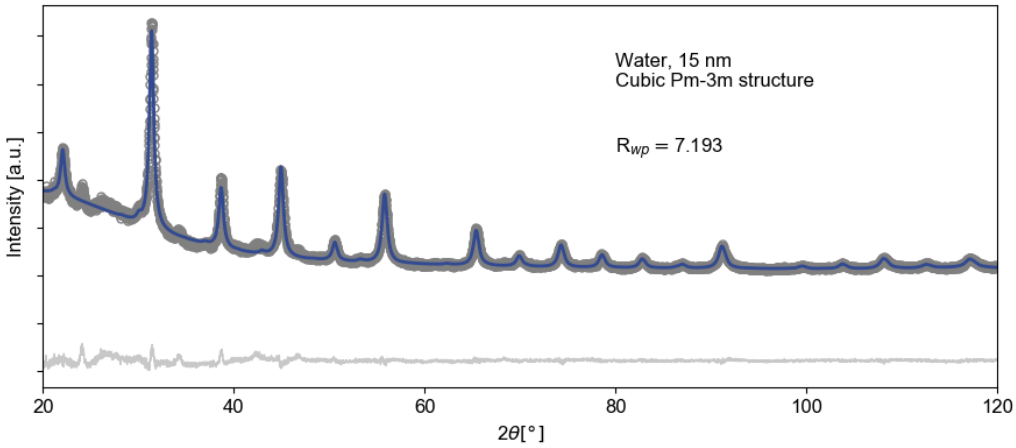
Water, 15 nm
Cubic Pm-3m structure
R_{wp} = 7.193
Intensity [a.u.]
20
40
60
80
100
120
2θ[°]

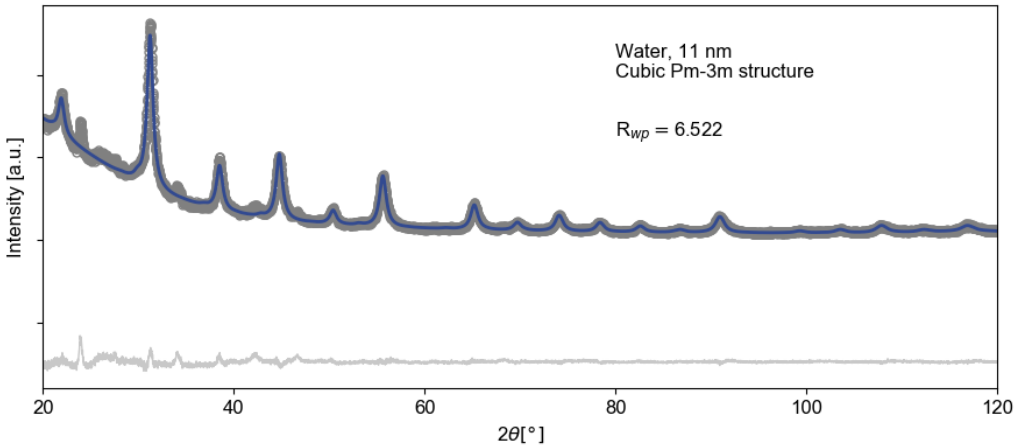
Water, 11 nm
Cubic Pm-3m structure
R_{wp} = 6.522
Intensity [a.u.]
20
40
60
80
100
120
2θ[°]

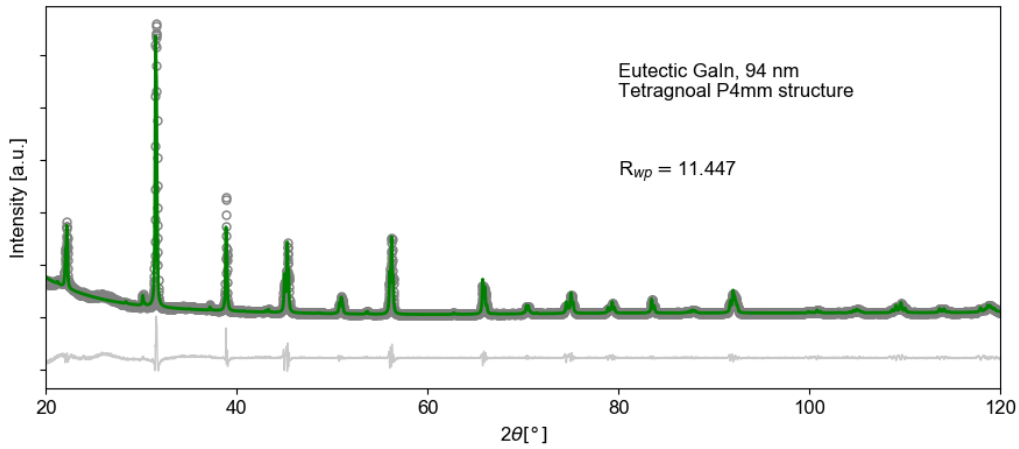
Eutectic GaIn, 94 nm
Tetragnoal P4mm structure
R_{wp} = 11.447
Intensity [a.u.]
20
40
60
80
100
120
2θ[°]

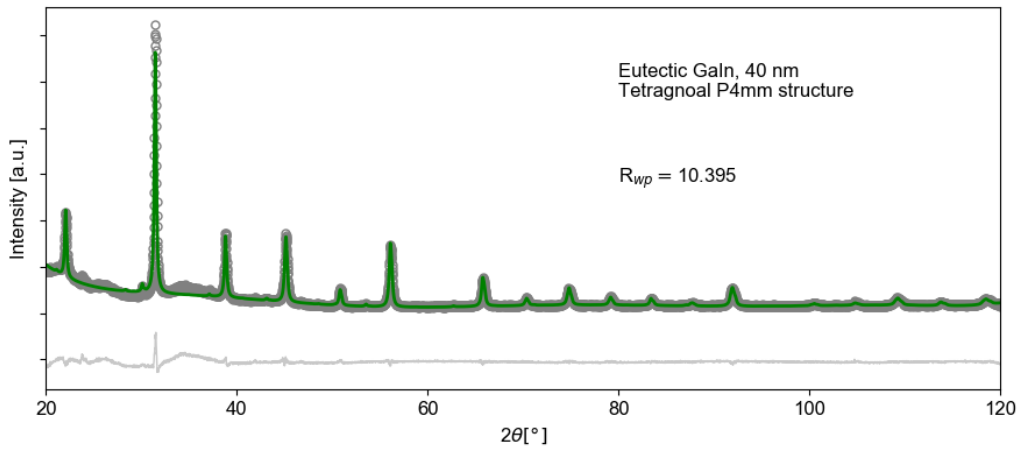
Eutectic GaIn, 40 nm
Tetragnoal P4mm structure
R_{wp} = 10.395
Intensity [a.u.]
20
40
60
80
100
120
2θ[°]

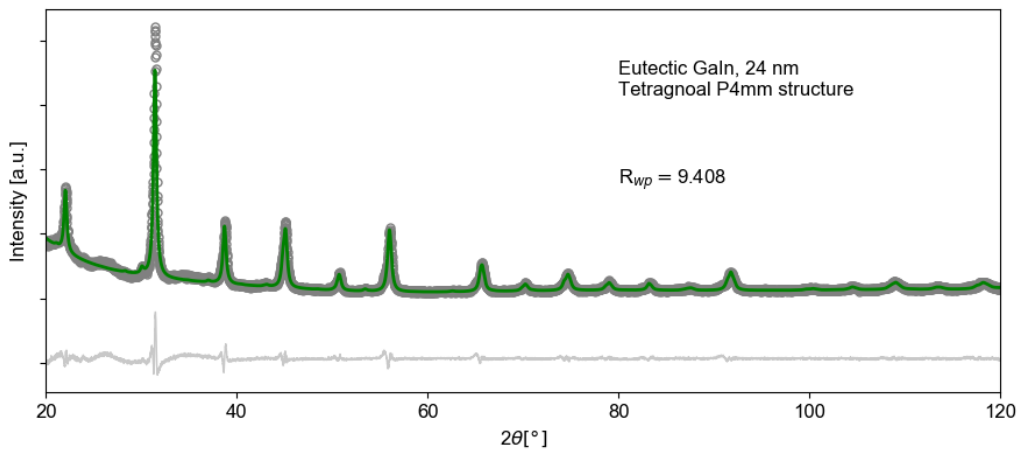
Eutectic GaIn, 24 nm
Tetragnoal P4mm structure
R_{wp} = 9.408
Intensity [a.u.]
20
40
60
80
100
120
2θ[°]

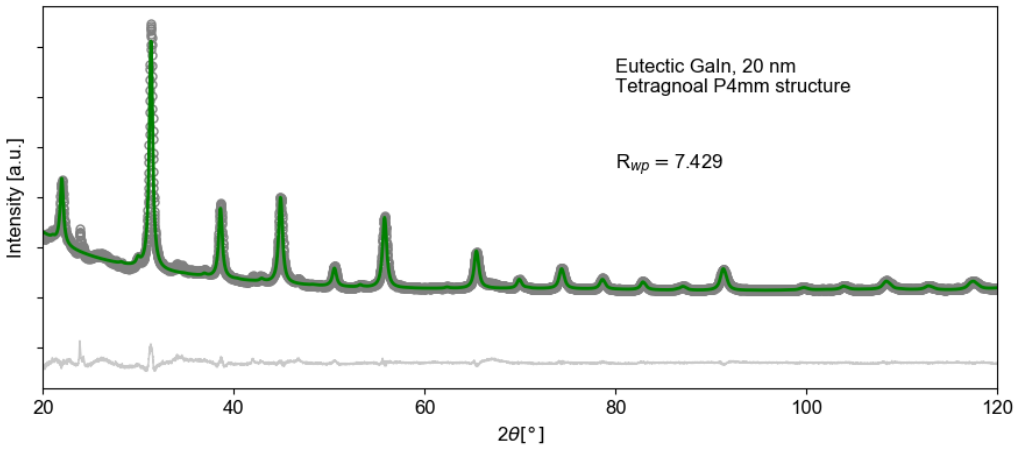
Eutectic GaIn, 20 nm
Tetragnoal P4mm structure
R_{wp} = 7.429
Intensity [a.u.]
20
40
60
80
100
120
2θ[°]

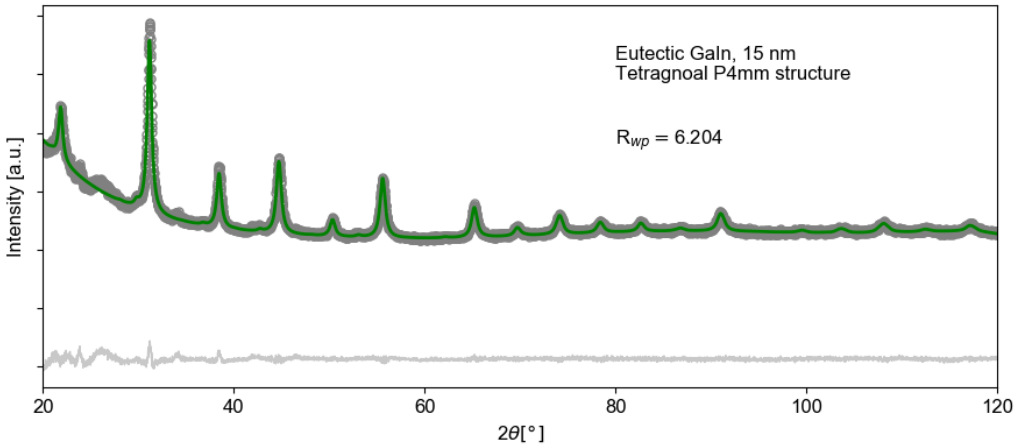
Eutectic GaIn, 15 nm
Tetragnoal P4mm structure
R_{wp} = 6.204
Intensity [a.u.]
20
40
60
80
100
120
2θ[°]

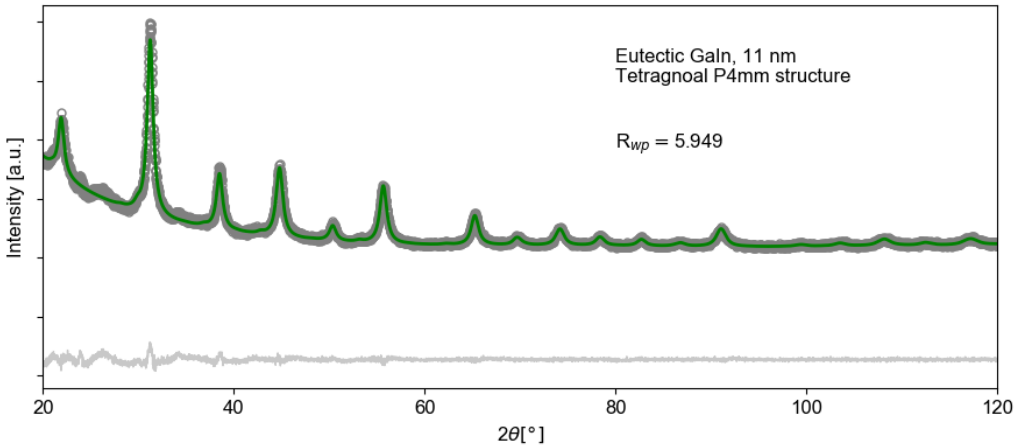
Eutectic GaIn, 11 nm
Tetragnoal P4mm structure
R_{wp} = 5.949
Intensity [a.u.]
20
40
60
80
100
120
2θ[°]

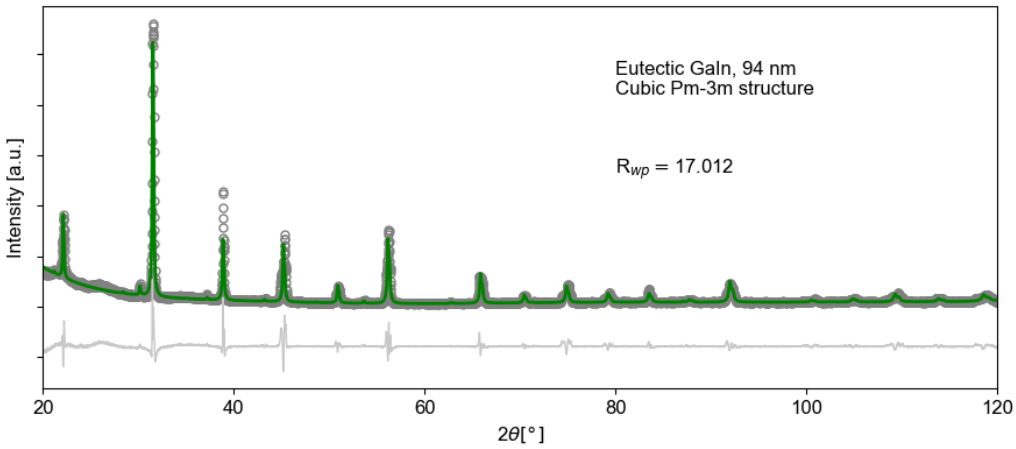
Eutectic GaIn, 94 nm
Cubic Pm-3m structure
R_{wp} = 17.012
Intensity [a.u.]
20
40
60
80
100
120
2θ[°]

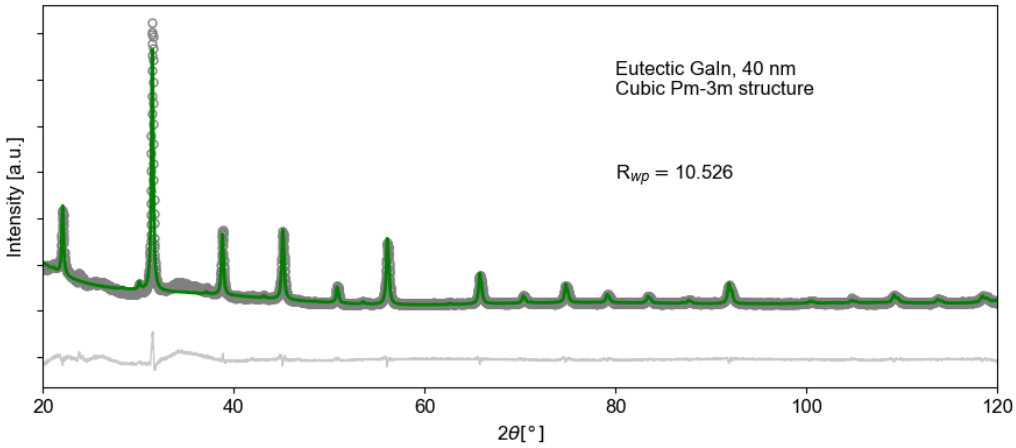
Eutectic GaIn, 40 nm
Cubic Pm-3m structure
R_{wp} = 10.526
Intensity [a.u.]
20
40
60
80
100
120
2θ[°]

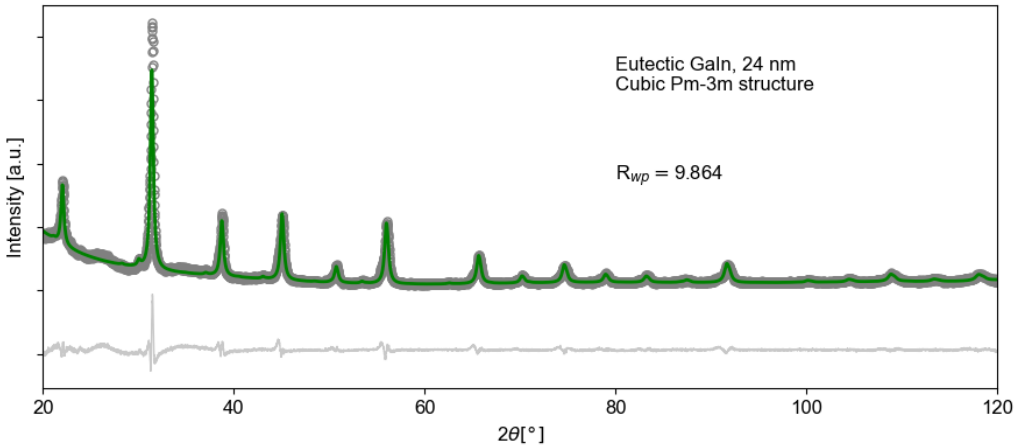
Eutectic GaIn, 24 nm
Cubic Pm-3m structure
R_{wp} = 9.864
Intensity [a.u.]
20
40
60
80
100
120
2θ[°]

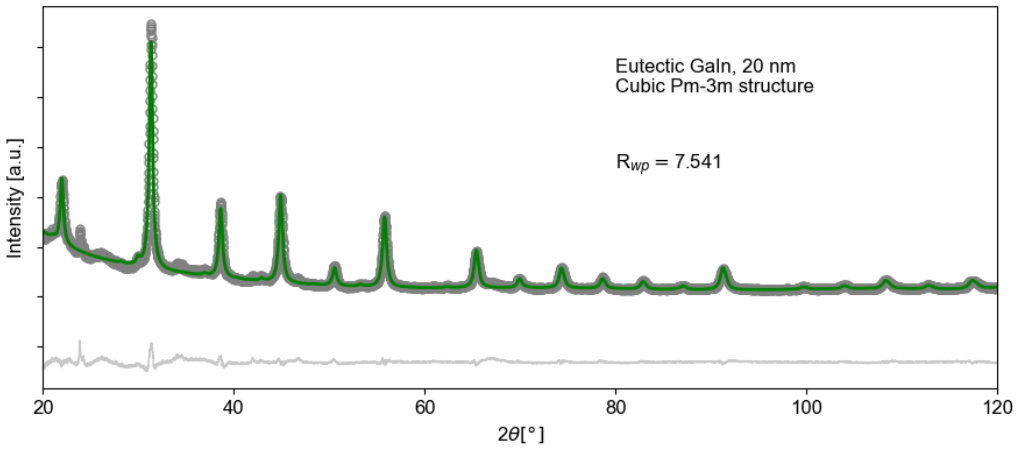
Eutectic GaIn, 20 nm
Cubic Pm-3m structure
R_{wp} = 7.541
Intensity [a.u.]
20
40
60
80
100
120
2θ[°]

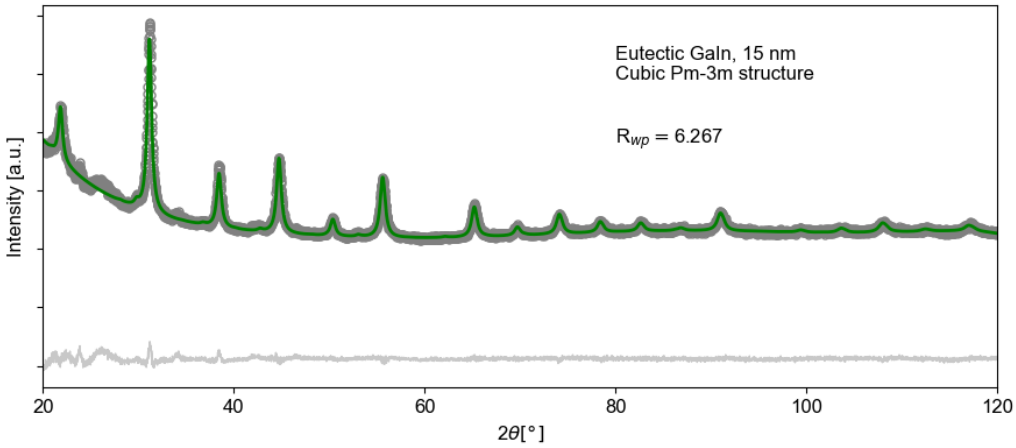
Eutectic GaIn, 15 nm
Cubic Pm-3m structure
R_{wp} = 6.267
Intensity [a.u.]
20
40
60
80
100
120
2θ[°]

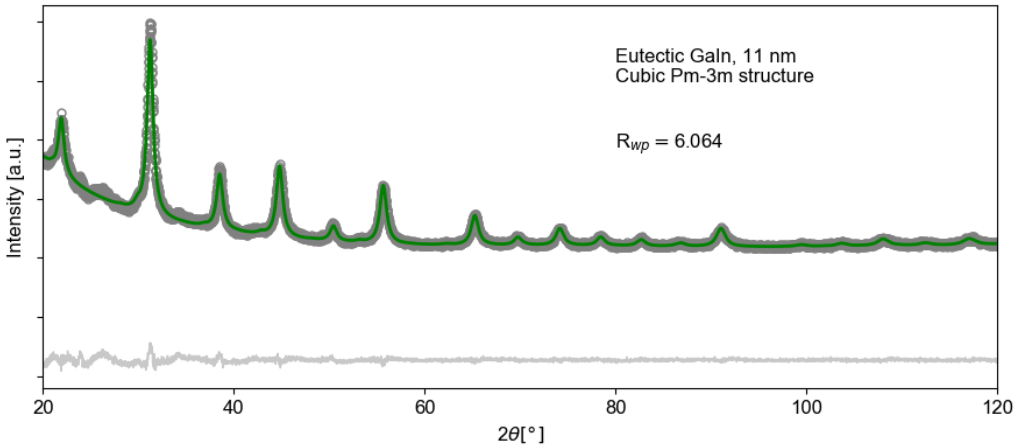
Eutectic GaIn, 11 nm
Cubic Pm-3m structure
R_{wp} = 6.064
Intensity [a.u.]
20
40
60
80
100
120
2θ[°]

Appendix B

Rietveld refinement for size determination

The rietveld refinements for the diffractograms is plotted below. Only tetragonal $P4mm$ symmetry is used, as the cubic crystal symmetry is likely to be a bad approximation for the larger particles.

Size, symmetry and the agreement factor R_{wp} is written in the figures, where the data is marked as gray circles and the Rietveld refinement as the red line.

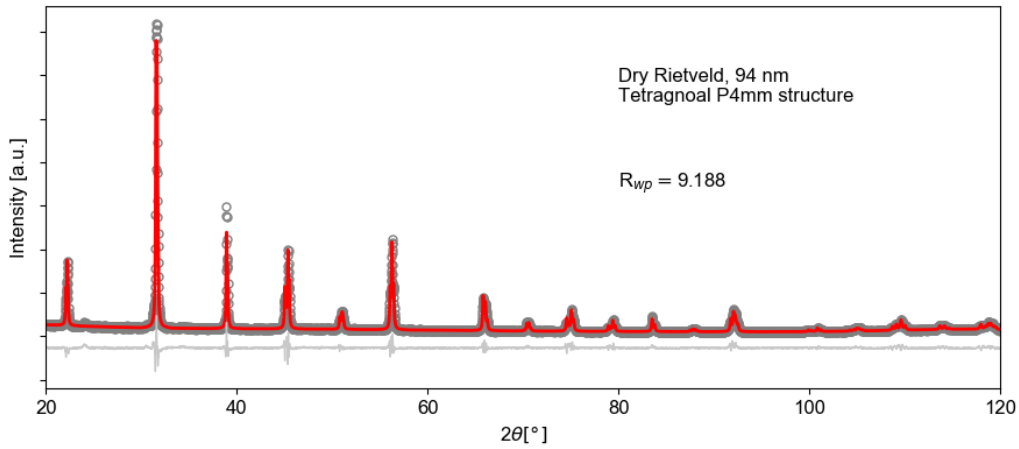
Dry Rietveld, 94 nm
Tetragnoal P4mm structure
R_{wp} = 9.188
Intensity [a.u.]
20
40
60
80
100
120
2θ[°]

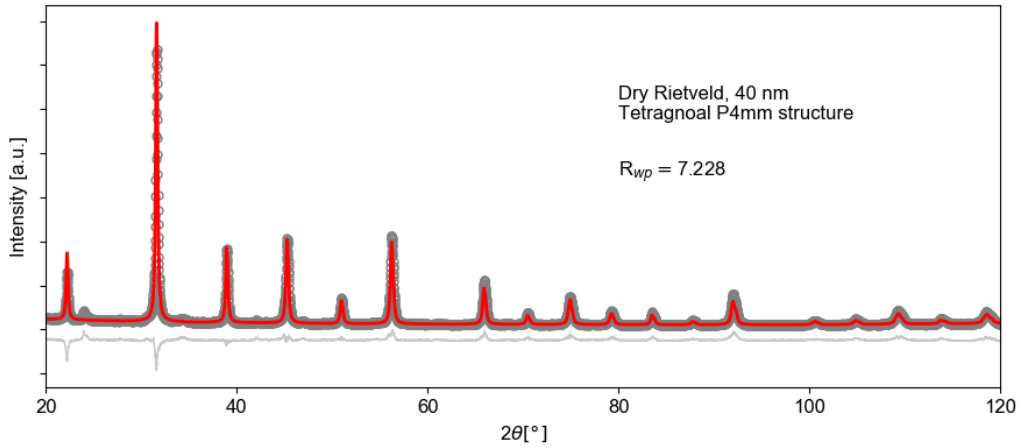
Dry Rietveld, 40 nm
Tetragnoal P4mm structure
R_{wp} = 7.228
Intensity [a.u.]
20
40
60
80
100
120
2θ[°]

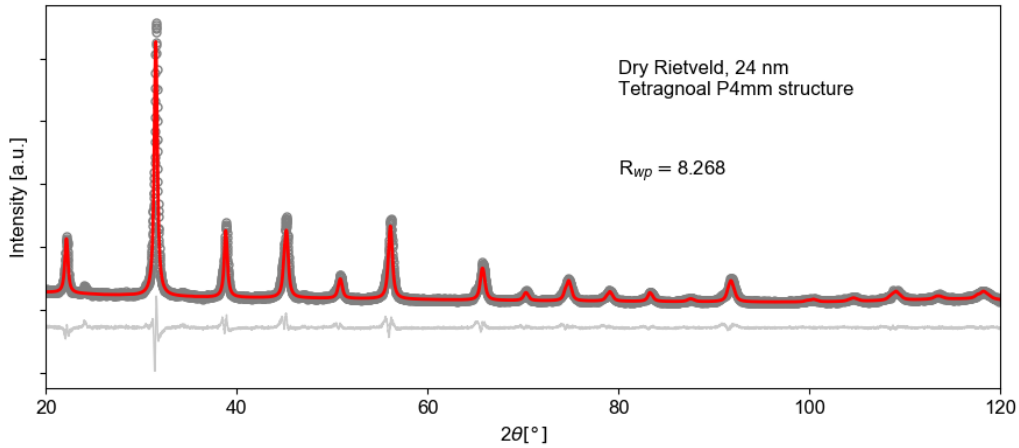
Dry Rietveld, 24 nm
Tetragnoal P4mm structure
R_{wp} = 8.268
Intensity [a.u.]
20
40
60
80
100
120
2θ[°]

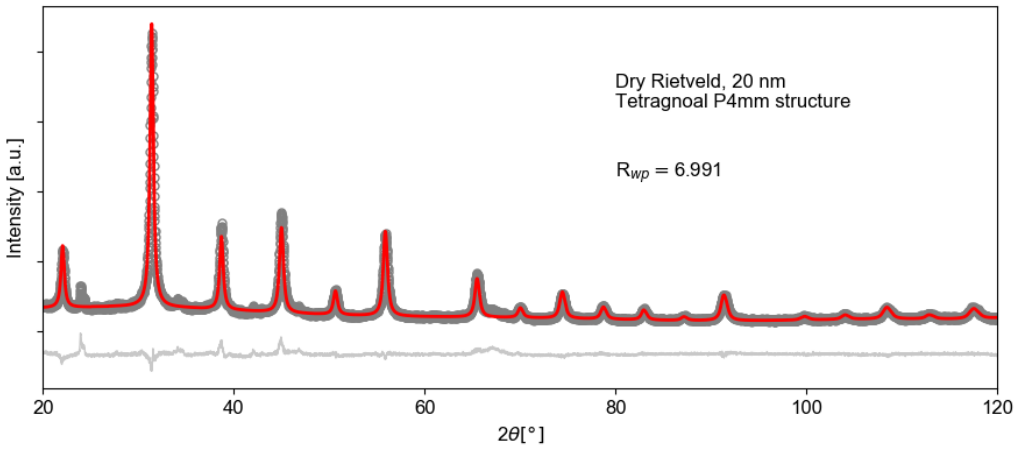
Dry Rietveld, 20 nm
Tetragnoal P4mm structure
R_{wp} = 6.991
Intensity [a.u.]
20
40
60
80
100
120
2θ[°]

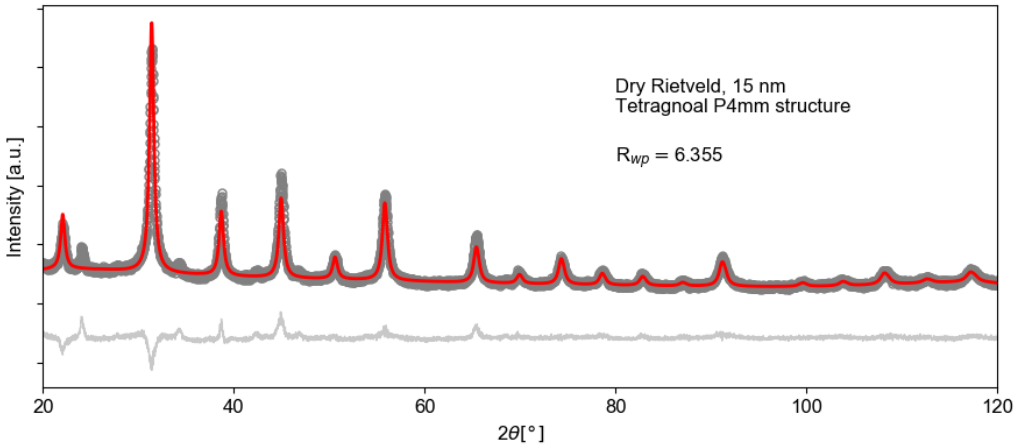
Dry Rietveld, 15 nm
Tetragnoal P4mm structure
R_{wp} = 6.355
Intensity [a.u.]
20
40
60
80
100
120
2θ[°]

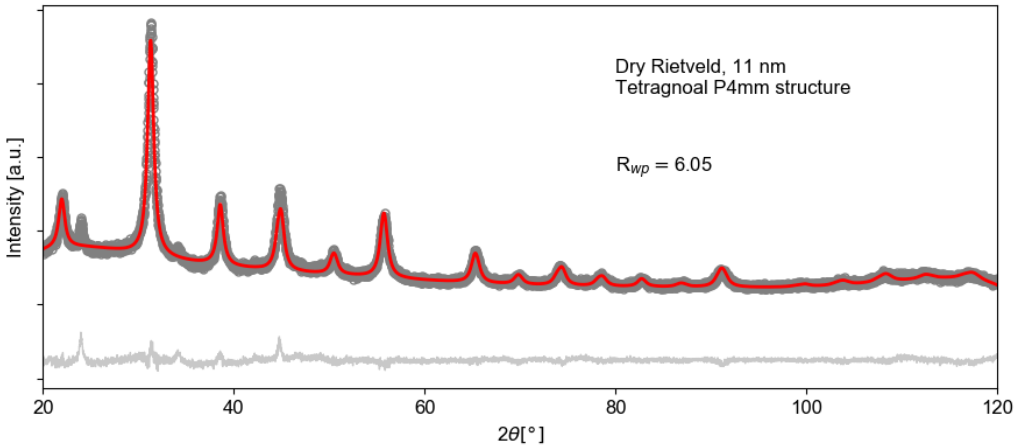
Dry Rietveld, 11 nm
Tetragnoal P4mm structure
R_{wp} = 6.05
Intensity [a.u.]
20
40
60
80
100
120
2θ[°]

Appendix C

Agreement factor R_{wp} for ADP

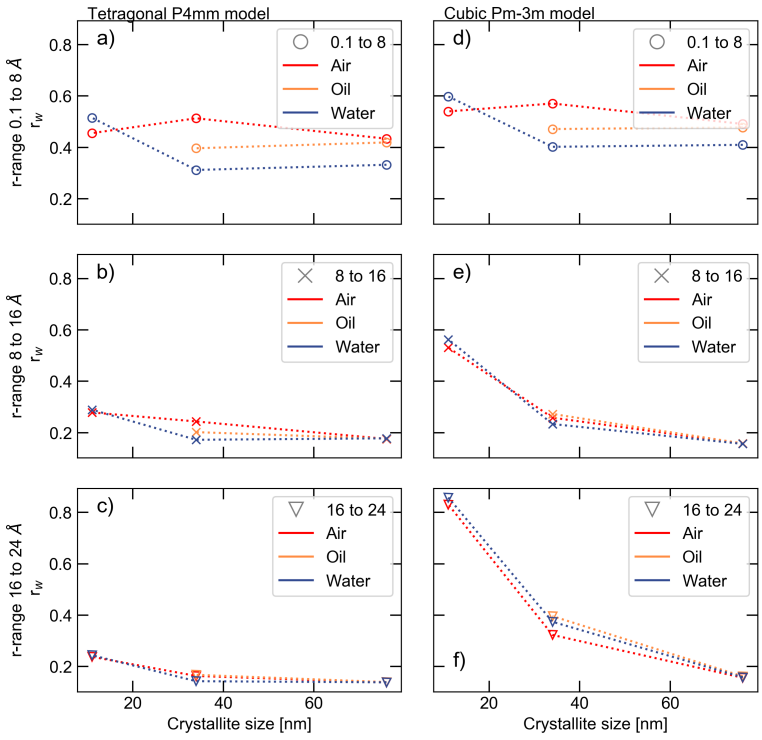

Figure C.1: R_w value for the fits in the ranges from 0.1 to 8 Å (circle), 8 to 16 Å (cross) and 16 to 24 Å (triangle). The fitted parameter for both particles is the scaling factor, Q_{damp} and the ADP.

The agreement factor R_{wp} for the ADP, shown in figure C.1 fits shows a very similar trend as the fits to the lattice parameter a.

Appendix D

Scanning electron microscopy

The two smaller particles, sample ref and sample t-0.5, was both characterized in a scanning electron microscope (SEM) for particle size and morphology characterization. The low degree of vacuum limited the degree of magnification with focused imaging, and the single particle characterization was impossible. Two images at the lowest magnification with good resolution is shown in figure D.1 and D.2.

As $BaTiO_3$ is conductive, the particles become charged by the electron beam. With nanosized particles, this could be unproblematic if the particles are well dispersed on a conductive surface, which will remove the charge accumulation. The particles did agglomerate into large agglomerates, making it impossible to remove the charge build up, and this limits the degree of magnification possible.

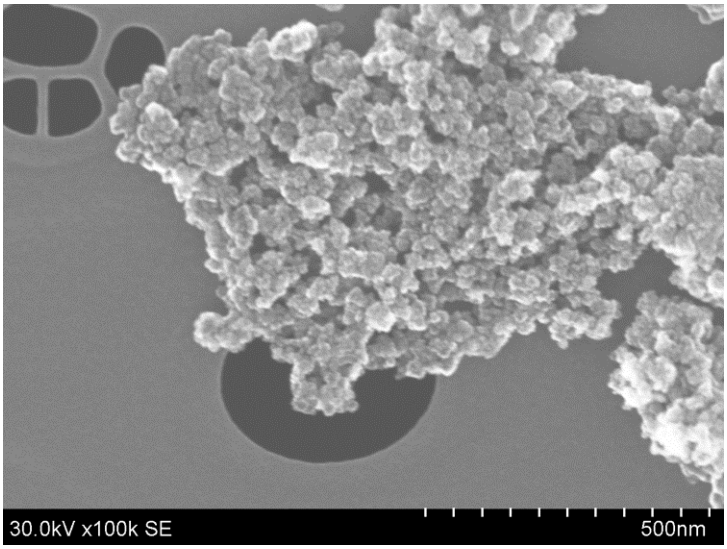

Figure D.1: SEM image of the particle with 11 nm crystallites. The scale bar is 200 nm.

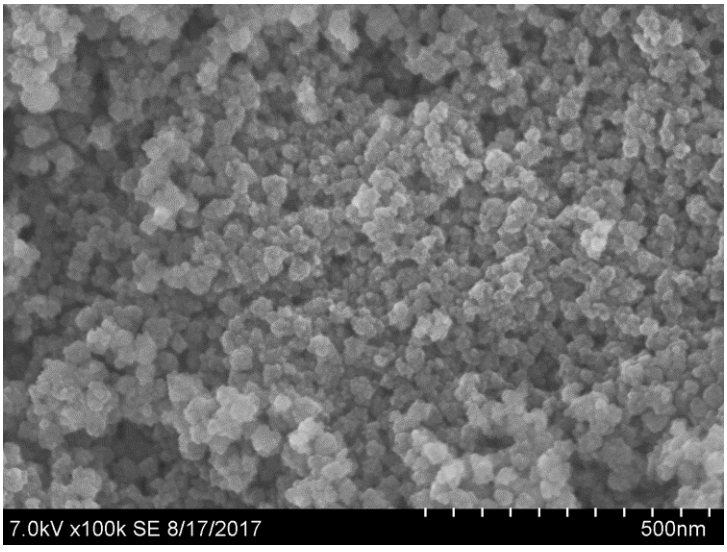

Figure D.2: SEM image of the particle with 15 nm crystallites. The scale bar is 500 nm.